Scouring Patterns in Front of Vertical Breakwaters and Their Influences on the Stability of the Foundations of the Breakwaters

by: Xie Shi-Leng*

September 1981

*Research Fellow at the Coastal Engineering Group of the Department of Civil Engineering, Delft University of Technology, Delft, The Netherlands.
On leave from the Design Institute of the First Navigation Engineering Bureau of the Ministry of Communications, Tianjin, China.

Acknowledgment

I would like to express my sincere gratitude to Prof.Dr.Ir. E.W. Bijker, who kindly agreed my studying at the Coastal Engineering Group, Department of Civil Engineering, Delft University of Technology for two years. The present study was carried out under the direction of Prof. Bijker and Ir. J.J. van Dijk. Their supervision and many valuable advises are greatly appreciated.
Thanks are also given to the staffs of the Group and the Laboratory of Fluid Mechanics of the Department for their friendly cooperation and help in all respects.

List of Figures

Chapter 1. Introduction

Scouring of the sea beds in front or around the coastal structures due to the action of water waves is an important topic in the field of coastal engineering. This problem has been studied with different kinds of structures. For example, the scouring at the base of a vertical or inclined seawall installed on a sloping beach as well as that of a composite breakwater on a flat bed has been studied by Sato, Tanaka and Irie (1968), scouring in front of the inclined seawall on a flat bed by Herbich and Ko (1968), scouring around a porous vertical wall on a sloping beach by Hotta and Marui (1976), and scouring around a circular pile by Wells and Sorensen (1970).

There are some examples of vertical breakwaters under the action of standing waves which have been damaged by the influence of the scouring of sea beds, de Best, Bijker and Wichers (1971) studied the problem of scouring of a sand bed in front of a vertical breakwater, and found that the scouring patterns were different for fine and coarse material. For fine material, the scouring troughs occured at the nodes of the standing waves, and the deposited ridges at the antinodes. For coarse material, the troughs occured halfway between the nodes and the antinodes, and the ridges at the nodes.

Intending to determine the shapes and sizes of the scouring profiles in front of the vertical breakwaters, model tests have been conducted in two wave flumes with four different sand grain sizes in the Laboratory of Fluid Mechanics, Department of Civil Engineering, Delft University of Technology. Most of the test runs were done with regular waves, and a few of them with irregular waves.

In the present study, it was found that the different types of scouring pattern were dependent not only on the sand grain sizes but also on the wave conditions. After discussing the critical velocities for sand particles and the sizes of sand ripples under standing waves in Chapter 4 and 5 respectively, two criteria which may distinguish between two basic scouring patterns are presented in Chapter 6.

The geometrical shape of the scouring profile, the ultimate scouring depth and the development of the scouring depth as a function of time for the relatively fine material are given in Chapter 7. The mechanism of sand transport is discussed. A theoretical bottom profile derived from the equation of continuity is quite similar to the measured profiles, which may in turn prove the assumption that the relatively fine material is moved in suspension by the mass transport current from the

node towards the antinode under standing waves.

The influence of a protective layer on the sand bed on the scouring profile and the result of the test started with a non-flat bottom are also discussed in Chapter 7.

The shape of the scouring profile, the ultimate scouring depth and the development of the scouring depth with time for the relatively coarse material are described in Chapter 8.

Chapter 9 deals with the scale laws for the local scour problem. The scale law for the sand grain size is derived from a dimensionless parameter which has been used in Chapter 6 to distinguish the scouring types. The scale law for the scouring depth is derived from the equation of motion of the sand particle along the slope of a dynamic equilibrium profile.

Chapter 10 presents and discusses the results obtained from the tests with irregular waves. The significant wave height is recommended as the equivalent wave height, although this may lead to a slightly conservative estimate of the scouring depth.

The results of the hydraulic model study have been applied to some typical prototype conditions to examine the influences of the scouring patterns on the stability of the foundations of the breakwaters in Chapter 11. In some unfavourable conditions, the safety factor of stability reduces as much as 20%, which is demonstrated by the slip circle method. But in some other cases, the influence of the scouring holes can almost be neglected, which means that a relatively long protective layer is quite unnecessary.

Chapter 2. Experimental Facilities and Procedure

2.1. Experimental Facilities

The experiments were carried out in two wave flumes. The smaller one shown in Fig. 1 is 38 m long, 0.8 m wide and 0.6 m deep. The side-walls of the 18 m long observation section of this flume consist of glass plates. There is a paddle type wave generator at one end, and a concrete vertical wall at the other end of the flume. The distance between the wave paddle and the wall is 32.9 m. A 6 m long horizontal sand bed is formed in front of the wall, the thickness of which is 0.15 m. A 1:30 slope is used linking the sand bed to the flume bottom. The water depth in the flume is 0.45 m, and the water depth above the flat sand bed is 0.3 m.

The larger flume is 46 m long, 0,8 m wide and 1.0 m deep. The flume is equipped with an electrohydraulic wave generator. By controlling the movement of a servo-hydraulic wave board, it can produce either regular or irregular waves. The distance between the wave board and the vertical wall is 36.2 m. The length of the horizontal sand bed in front of the wall is 11 m. The water depths in the flume are 0.45, 0.55 and 0.65 m, and the water depths above the flat sand bed are 0.3, 0.4 and 0.5 m respectively.

In order to eliminate the re-reflected waves from the wave board, wire-mesh screens were hung in front of the board (Figs. 2 and 3). Also, two layers of table tennis balls were fixed on the front surface of the board. The wave screen system was composed of screens of type 1 and type 2, which are made of 5 and 22 sheets of wire meshes respectively. The diameter of the wire is 1 mm. The size of the mesh is 5 mm. The space between each 2 sheets is 10 mm.

2.2. Instruments

Wave heights and periods were measured by two electric resistance type wave height meters. The wave height meters were placed at the antinodes of the standing waves. The first wave height meter was placed at $\lambda/2$ in front of the vertical wall in the test runs with regular waves, λ being the wave length. This meter was normally placed close on the front surface of the wall in the test runs with irregular waves. Another meter was placed at the antinode position in front of the sand slope.

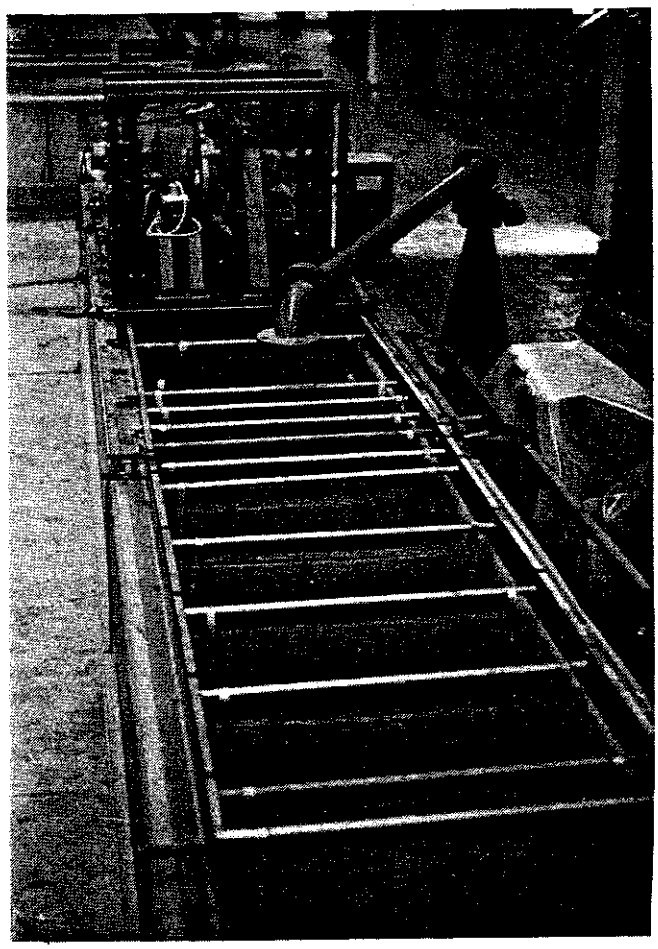

Fig. 3. Wave generator and wire-mesh screens in the small flume.

In some test runs, the orbital velocities of the standing waves at the nodes as well as halfway between the nodes and the antinodes were measured by a current flow meter. The diameter of the micropropeller is 15 mm.

The sand bottom profiles were measured by an electronic profile indicator developed by the Delft Hydraulics Laboratory, which can move along fixed rails on the wave flume (Fig. 4). The instrument consists of a probe placed vertically in water. A servo-mechanism maintains the tip of the probe at a constant distance (adjustable between 0.5-2.5 mm) above the bed. When the instrument is displaced in horizontal direction, the probe will follow the configuration of the bed continuously. The principle of operation is the appreciable difference between the electric conductivities of water and bed material. With a potentiometer the position of the probe is registered.

The waves, orbital velocities and bottom profiles were all recorded on paper by means of a direct-writing oscillograph

Fig. 4. Electronic profile indicator.

With a Correlator as well as a Spectrum Display, the autocorrelation functions and the energy density spectra of the irregular waves can be measured and recorded.

2.3. Experimental Conditions

In the small flume, 26 tests have been conducted with four sand diameters D_{50} = 106, 150, 200 and 780 μm, D_{50} is the particle diameter which was exceeded by 50% in size by weight. The incident waves used had heights H from 5.0 to 9.0 cm, with periods T from 1.17 to 3.56 sec. The wave lengths λ in the water depth h of 30 cm ranged from 171.4 to 600 cm. The wave steepnesses H/λ are from 0.0083 to 0.375, the relative water depths h/λ from 0.05 to 0.175 and the ratios H/D_{50} from 61.1 to 859.1. The test conditions are listed in Table 1 in detail.

In the large flume, another 23 tests with regular waves have been conducted with D_{50} = 200 μm and different water depths h = 30, 40 and 50 cm as well as D_{50} = 106 μm and h = 50 cm. Also, 3 tests with irregular waves have been conducted with D_{50} = 106 μm and h = 30 and 50 cm. Tests No. 17a', 18a', 19a' and 20a' are merely the repetitions of tests No. 17a, 18a, 19a and 20a (Table 2) to see the flume effect. The purpose of using different water depths in the tests is mainly to investigate the scale effect. Tests No. 13b to 16b were executed to examine the criteria which may distinguish the two basic scouring patterns under standing waves. This is explained in detail in Chapter 6.

The sand grain size distribution curves of the four bed materials are shown in Fig. 5. The fall velocities corresponding to D_{50} = 106, 150, 200 and 780 μm are W = 0.7, 1.5, 2.2 and 11 cm/s. These were measured in a settling tube developed by the Delft University of Technology.

2.4. Experimental Procedure

All the tests, except No. 4a, were started with a flat sand bed. The wave profiles were measured at the beginning and end of each test hour. The bottom profiles were measured 15 min, 30 min and 1 hr after starting the waves during the first test hour. For the further test, the bottom profiles were only measured at the end of each hour. The orbital velocities were only measured at the beginning and at the end of the tests. Usually, the equilibrium state of the bottom profiles was reached after 4 to 6 hours of wave action. When a series of tests was finished with one particular sand grain size, then the sand bed was removed and replaced by another size of sand.

In the following, Chapter 3 to 9 will deal with the results with regular waves, and Chapter 10 with irregular waves.

No.	D_{50} (μm)	H (cm)	T (s)	λ (cm)	H/λ	h/λ	H/D_{50}	Remarks
1a		5.0	1.17	171.4	0.0292	0.175	471.7	
2a		7.5	1.32	200	0.0375	0.150	707.5	
3a		5.5	1.53	240	0.0229	0.125	518.9	Begun at the equilibrium profile of No. 7a
4a		5.5	1.53	240	0.0229	0.125	518.9	
5a	106	5.5	1.86	300	0.0183	0.100	518.9	
6a		9.0	1.86	300	0.0300	0.100	849.1	
7a		5.0	2.41	400	0.0125	0.075	471.7	
8a		5.5	1.86	300	0.0183	0.100	518.9	With a protective layer $L = \frac{1}{8}\lambda = 37.5$ cm
9a		5.5	1.86	300	0.0183	0.100	518.9	$L = \frac{1}{4}\lambda = 75$ cm
10a		5.5	1.86	300	0.0183	0.100	518.9	$L = \frac{3}{8}\lambda = 112.5$ cm
11a		5.0	1.17	171.4	0.0292	0.175	333.3	
12a		5.7	1.32	200	0.0285	0.150	380.0	
13a	150	6.5	1.53	240	0.0271	0.125	433.3	
14a		5.7	1.86	300	0.0190	0.100	380.0	
15a		5.0	2.41	400	0.0125	0.075	333.3	
16a		6.0	3.56	600	0.0100	0.050	400.0	
17a		6.5	1.53	240	0.0271	0.125	325.0	
18a	200	5.5	1.86	300	0.0183	0.100	275.0	
19a		5.0	2.41	400	0.0125	0.075	250.0	
20a		5.0	3.56	600	0.0083	0.050	250.0	
21a		6.0	1.32	200	0.0300	0.150	76.9	No sand movement
22a		6.5	1.43	221	0.0295	0.136	83.3	
23a	780	6.5	1.53	240	0.0271	0.125	83.3	
24a		6.0	1.86	300	0.0200	0.100	76.9	
25a		5.0	2.41	400	0.0125	0.075	64.1	
26a		6.0	3.56	600	0.0100	0.050	76.9	No sand movement

Table 1. Test conditions in the small flume (h = 30 cm).

No.	D_{50} (μm)	h (cm)	H (cm)	T (s)	λ (cm)	H/λ	h/λ	H/D_{50}	Remarks
17a'			6.5	1.53	240	0.0271	0.125	325.0	repetition of
18a'			5.5	1.86	300	0.0183	0.100	275.0	repetition of
19a'		30	5.0	2.41	400	0.0125	0.075	250.0	repetition of
20a'			5.0	3.56	600	0.0083	0.050	250.0	repetition of
1b			7.5	1.86	300	0.0250	0.100	375.0	
2b			9.0	2.41	400	0.0225	0.075	450.0	
3b		40	7.5	2.36	444	0.0169	0.090	375.0	
4b	200		10.0	2.36	444	0.0225	0.090	500.0	
5b			5.0	1.70	333	0.0150	0.150	250.0	
6b			9.5	1.70	333	0.0285	0.150	475.0	
7b			4.5	1.98	400	0.0113	0.125	225.0	
8b		50	7.5	1.98	400	0.0188	0.125	375.0	
9b			11.0	1.98	400	0.0275	0.125	550.0	
10b			11.0	2.20	455	0.0242	0.110	550.0	
11b			7.5	3.12	667	0.0112	0.075	375.0	
12b			10.0	3.12	667	0.0150	0.075	500.0	
13b			4.5	1.70	333	0.0135	0.150	424.5	
14b			5.0	1.70	333	0.0150	0.150	471.7	
15b			6.0	1.70	333	0.0180	0.150	566.0	
16b			8.5	1.70	333	0.0255	0.150	801.9	
17b	106	50	7.5	2.40	500	0.0150	0.100	707.5	
18b			10.0	2.40	500	0.0200	0.100	943.4	
19b			8.0	3.12	667	0.0120	0.075	754.7	
1c			8.5	1.72	337	0.0252	0.148	801.9	irregular wave $H = H_s$, $T = \bar{T}$
2c			9.1	1.98	400	0.0228	0.125	858.5	" "
3c		30	7.1	1.69	270	0.0263	0.111	669.8	" "

Table 2. Test conditions in the large flume.

Chapter 3. Waves and Orbital Velocities

3.1. Waves

The wave profiles of test No. 2a and 25a are shown in Figs. 6 and 7, which represent the shorter and longer waves used in the tests respectively. l_1 and l_2 in the figures are the distances of the wave height meters from the wal. The wave profiles in Fig. 6 were taken at the beginning of the test, so that the incident waves as well as the standing waves can be seen. The wave profiles in Fig. 7 were taken at the end of the fourth hour of the test. It can be seen in these two figures that both the waves near the wall and the waves in front of the sand slope are regular. The heights and periods as well as the shapes of the individual waves are very close to one another. In fact, it could be seen in the tests that the wave forms merely moved up and down between the nodes, which is the basic feature of the standing waves. This means that the screen system used in the flume is quite efficient to eliminate the re-reflected waves from the wave paddle.

However, in some test runs the wave profiles gradually became irregular when the scouring patterns of the sand bed gradually developed. An example is shown in Fig. 8. At the beginning of this test, the waves near the wall as well as in front of the sand slope were regular. After two hours of wave action, the maximum depth of the scouring trough reached 6.5 cm. The waves became then obviously irregular, especially for the waves in front of the sand slope. The heights of the individual waves were not equal, and the shapes differed from one to another. The positions of the nodes and the antinodes of the standing waves shifted to and for along the flume. It may roughly be said that when the maximum scouring depth in h = 30 cm reaches about 4 cm, the irregularity of the wave profile can be noticed. This phenomenon may be regarded as the interaction between the scouring pattern and the waves.

3.2. Orbital Velocites

The horizontal component of the orbital velocity of the standing waves described by the second order theory of Miche is:

$$u = \frac{2\pi H}{T} \frac{\cos h\, K\,(z+h)}{\sin h\, Kh} \cos Kx \cos \omega t + \frac{3\pi^2 H^2}{2T\lambda} \frac{\cos h\, 2K\,(z+h)}{\sin h^4 Kh} \sin 2Kx \sin 2\omega t \qquad (1)$$

where $K = 2\pi/\lambda$, $\omega = 2\pi/T$, x and z are horizontal and vertical coordinates measured from the origin O, O is at the still water level of the node, x is positive towards the wall, z is positive upward, and t is time.

The first term on the right-hand side of eq. 1 represents the first order expression for the horizontal velocity.

Fig. 9 shows the measured wave and orbital velocity profiles of test No. 25a. In that figure, symbol a refers to the records taken at the beginning of the first test hour and b refers to the records taken at the end of the fifth test hour. Comparing the wave profiles a.1 and b.1, the wave heights are the same, but the shapes of the waves are a little different. Comparing the velocity profiles a.2 and b.2 measured at $x = 0$, $z_b = 5$ cm, that is at the node position in front of the wall, and $z_b = z + h$ is the height above the undisturbed flat sand bed, it can be seen that the orbital velocity near the bottom decreases with increasing time. The velocity profiles a.3 and b.3 are taken at $x = \lambda/8$, $z_b = 3$ cm, and a.4 and b.4 at $x = \lambda/8$, $z_b = 20$ cm. From a.4 and b.4, it can be seen that $u_- > u_+$ near the water surface. u_+ and u_- are the maximum horizontal velocity components, the directions of which are from and towards the node respectively.

As the maximum velocity at the bottom u_b is important to the problem of scouring of the sand bed, the velocities measured at $x = 0$ and near the bottom ($z_b = 3$ cm for tests No. 11a to 13a and $z_b = 5$ cm for the other 12 test runs) as well as that measured at $x = \lambda/8$ and near the bottom ($z_b = 3$ cm for tests No. 11a and 12a and $z_b = 5$ cm for the other 13 test runs) at the beginning of the tests have been compared with the theoretical values in Figs. 10 and 11.

From eq. 1, it can be seen that the second term is zero for $x = 0$. This means that the result of the second order theory is the same as that of the first order theory at the node. The differences between the results from the first and second order theories at $\lambda/4 > x > 0$ depend on h/λ, H/λ and x. Generally speaking, for the conditions used in the present study the differences are not so significant when $h/\lambda > 0.10$. But when $h/\lambda < 0.10$, these differences will be significant due to the influence of $1/\sin h^4$ Kh in the second term of eq. 1.

The measured bottom velocities are close to those obtained from the theory at the nodes as shown in Fig. 10. The relative error $\frac{u_{max.t} - u_{max.m}}{u_{max.t}}$ is from -11.6% to +7.1%. u_{max} is the maximum velocity at the bottom at the node, and the extra subscripts t and m represent the theoretical and measured values respectively. On the average

$u_{max.m} = 1.026\ u_{max.t}$ with a standard deviation $\sigma = 0.0470$. The correlation coefficient between $u_{max.t}$ and $u_{max.m}$ is $\rho = 0.9843$.

The measured bottom velocities are close to the results of the first order theory halfway between the nodes and the antinodes as shown in Fig. 11. The relative error $\frac{u_{b.t} - u_{b.m}}{u_{b.t}}$ is from -12.4% to +2.8%.

The meaning of the extra subscripts t and m for u_b is the same as that for u_{max}. On the average $u_{b.m} = 1.031\ u_{b.t}$, with $\sigma = 0.0497$ and $\rho = 0.9780$.

The second order theory gives much higher result than the measured value when the relative water depth is small. For example, $u_{b.m} = 23.9$ cm/s at $x = \lambda/8$ of test No. 16a, but according to eq. 1 $u_{b.t} = 41.2$ cm/s, which is 72% higher than the measured value.

It is interesting to mention that Lé Mehauté et al (1968) have proved in their tests with progressive waves that the first order theory described the bottom orbital velocities in the flume better than the second order theory did, especially in relatively shallow water.

Figs. 12 to 15 show the orbital velocity field patterns of tests No. 13a to 16a, which were done on the bed with sand of 150 μm. The velocities at different heights z_b at the nodes and halfway between nodes and antinodes measured at the beginning as well as at the end of the tests are shown. The theoretical velocity values from the first order theory are also shown in these figures. The measured velocity field patterns at the beginning of the tests are quite close to the theoretical ones.

The near bottom velocities at the nodes taken at the end of tests No. 13a to 15a show clearly that they are influenced by the deformed sand bed. Such an influence decreases with increasing z_b as shown in Table 3.

No. / z_b (cm)	13a	14a	15a
3 (for No. 13a) or 5	0.933	0.896	0.920
10	0.937	0.933	0.923
20	1.00	1.00	1.00

Table 3. The ratios of $u_{m.e}/u_{m.b}$ at the nodes.

u_m is the measured velocity, and the extra subscripts b and e represent the values taken at the beginning and end of the test respectively. The velocity at $z_b = 5$ cm at the node of test No. 16a could not be measured

at the end of the test, because the height of the deposited sand ridge reached 4.5 cm above the original sand bed. However, the near bottom velocities at x = λ/8 of test No. 16a, as well as test No. 15a, at the end of the test are smaller than those at the beginning of the test. Table 4 shows the ratios of $u_{m.e}/u_{m.b}$ at x = λ/8.

No. / z_b (cm)	15a	16a
5	0.899	0.979
10	0.879	0.974
20	0.904	1.00

Table 4. The ratios of $u_{m.e}/u_{m.b}$ at x = λ/8.

Figs. 16 and 17 show the orbital velocity field patterns of tests No. 18b and 19b, which were done on the bed with sand of D_{50} = 106 μm. The measured velocity field patterns at the beginning of the tests are quite close to the theoretical ones. The maximum ratio of u_m/u_t is 1.071 for test No. 18b at x = λ/8, z_b = 30 cm. u_t is the calculated velocity from the first order theory.

The near bottom velocities at the nodes taken at the end of tests No. 18b and 19b are smaller than those at the beginning just like in the cases of tests No. 13a to 15a, although the scouring patterns of these two series of tests are quite different as shown in Figs. 12 to 17. Table 5 shows the ratios of $u_{m.e}/u_{m.b}$ at the nodes for tests No. 18b and 19b as well as for tests No. 15b and 17b. The results of tests No. 15b and 17b are not shown with drawings.

No. / z_b (cm)	15b	17b	18b	19b
5	0.951	0.943	0.958	0.828
10	0.958	0.972	0.958	0.890
20	1.00	1.00	0.939	0.946
30	1.00	1.00	1.00	1.00

Table 5. The ratios of $u_{m.e}/u_{m.b}$ at the nodes.

When the orbital velocity field patterns at the end are compared with those at the beginning at $x = \lambda/8$ of tests No. 15b, 17b, 18b and 19b, no differences can be seen.

Test No. 19b is the only case that the velocities at the level of the original flat bed and at 3 cm below this level at the node has successfully been measured as shown in Fig. 17b. At the time of measuring the maximum scouring depth was 7.5 cm. In all the other cases, the micro-propeller did not work well when it was very close to the sand bed where the concentration of sediment was high.

Usually, the decrease of near bottom velocities with increasing time at the place of a scouring trough can be simply considered to be due to the increase of the cross section perpendicular to the direction of waves. In the present study, since the near bottom velocities decrease with time at nodes even in the cases when there are the deposited ridges, it might be considered as the characteristic of the uneven bottoms, the boundary conditions of which are different from that used in the theories of standing waves.

3.3. Mass Transport

According to the theory presented by Longuet-Higgins (1952) the direction of the mass transport current in a standing wave is from node to antinode near the bottom and it is opposite near the water surface. The mass transport velocity at the bottom is given by:

$$\bar{U} = \frac{3\pi^2 H^2}{2T \lambda \sin h^2 Kh} \sin 2Kx \qquad (2)$$

However, Noda (1968) has found in his experiments that the measured mass transport velocity at the bottom is less than that predicted by eq. 2 when the boundary layer becomes turbulent.

No attempt has been made to measure the mass transport currents of the standing waves. But small solid particles made of a mixture of paraffin and paint powder, the density of which is close to that of water, were used in the tests to observe the direction of the mass transport currents near the bottom. This direction is always from nodes to antinodes.

Chapter 4. Critical Velocities for Sand Particles

The sand bed was covered with ripples in every test run except No. 21a and 26a. The size of the sand ripple decreases with increasing distance $|x|$ from the node, owing to the fact that the maximum velocity at the bottom u_b decreases with increasing $|x|$.

After starting the test, the sand ripples appear first near the nodes, then extend towards the antinodes. For relatively coarse material, the sand ripples will extend up to a distance l_r measured from the antinodes in some 30 to 60 minutes. There is no sand movement at $|x| > \frac{\lambda}{4} - l_r$ where u_b is too low to stir up the sand particles from the bed.

l_r may not be so definitive for relatively fine material, because there will be sand deposit near the antinode where $|x| > \frac{\lambda}{4} - l_r$ as described in the Introduction and as to be explained in Section 7.4, and the sand deposit will also be covered with ripples. However, when $l_{r,t}$ is expressed as function of t (Fig. 18), $l_{r,t}$ is the distance between the antinode and the most extended ripple at anytime t, it can be seen that the rate of extension of the ripples generated by the orbital velocities is different from that moving with the sand deposit.

It is still possible to determine l_r in some 30 to 60 minutes for the relatively fine sand. Fig. 19 shows how to determine l_r from a record of the bottom profile.

The bottom orbital velocity at l_r defined as the critical velocity for sand particles $u_{crit.}$ in the present study can be obtained from a diagram calculated by the first order theory of the standing waves, an example of which is given in Fig. 20. The values of l_r and $u_{crit.}$ of all the tests are listed in Tables 6 and 7.

No.	D_{50} (μm)	l_r (cm)	$u_{crit.}$ (cm/s)	No.	D_{50} (μm)	l_r (cm)	$u_{crit.}$ (cm/s)
1a		8.5	6.0	16a		26.0	9.5
2a		6.0	6.4	17a		11.0	9.0
3a	106	10.0	6.8	18a	200	16.0	9.5
5a		12.0	7.0	19a		24.0	10.0
7a		17.0	7.0	20a		30.0	10.5
11a		10.0	7.0	22a		21.0	17.0
12a		10.0	7.7	23a	780	22.0	16.5
13a	150	9.0	7.3	24a		28.0	17.0
14a		15.0	9.0	25a		46.0	17.5
15a		23.0	9.8				

Table 6. $u_{crit.}$ of the tests in the small flume.

There are many formulae dealing with the critical velocities for sand particles under oscillatory waves. De Best, Bijker and Wichers (1971) have compared the critical velocities obtained from the tests under standing waves with those calculated from the formulae presented by Bagnold and Goddet. Silvester and Mogridge (1970) have collected 13 formulae. Most of the important formulae have been reviewed by Komar and Miller (1974), and two formulae for finer and coarser sands respectively were presented by them. On the basis of calculations and comparisons of the 13 formulae mentioned above, Swart (1977) presented a new formula. Recently, Hallermeier (1980) has also intended to provide a unified criterion. Only the results of the formulae of Bagnold, Goddet, Komar and Miller and Swart will be compared with those of the tests in the following. All the formulae used in the comparison are listed in Table 8.

No.	D_{50} (μm)	l_r (cm)	$u_{crit.}$ (cm/s)	No.	D_{50} (μm)	l_r (cm)	$u_{crit.}$ (cm/s)
17a'		11.0	9.0	11b	200	41.0	11.5
18a'		16.0	9.5	12b		28.0	10.7
19a'		24.0	10.0	13b		27.0	7.5
20a'		30.0	10.5	14b		24.0	7.5
5b	200	25.0	7.5	15b		20.0	7.5
6b		14.0	8.5	16b	106	15.0	8.0
7b		36.0	8.8	17b		26.0	9.0
8b		20.0	9.0	18b		18.0	9.0
9b		17.0	10.8	19b		33.0	10.0
10b		20.0	11.5				

Table 7. $u_{crit.}$ of the tests in the large flume.

Names	Formulae	Remarks
Bagnold	$u_{crit.} = 2.40\ \Delta^{2/3}\ D_{50}^{0.433}\ T^{1/3}$	for laminar boundary layer
Goddet	$u_{crit.} = 0.85\ \Delta^{2/3}\ D_{50}^{1/4}\ T^{3/8}$	for turbulent boundary layer
Komar and Miller	$u_{crit.} = 1.10\ \Delta^{2/3}\ D_{50}^{1/3}\ T^{1/3}$	for $D_{50} < 500$ μm
	$u_{crit.} = 3.68\ \Delta^{2/3}\ D_{50}^{3/7}\ T^{1/7}$	for $D_{50} > 500$ μm
Swart	$u_{crit.} = 4.58\ D_{50}^{0.38}\ T^{0.043}$	for $\Delta = 1.6$

Table 8. Formulae for $u_{crit.}$ (in metric units).

In Table 8, $\Delta = \frac{\rho_s - \rho}{\rho}$ is the relative mass density of sand, and ρ_s and ρ are the mass densities of sand and water respectively. Δ is taken as 1.65 except for Swart's formula.

Figs. 21 to 24 show the comparisons of $u_{crit.}$. Goddet's formula is only used for D_{50} = 780 μm. On the whole, the present test data are lower than the results of the formulae for all sand diameters. The Swart's results are much higher than those of the present tests. The Bagnold's results are most close to but still a little higher than the test data. It should be pointed out that the same conclusion can be obtained from the test data given by de Best, Bijker and Wichers (1971).

It seems that the critical velocities obtained in h = 50 cm are a little higher than those obtained in h = 30 cm for D_{50} = 106 μm in Fig. 21. However, such a tendency can hardly be seen for D_{50} = 200 μm in Fig. 23.

Madson and Grant (1976) proposed a modified Shields Diagram for the onset of sediment motion in oscillatory flow. The Shields Parameter is:

$$\psi = \frac{\tau}{\rho g \Delta D_{50}} \tag{3}$$

in which τ is the bed shear stress given by Jonssen (1966) as:

$$\tau = \frac{1}{2} f_w \rho u_b^2 \tag{4}$$

where f_w is the wave friction factor which can be expressed as:

$$f_w = \exp\left[-5.977 + 5.213 \left(\frac{a_b}{r}\right)^{-0.194}\right] \tag{5}$$

when $1.47 < \frac{a_b}{r} < 3{,}000$, and $f_w = 0.32$ when $\frac{a_b}{r} \leq 1.47$.

a_b is the amplitude of the orbital motion at the bottom, for the first order theory of standing waves:

$$a_b = \frac{u_b T}{2\pi} \tag{6}$$

r is the bed roughness. Madson and Grant (1976) took $r = D_{50}$ in their modified Shields Diagram.

The Shields Parameter ψ for the different sand diameters in the present study is shown in Table 9.

D_{50} (μm)	106	150	200	780
ψ	0.022 ~ 0.036	0.022 ~ 0.030	0.019 ~ 0.030	0.028 ~ 0.033

Table 9. Shields Parameter ψ.

These values are lower than the mean value obtained from the oscillating plate tests as well as from the progressive waves tests, which is about 0.06.

According to the above comparisons, both $u_{crit.}$ and ψ obtained under standing waves in the present study are lower than those under progressive waves or in oscillatory flow. The main reason for these differences is that the definitions of $u_{crit.}$ are different. Bagnold (1946) as well as many other research workers defined $u_{crit.}$ as the velocity which initiated the motion of the sand grains on a flat bed. In the present study, $u_{crit.}$ is determined at a distance l_r measured from the antinode. When the sand particles are stirred up and form a sand ripple at that place, at the side towards the node the sand bed has already been rippled, since the sand ripples extend from node towards antinode as described before. Because the incipient motion of the sand particles at l_r measured from the antinode could be influenced by the neighbouring ripples, it is likely that $u_{crit.}$ in the present study will be lower than that found by Bagnold (1946) and the others. In this respect, it should also be mentioned that Davies and Wilkinson (1978) have compared the threshold velocities for sand particles over a rippled bed with those over a flat bed, and found that the former are lower than the latter.

Chapter 5. Sand Ripples

Since the bed roughness r may be closely related to the ripple geometry when the sand bed is rippled, the ripple height H_r and ripple length λ_r are important parameters in sediment motion.

Nielsen (1979) analysed many laboratory data obtained from oscillatory flow as well as from progressive waves condition, and found:

$$\frac{H_r}{a_b} = 0.275 - 0.022 \frac{u_b}{(g \Delta D_{50})^{0.5}} \tag{7}$$

$$\frac{H_r}{\lambda_r} = 0.32 \tan \phi \quad (\text{for } \psi < 0.2) \tag{8}$$

in which ϕ is the natural repose angle of sand. ψ is calculated from eqs. 3, 4, 5 and 6 with $r = 2.5\ D_{50}$. It is worthwhile to compare H_r and λ_r measured in the present tests with those obtained from eqs. 7 and 8, as there were no test data under standing waves condition in the formulation or these equations.

Fig. 25 shows the comparison of the result of eq. 7 and the test data at the nodes. It seems that the latter are a little higher than the former.

Table 10 shows the comparison of the results of eq. 8 and the test data. ϕ is taken as 30° for D_{50} = 106, 150 and 200 μm, and 35° for 780 μm.

D_{50} (μm)		106	150	200	780
H_r/λ_r	from eq. 8	0.18	0.18	0.18	0.22
	from test data	0.15 ~ 0.21	0.16 ~ 0.22	0.15 ~ 0.20	0.16 ~ 0.20

Table 10. Comparison of H_r/λ_r.

Chapter 6. Two Basic Scouring Patterns

De Best, Bijker and Wichers (1971) have found in their model study that the scouring patterns of a sand bed in front of a vertical wall under the action of standing waves were different with the sand grain sizes. Three sand diameters D_{50} = 130, 160 and 220 μm were used in their tests. The fine material (D_{50} = 130 μm) was transported largely in suspension, which was scoured at the nodes and deposited near the antinodes of the standing waves. The coarse material (D_{50} = 220 μm) moved mainly as bed load, which was scoured halfway between the nodes and the antinodes and deposited at the nodes. The material of medium size (D_{50} = 160 μm) was not scoured much in the tests. Fig. 26 shows the typical bottom profiles for fine and coarse materials mentioned above.

In the present study, the scouring pattern which is typical for the fine material appeared in the case of D_{50} = 106 μm, and that for the coarse material in the cases of D_{50} = 150, 200 and 780 μm in the small flume. In some test runs (No. 13a to 15a) for D_{50} = 150 μm, however, there was a mixed type scouring pattern taking place in the flume. That is to say, some nodes were eroded and others accumulated sand.

It is considered that both the type found in the former study for D_{50} = 160 μm described above and the mixed type found in the present study are the transitional type between two basic scouring types which are typical for fine and coarse material respectively.

It was then proved that both types of the basic scouring pattern can occur for the same sand grain size by changing the wave characteristics in the large flume. The types of the scouring patterns of all test runs are listed in Table 11. It can be seen in the table that the sand particles of D_{50} = 200 μm, which usually act as "coarse material", act as "fine material" in test No. 2b. Comparing the test conditions of tests No. 19a' (or 19a) and 2b (Table 2), h = 30 cm and T = 2.41 sec are the same, only H is increased from 5.0. to 9.0 cm. The sand particles of D_{50} = 106 μm, which usually act as "fine material", act as "coarse material" in tests No. 13b and 14b, only because the wave heights are smaller in these two runs than in tests No. 15b and 16b (Table 2).

It seems to be logical to use the terms of "relatively fine material" and "relatively coarse material" rather than "fine material" and "coarse material", since the scouring patterns are dependent not only on the sand grain sizes but also on the wave conditions. However, for the sake of simplicity, these two different scouring patterns will sometimes be referred to in the following as Type "fine" and Type "coarse" respectively.

One of the important problems is to find the criterion which can distinguish the two types of scouring pattern. Several dimensionless parameters have been tried, such as h/WT which has been used successfully in the prediction of eroded (bar) or accreted (berm) profile of beaches, H/WT, u_{max}/W, u_{*m}/W, $(u_{max} - u_{crit.})/W$ and $(u_{*m} - u_{*c})/W$. u_* is the shear velocity, the extra subscripts m and c indicate that values obtained from u_{max} and $u_{crit.}$ through

$$u_* = \sqrt{\frac{\tau}{\rho}} \tag{9}$$

τ has been expressed in eq. 4 already.

No.	D_{50} (μm)	u_{max} (cm/s)	$\frac{u_{max}-u_{crit}}{W}$	Types of scouring pattern	No.	D_{50} (μm)	u_{max} (cm/s)	$\frac{u_{max}-u_{crit}}{W}$	Types scouri patter
1a		20.1	20.1	fine	1b		37.8	12.9	coarse
2a		32.8	37.7	fine	2b		48.0	17.3	fine
3a	160	26.0	27.4	fine	3b		33.5	10.7	coarse
5a		27.7	29.6	fine	4b		44.7	15.8	coarse
6a		45.4	54.9	fine	5b		17.0	4.3	coarse
7a		26.7	28.1	fine	6b	200	32.3	10.8	coarse
11a		20.1	8.7	coarse	7b		16.4	3.5	coarse
12a		24.9	11.5	coarse	8b		27.4	8.4	coarse
13a	150	30.7	15.6	mixed	9b		40.2	13.4	coarse
14a		28.7	13.1	mixed	10b		42.0	13.9	coarse
15a		26.7	11.3	mixed	11b		30.9	8.8	coarse
16a		33.1	15.7	coarse	12b		41.2	13.9	coarse
17a		30.7	9.9	coarse	13b		15.3	11.1	coarse
18a	200	27.7	8.3	coarse	14b		17.0	13.6	coarse
19a		26.7	7.6	coarse	15b		20.4	18.4	fine
20a		27.6	7.8	coarse	16b	106	28.9	29.9	fine
22a		29.8	1.2	coarse	17b		29.3	29.0	fine
23a	780	30.7	1.3	coarse	18b		39.1	43.0	fine
24a		30.3	1.2	coarse	19b		33.0	32.9	fine
25a		26.7	0.8	coarse					

Table 11. Types of the scouring patterns.*

*for No. 17a' to 20a' are the same as for No. 17a to 20a.

According to the results of calculation, it was found that only $(u_{max}-u_{crit.})/W$ or $(u_{*m}-u_{*c})/W$ could be used to distinguish between the scouring patterns. The scouring pattern is Type "coarse" when $(u_{max}-u_{crit.})/W \lesssim 15.8$, and Type "fine" when this parameter is equal to 17.3 (No. 2b) for D_{50} = 200 μm in Table 11. The scouring pattern is Type "coarse" when $(u_{max}-u_{crit})/W \lesssim 13.6$, and Type "fine" when $(u_{max}-u_{crit.})/W \gtrsim 18.4$ for D_{50} = 106 μm. The highest value of the same parameter for Type "coarse" and mixed type is 15.7 (No. 16a) when D_{50} = 150 and 780 μm. It seems to be reasonable to take $(u_{max}-u_{crit.})/W \gtrsim 16.5$ as the criterion for scouring pattern Type "fine", and $(u_{max}-u_{crit.})/W < 16.5$ for Type "coarse" (including mixed type). The values of $(u_{*m}-u_{*c})/W$ have been calculated taking the bed roughness $r = D_{50}$ as well as $r = H_r$. Only the result of the former can be used for the purpose of distinguishing between the scouring patterns. $(u_{*m}-u_{*m})/W \gtrsim 1.12$ can be taken as the criterion for scouring pattern Type "fine". Only those values near this critical value will be shown in Table 12.

When $(u_{max}-u_{crit.})/W$ or $(u_{*m}-u_{*c})/W$ is relatively high, the majority of the material will be moved as suspended load rather than as bed load.

No.	D_{50} (μm)	$(u_{*m}-u_{*c})/W$	Types of scouring pattern
1a	106	1.49	fine
15b	106	1.27	fine
2b	200	1.14	fine
13a	150	1.11	mixed
16a	150	0.99	coarse
4b	200	1.05	coarse
14b	106	0.95	coarse

Table 12. The values of $(u_{*m}-u_{*c})/W$ $(r = D_{50})$.

Chapter 7. Scouring Pattern for Relatively Fine Sand

7.1. Development of the Scouring Depth

The scouring pattern for relatively fine sand has troughs at the nodes and ridges at the antinodes of the standing waves. This type of bottom profile will be described in detail in Section 7.3.

The development of the scouring depth is shown in Fig. 27. The ordinate of the figure is the relative scouring depth Z_s/H, Z_s is the maximum depth of the trough of the scouring pattern at time t, and the abscissa is the relative time or the number of waves acting on the sand bed $N = t/T$. There are two series of curves in Fig. 27. One is for the condition of wave steepness $H/\lambda > 0.02$, and the other for $H/\lambda < 0.02$. Comparing the curves of $h/\lambda = 0.10$ with different H/λ, it can be seen that the final values of Z_s/H are almost the same, but the number of waves or the time needed to reach the final scouring depths are different. The flat waves ($H/\lambda < 0.02$) need more time than the steep waves ($H/\lambda > 0.02$), because the energy of the flat waves is less than that of the steep waves when λ and T are the same.

The number of waves required to reach the final scouring depth $N_{max} = t_{max}/T$ is about 6,500 to 7,500 for $H/\lambda > 0.02$, and about 7,500 to 10,000 for $H/\lambda < 0.02$ dependent on the relative water depth h/λ. The dashed lines linking the values of N_{max} on different curves with different h/λ are also shown in Fig. 27. The relative scouring depth increases very rapidly at first, reaching half of its ultimate value Z_{sm}/H in the first 1,000 to 2,000 waves, Z_{sm} is the ultimate value of Z_s when the equilibrium bottom profile is reached.

The test data obtained from different water depth shown in Fig. 28 indicate that h has no obvious influence on the development of the relative scouring depth Z_s/H for the same h/λ.

7.2. Maximum Depth of the Scouring Trough

The ultimate maximum depth of the scouring trough Z_{sm} and Z_{sm}/H are listed in Table 13.

Z_{sm}/H is expressed as function of h/λ in Fig. 29. All the test points except No. 2b are quite close to each other, and an experimental curve can be drawn.

No.	D_{50} (μm)	H (cm)	H/λ	h/λ	Z_{sm} (cm)	Z_{sm}/H
1a	106	5.0	0.0292	0.175	1.3	0.26
2a	106	7.5	0.0375	0.150	2.8	0.37
3a	106	5.5	0.0229	0.125	2.8	0.51
5a	106	5.5	0.0183	0.100	4.0	0.73
6a	106	9.0	0.0300	0.100	6.5	0.72
7a	106	5.0	0.0125	0.075	5.0	1.00
2b	200	9.0	0.0225	0.075	8.0	0.89
15b	106	6.0	0.0180	0.150	2.2	0.37
16b	106	8.5	0.0255	0.150	3.0	0.35
17b	106	7.5	0.0150	0.100	5.0	0.67
18b	106	10.0	0.0200	0.100	7.0	0.70
19b	106	8.0	0.0120	0.075	7.5	0.94

Table 13. Z_{sm} and Z_{sm}/H.

The results of tests No. 5a, 6a, 17b and 18b with $h/\lambda = 0.10$ as well as tests No. 2a, 16b and 17b with $h/\lambda = 0.15$ show that the wave steepness H/λ has no obvious influence on that function. The exception of test No. 2b may not be explained as the influence of sand grain size, since the wave profile in the flume was rather irregular for this test run. Even at the beginning of this test, the wave profile has shown some irregularity. When the scouring depth developed reaching about 5 cm, it could be observed that the reflected waves met the incoming waves at the place of scouring troughs, i.e. at the "nodes" of the standing waves, sending up a fountain of spray. No wonder that this phenomenon would influence the value of Z_{sm} of test No. 2b. The influence of sand grain size, water depth as well as wave steepness on the function of Z_{sm}/H is discussed in detail in Chapter 8.

The curve shown in Fig. 29 means that the ultimate maximum scouring depth Z_{sm} is dependent on wave height as well as on relative water depth. It seems to be reasonable that Z_{sm}/H decreases with increasing h/λ. It can be expected that there will be no scouring in relatively deep water. The test data in Fig. 29 can be expressed by a formula, i.e.

$$Z_{sm} = \frac{0.4\ H}{(\sin h\ 2\pi \frac{h}{\lambda})^{1.35}} \qquad (10)$$

It is not intended to extrapolate the test result to shallower water using eq. 10, since some properties of the standing waves in very shallow water, which may be important to the local scour problem, have not yet been understood fully. On the other hand, the test result might be extrapolated to deeper water a bit. Eq. 10 is also shown in Fig. 29. Z_{sm} is an important parameter in this problem, but when the time required to reach the equilibrium condition is considered, Z_s in any time for different h/λ may be important as well. Because N_{max} = 6,500 ~ 10,000 as described in Section 7.1, for T = 6 ~ 10 sec, t_{max} = 10.8 ~ 33.3 hr in nature, which may be longer than the time of the most severe storm in some regions. When all the test data in Fig. 27 are put in a figure of Z_s/Z_{sm} versus t/t_{max} (Fig. 30), then a relationship can be established, i.e.

$$\frac{Z_s}{Z_{sm}} = \left(\frac{t}{t_{max}}\right)^{0.3} \tag{11}$$

For any known H, T, h, λ and t, N_{max} is first obtained by interpolation from Fig. 27 using h/λ. Then Z_{sm} and Z_s can be obtained by Fig. 29 or eq. 10 and by Fig. 30 or eq. 11 using the known t_{max}.

7.3. Bottom Profile

Figs. 31 to 34 show the bottom profiles of tests No. 1a to 3a, 5a to 7a, 16b and 17b in the range of $\lambda/2$ from the wall. They have been smoothed out, so that the ripples are not shown on the profiles.

The sand eroded from the nodes is deposited near the antinodes. The tops of the deposited ridges are not at the antinodes for test No. 1a (Fig. 31) as well as for test No. 15b, for which the values of $(u_{max}-u_{crit.})/W$ are just a little higher than the critical value 16.5 (Table 11), but the tops of the ridges are almost always at the antinodes for the other test runs. For tests No. 6a and 7a, the positions of the maximum depths of the eroded troughs do not coincide with the nodes. In these cases, however, the depths at nodes are still marked as Z_{sm}, otherwise the distances between the places of the maximum depths of any two adjacent troughs will not be equal to $\lambda/2$.

Two theoretical curves, the sinusoidal curve and the trochoid, have been used to compare with the measured profile (Figs. 31 to 34). Neither of them is very close to the measured profiles. Owing to the fact that the scouring troughs are usually broader and flatter than the ridges, more or less like the waves forming the scouring patterns, the trochoid

fits the bottom profiles better than the sinusoidal curve does, especially in the left part of the figures, which is the part near the wall. When the trochoid is accepted to predict the scouring pattern as an approximation, then the following equations should be used:

$$x_t = \frac{\lambda}{4\pi}\theta + R \sin\theta \tag{12}$$

$$Z_t = -R \cos\theta \tag{13}$$

Where x_t and Z_t are horizontal and vertical coordinates of the curve respectively. x_t is measured from the node, and Z_t is measured from a height Z_o above the original flat sand bed positive upward.

$$R = \frac{1 - \sqrt{1 - \frac{8\pi}{\lambda} Z_{sm}}}{\frac{4\pi}{\lambda}} \tag{14}$$

$$Z_o = R - Z_{sm} \tag{15}$$

θ is from 0 to 2π.

When Z_s is used instead of Z_{sm} in eqs. 14 and 15, the bottom profile at any time will also be obtainable.

A theoretical bottom profile derived from the equation of continuity for local scour will be given in the following Section, which may explain why the scouring trough is broader and flatter than the deposited ridge and why the trochoid can be used as an approximation to fit the measured profile.

7.4. Mechanism of Sand Transport

Bijker et al (1971, 1976) explained the mechanism of sand transport when the majority of sand is moved as suspended load. Sand particles will be moved according to the circulation pattern of mass transport in the standing waves. This means that the direction of sand transport is from node to antinode as that of the net current near the bottom. In the following, the mass transport is assumed as the driving current for sand transport at first, then a theoretical scouring profile can be obtained which is similar to the measured one. Such a derivation may complement the above explanation.

Hattori (1969, 1971) measured the concentration of suspended sediment in the standing waves, and showed that there was a high concentration layer near the bottom. This high concentration layer has also been observed in the present tests. Assuming that the sand transport rate S in this layer z_c can be expressed as:

$$S = C_x U(x) z_c \tag{16}$$

in which C_x is the average value of the time-mean concentration in z_c, and $U(x)$ is the time-mean driving velocity.

An one dimensional expression obtained by Hattori (1969) is:

$$C_x = C_o \exp[\alpha (1 - \cos Kx)] \tag{17}$$

in which C_o is the reference concentration at $x = 0$, and α is a parameter; both of them should be determined experimentally. Equation 17 indicates that the concentration is minimum at the nodes and maximum at the anti-nodes.

For the local scour problem, the equation of continuity is:

$$\frac{\partial Z}{\partial t} = \frac{\partial S}{\partial x} \tag{18}$$

where Z is the scouring depth, which is positive downward.

Assuming the mass transport as the driving current, eqs. 16, 17 and 2 are substituted into eq. 18, then

$$\frac{\partial Z}{\partial t} = z_c \left\{C_x \frac{\partial U(x)}{\partial x} + U(x) \frac{\partial C_x}{\partial x}\right\}$$

$$= z_c \{C_o \exp[\alpha (1 - \cos Kx)] (2K \bar{U}_{max} \cos 2Kx)$$

$$+ (\bar{U}_{max} \sin 2Kx) C_o \exp[\alpha (1 - \cos Kx)] (\alpha K \sin Kx)\}$$

$$= z_c C_o K \bar{U}_{max} \exp[\alpha (1 - \cos Kx)] \{2 \cos 2Kx + \alpha \sin Kx \sin 2Kx$$

$$= A \exp[\alpha (1 - \cos Kx)] (2 \cos 2Kx + \alpha \sin Kx \sin 2Kx) \tag{19}$$

$$A = \frac{3 \pi^3 H^2 C_o z_c}{T \lambda^2 \sin h^2 Kh} \tag{20}$$

A is constant for any particular wave condition. The result of eq. 19 is given in Fig. 35 to show the relative scouring rate along bottom profile. α is assumed as 0.2, which is lower than the values obtained by Hattori (1969, 1971) for light material. It is easy to understand from Section 7.1 and Fig. 27 that the scouring rate $\frac{\partial Z}{\partial t}$ should be a function of time t. Equation 19 is true only when the number of waves N is relatively small, because eq. 2 as well as eq. 17 is derived from a flat bottom.
The curve shown in Fig. 35 can also be looked upon as the shape of the scouring pattern as long as eq. 19 is valid, i.e. $\frac{\partial Z}{\partial t}$ is constant with time, since

$$Z = \int \frac{\partial Z}{\partial t}\, dt = \left(\frac{\partial Z}{\partial t}\right) t \qquad (21)$$

The bottom profile shown in Fig. 35 has some features which are similar to those of the measured profiles described in Section 7.3. The scouring trough is broader and flatter than the deposited ridge. The position of the point of zero scouring is near but a bit farther than $x = |\lambda/8|$. The height of the ridge at the antinode can be greater than the maximum scouring depth, however, this is only true for tests No. 2a, 3a and 6a (Figs. 31 to 33). The trochoid has all the features mentioned above, so it can conveniently be used as an approximation to describe the scouring profile. The similarity between the derived profile shown in Fig. 35 and the measured one may prove the assumption that the mass transport is the driving current in turn.

7.5. Influence of the Protective Layer

When there is a protective layer, such as rip-rap, on the sea bed in front of the breakwater, the scouring bottom profile will differ from that without the protective layer. Fig. 36 shows two equilibrium bottom profiles which one has a protective layer and the other has not under the action of the same wave condition. Z'_{sm} is the ultimate maximum depth of the first scouring trough from the wall when there is a protective layer on the sand bed.
Three special test runs have been conducted in the wave flume to investigate the influence of the different lengths of the protective layer L on the scouring bottom profiles. The wave condition of tests No. 8a, 9a and 10 a is the same as that of test No. 5a (Table 1), and L = $\lambda/8$, $\lambda/4$, 3 $\lambda/8$ respectively. The protective layer consists of coarse sand and 1 ~ 2 cm crushed stones, the thickness of which is 3 cm.

The influence of the protective layer on the sand bed is mainly limited in a distance of $\lambda/2$ from the wall. Z'_{sm} decreases with increasing L, and the length of the scouring trough also decreases with increasing L. The distance from the wall to the first scouring trough increases with L. There is essentially no scouring over a distance of $\lambda/2$ from the wall when $L = 3\lambda/8$. Fig. 37 shows Z'_{sm}/Z_{sm} versus L. The detailed bottom profiles for $L = \lambda/8$ and $\lambda/4$ are shown in Fig. 38. For simplicity, both profiles consist of straight lines. The eroded volumes are not balanced by the accreted volumes, partly because Z'_{sm} are taken from the curve in Fig. 37 instead of the actual measured values.

7.6. Result of the Test Started with A Non-Flat Bottom

It may be easy to imagine what will occur on the bottom when only the wave height is changed, as long as the change of the value of $(u_{max}-u_{crit.})$ or $(u_{*m}-u_{*c})/W$ does not make it possible to change the type of the scouring pattern. If a train of waves with height H_2 and period T acts on the equilibrium profile of H_1 and T, this will remain unchanged when $H_2 < H_1$. When $H_2 > H_1$, it will develop further until the new equilibrium condition corresponding to H_2 is reached.

If both the wave height and period are changed from H_1, T_1 to H_2, T_2, the positions of nodes and antinodes will be changed too. This will make the situation more complicated than the former case.

Test No. 4a was done beginning at the equilibrium profile of test No. 7a (Table 1). $H_1 = 5.0$ cm, $T_1 = 2{,}41$ sec, $\lambda = 400$ cm for No. 7a and $H_2 = 5.5$ cm, $T_2 = 1.53$ sec, $\lambda_2 = 240$ cm for No. 4a. The position of the third node from the wall of No. 4a coincides with that of the second node of No. 7a (Fig. 39). The second node of No. 4a is close to the position of the top of the deposited ridge of No. 7a, which is not exactly at the antinode of this case. And the first node of No. 4a is near the edge of the first scoured trough of No. 7a.

The ultimate maximum scouring depth of the first and third trough of test No. 4a were reached in 5 hours. The former deposited ridge at the second node was eroded very fast at the beginning, the scouring heights was 2.5 cm in 1 hour. Then the rate of the scouring decreased. The scouring height was 3.5 cm in 5 hours. And the scouring height was 4.0 cm in

10 hours when the equilibrium condition was reached. The bottom elevation at the second node was still 0.9 cm higher than the original horizontal sand bed.

The equilibrium profile of test No. 3a is also shown in Fig. 39. It can be seen that the ultimate maximum scouring depth of No. 4a (Z_{sm} = 4.0 cm) is less than that of No. 7a (Z_{sm} = 5.0 cm), but greater than that of No. 3a (Z_{sm} = 2.8 cm). This means that when the greater scouring depth is created by the storm waves, it is difficult to fill in the scouring trough according to the condition of the other waves.

The difference of the results between tests No. 4a and 3a may be attributed to the influence given by the scouring pattern of test No. 7a on the waves as well as on the orbital velocities near the bottom of test No. 4a.

Chapter 8. Scouring Pattern for Relatively Coarse Sand

8.1. Development of the Scouring Depth

The scouring troughs occur halfway between nodes and antinodes, and the ridges at the nodes of the standing waves for relatively coarse sand. This type of bottom profile will be described in detail in 8.3.
The development of the scouring depth is shown in Fig. 40. It is more or less like Fig. 27 for relatively fine sand. The number of waves required to reach the final scouring depth N_{max} is about 7,000 for $H/\lambda > 0.02$, and about 6,500 to 10,000 for $H/\lambda < 0.02$ dependent on the relative water depth h/λ. The relative scouring depth increases very rapidly at first, reaching half of its ultimate value Z_{sm}/H in about 2,000 waves.
It has been mentioned in Chapter 6 that the mixed type of scouring pattern occured in tests No. 13a to 15a for D_{50} = 150 μm. In such a case, only the depths of the scouring troughs halfway between nodes and antinodes are used in this Chapter.
Intending to investigate the influence of sand diameter or water depth on the development of the scouring depth, the test data of No. 15a and 12b are put into a figure. Fig. 41 shows that D_{50} or h has no obvious influence on the development of Z_s/H for the same h/λ, as long as H/λ is close to each other.

8.2. Maximum Depth of the Scouring Trough

Fig. 42 shows Z_{sm}/H versus h/λ for all the test data with different D_{50}, h as well as H/λ. The test data are rather scattered, but there is no obvious influence of D_{50} or h in that figure. The general tendency is that Z_{sm}/H decreases with increasing h/λ, which is the same as that of relatively fine material. The only two exceptions are the test points of No. 19a and 20a, which have been repeated in the large flume. The curve of Z_{sm}/H as a function of h/λ drawn in Fig. 42 is rather an envelope with a few exceptions around $h/\lambda = 0.10$. Fig. 43 shows that Z_{sm}/H tends to increase a bit with the wave steepness H/λ, however, this influence is hardly significant.
The experimental curve in Fig. 29 for relatively fine material is reproduced in Fig. 42. The maximum scouring depth for scouring pattern Type "fine" is greater than that of Type "coarse", as there is only one scouring trough in half wave length $\lambda/2$ for the former and there are

two troughs in $\lambda/2$ for the latter.

When all the test data in Fig. 40 are put in a figure of Z_s/Z_{sm} versus t/t_{max} (fig. 44), then a relationship can be obtained, i.e.

$$\frac{Z_s}{Z_{sm}} = \left(\frac{t}{t_{max}}\right)^{0.4} \tag{22}$$

Eq. 22 is a bit different with eq. 11 in Section 7.2 for relatively fine material.

8.3. Bottom Profile

For scouring pattern Type "coarse", the sand eroded halfway between the nodes and the antinodes is deposited at the nodes. It has already been shown in Chapter 4 that the sand ripples did not cover the bed and the bottom level did not change over a distance l_r measured from the antinode. The values of l_r are different for different D_{50} under the same wave condition (Table 6), so that the bottom profiles of the finer sand seem to be quite different from those of the coarser sand at first sight. Only when a length parameter $l_* = \frac{\lambda}{4} - l_r$ is introduced, then the mean bottom profile of Type "coarse" for different D_{50} can be given as it is shown in Fig. 45 and Table 14. The scouring trough is represented by a sinusoidal curve, and the eroded volume is balanced by the accreted volume.

X	0	0.1 l_*	0.2 l_*	0.3 l_*	0.4 l_*	0.46 l_*	0.5 l_*
Z	-1.0 Z_{sm}	-0.99 Z_{sm}	-0.91 Z_{sm}	-0.70 Z_{sm}	-0.31 Z_{sm}	0	0.23 Z_{sm}
X	0.6 l_*	0.7 l_*	0.73 l_*	0.8 l_*	0.9 l_*	1.0 l_*	
Z	0.73 Z_{sm}	0.98 Z_{sm}	1.0 Z_{sm}	0.92 Z_{sm}	0.55 Z_{sm}	0	

Table 14. Coordinates of the bottom profile.

Where X and Z are horizontal and vertical coordinates of the curve respectively. X is measured from the node, and Z is measured from the original flat bottom positive downward. Three measured bottom profiles with different D_{50} and h are also shown in Fig. 45 as examples.

Bijker et al (1976) explained the mechanism of sand transport for relatively coarse material which is caused by small asymmetry in orbital motion.

Chapter 9. Scale Laws

9.1. Scale Law for the Sand Grain Size

It has already been shown in Chapter 6 that $(u_{max}-u_{ctit.})/W$ is an important parameter to distinguish two basic types of scouring pattern. It means that this parameter in model should be kept the same as that in prototype, or at least in the same category. Generally the trial and error method has to be used to determine the scale of the sand diameter, since both $U_{crit.}$ and W are functions of D_{50}. An example will be given in the following table. n will be used to denote the scale, i.e. the ratio between the values of a certain quantity in model and in prototype. A subscript to n refers to the quantity concerned. For instance, n_l is the length scale. It is well known that in an undistorted model

$$n_h = n_H = n_\lambda = n_l \tag{23}$$

and

$$n_T = n_u = n_{\bar{U}} = n_l^{1/2} \tag{24}$$

In Table 15, the sand diameter in model is the result of calculation. $u_{crit.}$ is obtained from the Bagnold formula (Table 8), which does not follow the scale of u.

	h (m)	H (m)	λ (m)	T (s)	u_{max} (m/s)	D_{50} (μm)	W (m/s)	u_{crit} (m/s)	u_{max}
prototype	10	4.0	8.0	8.84	3.27	500	0.073	0.26	41
model	0.5	0.2	4.0	1.98	0.73	150	0.015	0.078	42

Table 15. Scale of the sand diameter ($n_l = 1/20$).

From Table 15,

$$n_D = \frac{150}{500} = 0.3 \cong n_l^{0.4}$$

u_{max} is much larger than $u_{crit.}$ for most of the design conditons under severe storm waves. If $(u_{max}/W)_m = (u_{max}/W)_p$ instead of $(\frac{u_{max}-u_{crit.}}{W})_p$ is considered as an approximation, the subscripts m and p denote the parameter in model and in prototype respectively, then

$$n_W = n_u = n_l^{1/2} \tag{25}$$

$Re = W D_{50}/\nu$ is the grain size Reynolds Number, in which ν is the kinematic viscosity of water. For finer sand, $Re < 10^0$, which is corresponding to $D_{50} < 100$ μm when the temperature of water is about 20 degrees centrigrade, the well known Stokes equation for the fall velocity W is valid, i.e.

$$W \propto D_{50}^2 \tag{26}$$

$$n_w = n_D^2 \tag{27}$$

Then:

$$n_D = n_l^{1/4} \tag{28}$$

For coarser sand, $Re = 10^0 \sim 10^3$, i.e. D_{50} is smaller than about 2500 μm,

$$W \propto D_{50} \tag{29}$$

$$n_D = n_W = n_l^{1/2} \tag{30}$$

For the even coarser material, such as gravel, $w \propto D_{50}^{1/2}$, then n_D will follow the length scale n_l.
Generally speaking, the scale for the sand grain size n_D ranges from $n_l^{1/4}$ to $n_l^{1/2}$.

9.2. Scale Law for the Scouring Depth

When the dynamic equilibrium condition is reached for the sand bed composed of relatively fine material under the action of standing waves, the equation of mation of the sand particle along the slope can be established as:

$$\frac{W_s}{g}\frac{du_s}{dt} = F_d - F_g - F_f \frac{F_d - F_g}{|F_d - F_g|} \tag{31}$$

in which $W_s = (\rho_s - \rho)\, g\, \frac{\pi D_{50}^3}{6}$ is the weight of the sand particle in water, u_s is the velocity of the sand particle along the slope, and F_d, F_g and F_f are the drag force, the component of the gravitational force and the friction force respectively.

$$F_g = W_s \sin \alpha \tag{32}$$

in which α is the angle of the deformed sand bed with horizontal at the place where the ultimate scouring depth Z = 0 in particular (Fig. 46).

$$F_d = \frac{1}{2} \rho\, C_D\, \frac{\pi D^2}{4}\, (u_\alpha - u_s)\, |u_\alpha - u_s| \tag{33}$$

in which C_D is the coefficient of drag, and u_α is the velocity of water along the slope. Considering the velocity of water on a flat bottom, it may be reasonable to assume:

$$u_\alpha = u_o + u_2 \cos \omega t \tag{34}$$

The sand particle will move only when the velocity of water exceeds the critical velocity for the sand particle. The variation of the velocity of the sand particle with time is shown in Fig. 47. As an approximation, it can be assumed that

$$u_s = u_3 \cos \omega t \tag{35}$$

From eqs. 34 and 35, then

$$u_\alpha - u_s = u_o + u_1 \cos \omega t \tag{36}$$

where $u_1 = u_2 - u_3$.

According to Eagleson and Dean (1959), the coefficient of drag can be expressed as $C_D = C_1/Re$ when the Reynolds Number Re is smaller than about 100, where C_1 is a constant, and $Re = (u_\alpha - u_s)\, D_{50}/\nu$, i.e.

$$C_D = \frac{C_1\, \nu}{(u_\alpha - u_s)\, D_{50}} \quad (\text{for } Re < 100) \tag{37}$$

and C_D is almost a constant when Re is larger than about 1,000, i.e.

$$C_D = C_2 \quad (\text{for } Re > 1{,}000) \tag{38}$$

where C_2 is a constant.

When eqs. 36 and 37 or 38 are substituted into eq. 33, the net drag force on the sand particle is able to be obtained by integration of eq. 33 over one complete wave cycle:

$$f_d = \rho\, C_D \frac{\pi D_{50}^2}{8} u_o^2 \qquad \text{(for } Re < 100\text{)} \tag{39}$$

or

$$f_d = \rho\, C_D \frac{D_{50}^2}{2} u_o\, u_1 \qquad \text{(for } Re > 1{,}000\text{)} \tag{40}$$

The derivations of eqs. 39 and 40 are presented in Appendix 2 in detail. Dealing with the net drag force, Eagleson and Dean (1959) have proved with tests of beach slope under progressive waves that the mass transport velocity, i.e. u_o, instead of the relative instantaneous velocity should be used determining Re as well as C_D.

The friction force can be adsorbed when the coefficient of drag is obtained on a sand slope instead of a smooth plane boundary.

The net acceleration of the sand particle in one wave period is zero for the dynamic equilibrium condition. Then, from eqs. 32 and 39, eq. 1 becomes

$$\frac{3\, C_D\, u_o^2}{4\, \Delta\, g\, D_{50}} = \sin\alpha \tag{41}$$

For wave-induced motion of the sand particle along a sand slope $C_D = 19.2/Re$ as long as $Re < 100$. Therefore

$$\frac{14.4\, \nu\, u_o}{\Delta\, g\, D_{50}^2} = \sin\alpha \tag{42}$$

Further, when $\nu = 10^{-6}$ m^2/s, $\Delta = 1.65$ and $g = 9.81$ m/s^2 are taken, then

$$8.90 \times 10^{-7} \frac{u_o}{D_{50}^2} = \sin\alpha \tag{43}$$

For any particular test run, D_{50} is known and α is able to be measured from the bottom profile, thus u_o is obtainable (Table 16).

In Table 16, Re has been checked and u_o compared with $\bar{U}_{max}$, i.e. the theoretical mass transport velocity at the bottom halfway between node and antinode as given by eq. 2. It should be pointed out that $Re < 100$ can be satisfied in most of prototype conditions.

Equation 43 shows that the slope of the equilibrium profile depends on a dimensional parameter u_o/D_{50}^2. u_o/D_{50}^2 versus tan α is shown in Fig. 48. These two parameters should have a good relationship since α is small.

No.	D_{50} (μm)	α (degree)	$\frac{u_o}{D_{50}^2}$ $(\frac{1}{m.s})$	u_o (cm/s)	Re	$\bar{U}_{max}$ (cm/s)	$u_o/\bar{U}_{max}$
1a	106	7	1.37×10^5	0.15	0.159	1.04	0.144
2a	106	13.5	2.62×10^5	0.29	0.307	2.65	0.109
3a	106	8	1.56×10^5	0.17	0.180	1.62	0.105
5a	106	10	1.95×10^5	0.22	0.233	1.83	0.120
6a	106	18	3.47×10^5	0.39	0.413	4.90	0.080
7a	106	9	1.76×10^5	0.20	0.212	1.61	0.124
2b	200	14	2.72×10^5	1.09	2.18	5.20	0.210
15b	106	6	1.17×10^5	0.13	0.138	0.80	0.163
16b	106	8	1.56×10^5	0.17	0.180	1.60	0.113
17b	106	8	1.56×10^5	0.17	0.180	1.54	0.117
18b	106	11	2.14×10^5	0.24	0.254	2.74	0.088
19b	106	9	1.76×10^5	0.20	0.212	1.90	0.105

Table 16. The values of u_o.

From Fig. 48, the scale of tan α of the equilibrium profile:

$$n_{\tan\alpha} = n_{(u_o/D^2)} \tag{44}$$

$n_{u_o} = n_l^{1/2}$ from eq. 24, and $n_D = n_l^{1/4}$ from eq. 28 for fine material, therefore

$$n_{\tan\alpha} = 1 \tag{45}$$

Since $\tan\alpha = Z/l$ (Fig. 46), then

$$n_Z = n_l \tag{46}$$

This means that the scale of the scouring depth will follow the length scale. The dimensionless form of the maximum scouring depth obtained from different water depths, i.e. Fig. 29 or eq. 10 in Section 7.2 supports this conclusion.

The dimensionless form of the maximum scouring depth obtained from different sand grain sizes and different water depths for relatively coarse sand, i.e. Fig. 42 in Section 8.2 reveals that eq. 46 is also true for coarser material even though the mechanisms of sand movement for coarser and finer material are quite different.

It is interesting to cite that Breusers, Nicollet and Shen (1977) concluded on the basis of the evidences obtained from the laboratory and from the field that for the local scour around bridge pier in a current, the depth of scour can be regarded as a function of the geometry alone and can also be treated like any other length in the comparison of model and prototype.

The reduction of the mass transport velocity from $\bar{U}_{max}$ to u_o, and also the reduction of the orbital velocity near the bottom as indicated in Section 3.2 may explain why eventually an equilibrium profile can be reached.

Chapter 10. Scouring Pattern under Irregular Waves

10.1. Waves and Wave Spectra

Only three test runs (tests No. 1c, 2c and 3c in Table 2) were carried out in the large flume with D_{50} = 106 μm with irregular waves. It is impossible to measure the incident wave trains and their spectra in front of the wall directly, since the distance between the wall and the wave board is only 9-13 times the mean wave lengths in the tests. The vertical wall is regarded as a total reflection barrier for the waves. The standing wave height can be measured at any antinode in front of the wall in regular waves, but it can only be measured on the front surface of the wall in irregular waves. Since the various wave components in the incident wave train as well as in the reflected wave train have different wave lengths, they propagate with different celerities. The crests of the various incident and reflected wave components will not meet at the same fixed positions except direct on the surface of the wall. One example of the records of the irregular standing waves is shown in Fig. 49a.

The "zero-up-crossing" method is adopted to determine the wave height and period of the individual wave from the records. The half of every standing wave height is taken as the individual incident wave height. The Rayleigh Distribution is generally accepted to described the statistical property of wave heights in deep water, which can be expressed as:

$$P_H = \exp\left[-\frac{\pi}{4}\left(\frac{H_p}{\bar{H}}\right)^2\right] \tag{47}$$

where P_H is the probability of exceedance of wave height H_p, and $\bar{H}$ is the mean wave height.

In relatively shallow water, however, an empirical distribution has been proposed, and it has been introduced and applied by Lates (1963). This distribution can be expressed as:

$$P_H = \exp\left[-\frac{\pi}{4\left(1+\frac{h*}{\sqrt{2\pi}}\right)}\left(\frac{H_p}{\bar{H}}\right)^{\frac{2}{1-h*}}\right] \tag{48}$$

where $h* = \bar{H}/h$. Equation 48 will approach eq. 47 when $h*$ approaches zero. The statistical properties of wave heights of tests No. 1c, 2c and 3c have been compared with the results of eqs. 47 and 48 in Fig. 50. It seems that eq. 48 describes the wave properties in the flume better than eq. 47 does.

The wave spectra measured at the antinodes of the standing waves are shown in Figs. 51 to 53. It should be mentioned that the energy densities of the incident waves are only one quarter of that S(f) shown in these figures. From these figures, it can be seen that the spectra measured at different time of every test run are not exactly the same. The shapes, the peak values of the energy density, the frequencies of the peak and the total energies of these spectra are, within certain limits, changing continuously. It has already been known from the tests with regular waves that the relative water depth h/λ, or the wave period T is an important factor determining the position and depth of the scouring hole. The variation of the peak frequency f_m, or the peak period T_m is considered to be acceptable if the maximum scouring depth Z_s still increases with time. Besides, the variation of the significant wave height H_s should not exceed $\pm$ 10%. Tests No. 1c and 3c satisfy above requirements until the equilibrium condition is reached. Unfortunately, that is not the case for test No. 2c. That test run has to be finished in the fifth hour.

The measured spectra have been compared with the JONSWAP (Joint North Sea Wave Project) spectra given by:

$$S(f) = \alpha \frac{g^2}{(2\pi)^4} \frac{1}{f^5} \exp\left[-1.25 \left(\frac{f_m}{f}\right)^4\right] \gamma^{\exp\left[-\frac{(f-f_m)^2}{2\sigma^2 f_m^2}\right]} \tag{49}$$

in which S(f) is the energy density ($m^2 s$), f is the frequency (Hz), the peak frequency

$$f_m = 3.5 \frac{g}{U} \left(\frac{gF}{U^2}\right)^{-0.33} \tag{50}$$

U is the wind speed (m/s), F is the fetch length (m),

$$\alpha = 0.076 \left(\frac{gF}{U^2}\right)^{-0.22} \tag{51}$$

$$\sigma \begin{cases} \sigma_a = 0.07 & \text{for } f \leq f_m \\ \sigma_b = 0.09 & \text{for } f > f_m \end{cases}$$

Generally, γ is taken as 3.30 as the mean value, however, Ochi (1979) proposed a family of spectra with γ from 1.75 to 4.85. He also gave a formula relating U and H_s as:

$$U = K F^{-0.615} H_s^{1.08} \tag{52}$$

Where K is a constant, which equals 96.2, 83.7 and 76.4 when γ equals 1.75, 3.30 and 4.85 respectively.

Considering that the JONSWAP spectra are obtained from deep water wave data, the lowest value $\gamma = 1.75$ is selected in the comparison with the measured spectra. Fig. 51a shows one example of these comparisons. S(f) shown in the figure is four times that calculated by eq. 49, since it represents the standing wave condition. The measured spectrum is a little narrower than the theoretical one, especially the energy density of the higher frequency part of the former is lower than the latter.

The total energies of the spectra at different distances from the wall l have been measured from the autocorrelation functions displayed by the Correlator. In Fig. 54, the ordinate is the ratio of the energy at distance l and that at $l = 0$, and the abscissa is the distance l, λ is the wave length calculated from the mean wave period $\bar{T}$ via

$$\lambda = \frac{g\bar{T}^2}{2\pi} \tan h \frac{2\pi h}{\lambda} \tag{53}$$

The ratio of T_m and $\bar{T}$ is from 1.05 to 1.21, and its mean value is 1.13. These are obtained from 10 records of tests No. 1c, 2c and 3c.

It can be seen from Fig. 54 that the energy ratio decreases rather fast with increasing l. The energy reaches half of that measured close on the wall, i.e. double the energy of the incident waves, at a distance about 4λ from the wall, and then remains almost constant. In other words, the 'nodes' and 'antinodes' vanish completely when $l \geq 4\lambda$. The wave spectrum measured at $l_2 = 20.2$ m or 6λ is compared with that measured at $l_1 = 0$ for test No. 1c in Fig. 51f. The shapes of these two spectra are quite similar.

The wave pattern in front of a wall with irregular waves is definitively different from that with regular waves. Such a difference will surely influence the scouring pattern of the sand bed which is described in Section 10.3.

10.2. Orbital Velocities and Velocity Spectra

The horizontal components of the orbital velocities at a distance $\lambda/4$ from the wall, i.e. the node, near the bottom under irregular waves have been measured in test No. 2c. One of the examples is shown in Fig. 49b. On the whole, the wave profile and the corresponding velocity profile are rather similar. But occasionally, there is only one 'wave' in the velocity record when there are two waves in the wave record when the zero-up-

crossing method is adopted as shown on the right side of both records in Fig. 49.

The statistical property of the orbital velocities has also been calculated, and compared with that of the wave heights measured at the same time as well as with the Rayleigh Distribution in Fig. 55. The ratio of u_p and $\bar{u}$ is smaller than that of H_p and $\bar{H}$ when the probability of exceedance P_u or P_H is smaller than about 8%, where $\bar{u}$ is the mean velocity, and u_p is the velocity, the probability of exceedance of which is P_u. The wave height records are easier to be obtained than the orbital velocity records, especially in reality, therefore it will be interesting if u_p is able to be obtained from H_p. In Table 17. $u_{p.c}$ and $u_{p.m}$ are compared, the extra subscripts c and m represent the calculated and measured values respectively. $u_{p.c}$ is calculated by:

$$u_{p.c} = \frac{2\pi H_p}{\bar{T}} \frac{\cos h \frac{2\pi}{\lambda}(z + h)}{\sin h \frac{2\pi}{\lambda} h} \tag{54}$$

(53)

in which λ is obtained from eq. 53. The calculated mean velocity $\bar{u}_c$ = 29.5 cm/s, which is obtained by substituting $\bar{H}$ as H_p in eq. 54. The measured mean velocity $\bar{u}_m$ = 30.6 cm/s. The relative error $\frac{\bar{u}_m - \bar{u}_c}{\bar{u}_m}$ = 3.6%.

P_u (%)	1	2	5	10	13.5*	20
$u_{p.m}$ (cm/s)	57.6	55.8	51.4	46.0	43.3	40.6
$u_{p.c}$ (cm/s)	62.4	61.6	51.2	43.7	41.4	39.2
$\frac{u_{p.m}-u_{p.c}}{u_{p.m}}$ (%)	- 8.3	-10.4	0.4	5.0	4.4	3.4

Table 17. Comparison of $u_{p.c}$ and $u_{p.m}$.

*$u_{13.5\%}$ may be considered as the significant velocity u_s approximately since $H_{13.5\%} = H_s$ according to the Rayleigh Distribution.

It seems that eq. 54 can be applied at least when $P_u \geq 5\%$, the relative error of which is within 5%.

The velocity spectra have also been measured at $1 = \lambda/4$, z_b = 10 cm in test No. 2c. It should be pointed out that the velocity measured by the Spectrum Display is neither the spectrum of $(u_i)_+$ nor that of $(u_i)_-$, but the spectrum of $(u_i)_+ + |(u_i)_-|$ when the velocity profile like that shown in Fig. 49b is used as the input data. $(u_i)_+$ and $(u_i)_-$ are the horizontal velocity components, the directions of which are towards the wall and the wave board respectively.

If $(u_i)_+ = (u_i)_-$ is assumed as in the regular wave cases, then the measured spectra can be regarded as the spectra of $(u_i)_+$ as well as the spectra of

$(u_i)_-$ when the scale of the ordinate is divided by four. One example is shown in Fig. 56.

The velocity spectrum can also be obtained from the wave spectrum by the following equation when both of them are linear systems.

$$S(u) = K_u^2(f)\ S(f) \tag{55}$$

where S(u) is the horizontal velocity spectrum at a height z_b above the bottom at the node ($l = \lambda/4$, in m^2/s or cm^2/s), S(f) is the incident wave spectrum, in fact it is obtained from the standing wave spectrum by dividing the ordinate by four (in m^2s or cm^2s), $K_u^2(f)$ is the transfer function between these two spectra (in $1/S^2$), which can be expressed as

$$K_u^2(f) = 4\ \pi^2\ f^2\ \frac{\cos h^2\ K_i\ z_b}{\sin h^2\ K_i\ h} \tag{56}$$

where $K_i = 2\pi/\lambda_i$, and λ_i is the wave length corresponding to the different f.

The transfer function and the calculated velocity spectrum are also shown in Fig. 56. The calculated spectrum coincides quite well with the measured one. It should also be pointed out that S(f) and S(u) are not strictly synchronous records but are taken one after the other.

10.3. Scouring Pattern under Irregular Waves

The scouring pattern of the sand bed, which is several wave lengths in front of a vertical wall, under irregular waves is different with that under regular waves (Fig. 57).

The scouring profiles between any two adjoining antinodes are the same in a regular wave case. For the sand bed composed of relatively fine material under the action of irregular waves, the maximum depth of every scouring trough and the maximum height of every deposited ridge still occur roughly at the 'node' and 'antinode' positions corresponding to a wave length λ calculated by eq. 53, but the scouring depth as well as the deposited height decreases very fast with increasing distance l from the wall. From Fig. 54, the energy ratio is 83% at $l = \lambda/2$, or the wave height at that place is 0.91 of that at $l = 0$, but the maximum scouring depth of the second trough is only about 0.4 of that of the first one from the wall as shown in Fig. 57b. This is owing to the fact that the scouring depth is dependent not only on the wave height but also on the character of the waves. As it has already been described in Section 10.1, there is only one true antinode at $l = 0$ and there are no antinodes and

nodes at all when $l \geq 4\lambda$. The so called 'antinode' and 'node in the distance $4\lambda > I > 0$, in fact, are all imperfect.

Fortunately, the differences of the deposited heights at $l = 0$ and $l = \lambda/2$ are not so large, and the bottom profiles from $l = 0$ to $\lambda/2$ under the action of irregular waves can still be described by the trochoids as an approximation like in the regular wave cases in Section 7.3. The comparisons of the measured bottom profiles of tests No. 1c and 3c with the trochoids as well as the sinusoidal curves are shown in Fig. 58. It is shown in Chapter 11 with some typical examples that only the scouring profiles over a distance less than $\lambda/2$ from the wall are important to the stability of the foundation of the breakwater.

It is important to difine an equivalent wave height, with certain statistical meaning, in an irregular wave train. The effect of this train on the sand bed, the ultimate maximum depth of the scouring trough Z_{sm} in particular, is the same as the effect of a regular wave train with the height which is equal to the equivalent wave height.

In Table 18, the Z_{sm}/H values are obtained at first from the curve for the regular wave cases in Fig. 29 in Section 7.2. according to the h/λ values of tests No. 1c and 3c. Z_{sm} of these two irregular wave test runs are measured from the bottom profile records, then the equivalent wave heights are obtained, and their values of the probability of exceedance P_H is able to be found in Fig. 50 since the mean wave heights $\bar{H}$ of the tests are known.

No.	h/λ	Z_{sm}/H (from Fig. 29)	Z_{sm} (cm)	equivalent wave height H (cm)	P_H (%)
1c	0.148	0.38	2.7	7.1	30
3c	0.111	0.62	3.0	4.8	48

Table 18. Equivalent wave heights.

In Fig. 59, the ratios of Z_{sm} and H_s as well as Z_{sm} and $\bar{H}$ are given with the curve of Z_{sm}/H versus h/λ reproduced from Fig. 29 as reference.

The significant wave height H_s is commonly taken as the equivalent wave height in designing rubble mound breakwaters, although some different conclusions can be found in the different test reports. Dealing with coastal sediment problems, Sato et al (1968) used significant wave heights as the equivalent wave heights in comparing the maximum scouring depths measured from field with those obtained from the regular wave tests in front of the seawall installed on a beach. Van Hijm (1976) reported that good

results were obtained in predicting the longshore transport rates of a natural gravel beach by characterizing the wind wave fields with significant wave heights.

Of course, it is impossible to obtain the equivalent wave height for the local scour problem concerned in this paper definitely only by a few test runs with irregular waves. However, from Table 18 and Fig. 59, it may be said roughly that the equivalent wave height is between $\bar{H}$ and H_s. For the time being, H_s is recommended as the equivalent wave height as it is on the conservative side.

The critical velocities for sand particles $u_{crit.}$, the sand ripple heights and lengths, H_r and λ_r, and the values of the parameter $(u_{max}-u_{crit})/W$ can all be checked up, when H_s is assumed as the equivalent wave height and the significant value of u_{max} is calculated by substituting H_s as H_p in eq. 54. The distance l_r which has been used in Chapter 4 to determine $u_{crit.}$ is only possible to be measured from the first antinode corresponding to the wall face in an irregular case. l_r and $u_{crit.}$ of tests No. 1c, 2c and 3c are listed in Table 19. The critical velocities $u_{crit.}$ of different wave periods $\bar{T}$ for D_{50} = 106 μm obtained under the irregular waves are comparable with those obtained under the regular waves in Fig. 21 in Chapter 4.

No.	$\bar{T}$ (sec)	l_r (cm)	u_{crit} (cm/s)	measured		calculated		$\frac{u_{max}-u_{crit}}{W}$	Type of scouring pattern
				H_r (cm)	H_r/λ_r	H_r (cm)	H_r/λ_r		
1c	1.72	15	8.0	1.4	0.20	1.0	0.18	29.9	fine
2c	1.98	16	8.5	1.5	0.18	1.0	0.18	35.3	fine
3c	1.69	9	8.0	1.0	0.17	0.9	0.18	38.4	fine

Table 19. u_{crit}, H_r, H_r/λ_r and $(u_{max}-u_{crit})/W$.

The ripple height H_r and the ripple steepness H_r/λ_r measured at the first node position from the wall in each test run are also compared with those calculated by eqs. 7 and 8 (Chapter 5) in Table 19. The measured values of H_r and λ_r are higher than the calculated values. This is as same as the condition with regular waves.

The values of $(u_{max}-u_{crit})/W$ listed in Table 19 shows that the criterion of $(u_{max}-u_{crit})/W \geq 16.5$ for relatively fine material given in Chapter 6 may also be applied to the irregular wave cases, although none of the values obtained are close to the critical value.

It seems that all the parameters for irregular wave cases are comparable with those for regular wave cases, except for the time required to reach the equilibrium condition, i.e. t_{max}. t_{max} in tests No. 1c and 3c are compared with t_{max} in tests No. 16b and 6a respectively, because they have the same D_{50}, h and close h/λ and H/λ (Table 20).

Comparison No.	Test No.	D_{50} (μm)	h (cm)	h/λ	H/λ	t_{max} (hr)
I	1c	106	50	0.148	0.0252	8.0
	16b	106	50	0.150	0.0255	3.5
II	3c	106	30	0.111	0.0263	8.0
	6a	106	30	0.100	0.0300	3.5

Table 20. Comparison of t_{max}.

The comparisons show that t_{max} for irregular waves is more than double that for regular waves. This is because in a regular wave case, the wave period T does not change with time, but in an irregular wave case, the peak period T_m as well as the mean wave period $\bar{T}$ changes with time at random as shown in Fig. 51 to 53. It is recommended to use t_{max} as well as the relationship between Z_s/Z_{sm} and t/t_{max} obtained from the regular wave tests rather than that obtained from the irregular wave tests, because the former is more reliable than the latter.

Chapter 11. Influences of the Scouring Patterns on the Stability of the Stability of the Foundations of the Vertical Breakwaters

Owing to the fact that some vertical breakwaters have been damaged by scouring of the sea beds in front of them, it is generally demanded extending a protective layer on the sea bed to a distance equal to $\lambda/4$ to $3\lambda/8$ in the design of breakwater.

When the scouring pattern in front of a vertical breakwater is known, it is possible to examine its influence on the stability of the foundation of the breakwater, and then decide whether a protective layer is necessary and how long its length should be.

The slip circle analysis, or so called method of slice is utilized in the calculation of the stability of the foundations in view of the complicated geometries of the deformed sand beds.

The scouring pattern will only influence the safety factor of the stability when the tendency of the slide is towards the seaside. In case the center of the failure circle is higher than the point where the wave force acts on the breakwater, the scouring of the sea bed will only influence the stability under the action of wave trough (Fig. 60). The safety factor can be expressed as:

$$F = \frac{R \tan \phi \sum_{i=1}^{n} W_i \cos \alpha_i}{P r_p - R \sum_{i=1}^{n} W_i \sin \alpha} \tag{57}$$

in which R is the radius of the slide circle, ϕ is the internal friction angle of the foundation soil, W_i is the weight of the ith slice, α_i is the angle between the gravitational force and the normal force on the arc of the circle, P is the wave force, and r_p is the arm of the wave force to the center of the circle.

A computer program considered in particular the influence of the scouring pattern has been worked out. This program can find out the minimum safety factor of the stability corresponding to the most dangerous slip circle in each case easily. Some examples are given in the following. The relative water depth h/λ will be varied from 0.075 to 0.125 in each case in Table 21. It should be pointed out that the probability of exceedance of the wave height H has not been defined specially in the examples. Different H_p values should be used for calculating wave force and scouring depth in practical design.

Case	h (m)	H (m)	B (m)	ϕ (degree)	Scouring type
1	10	4	8	25	fine
2	10	4	8	25	coarse
3	10	4	8	30	coarse
4	15	7	12	25	fine

Table 21. Different cases for stability analysis.

In Table 21, B is the width of the breakwater. The results of the calculation are shown in Fig. 61, in which F_1 denotes the safety factor of stability without scouring, and F_2 denotes the safety factor when the influence of the scouring pattern has been considered. Assuming the deposited ridge above the original flat sea bed may be washed out easily when there is a current along the axis of the breakwater, another situation is also taken into consideration, i.e. only the influence of the scouring trough is considered in the stability analysis. The safety factor obtained under this assumption is denoted as F_3. From Fig. 61, the following conclusions can be obtained:

1. The tendencies of variation of F_1, F_2, and F_3 with h/λ are the same for different h and H for scouring pattern Type "fine" (Fig. 61a and b). F_1 decreases a bit with decreasing h/λ owing to the fact that the wave force P increases with decreasing h/λ. Although the maximum scouring depth Z_{sm} increases with decreading h/λ (Fig. 29 in Chapter 7), F_2 increases with decreasing h/λ. F_2 are 3.5 and 3.6% less than F_1 for case 1 and 4 respectively when $h/\lambda = 0.125$. F_2 is almost the same as F_1 when $h/\lambda = 0.100$. F_2 are 14.3 and 10.2% larger than F_1 for case 1 and 4 respectively when $h/\lambda = 0.075$. This is because in relatively shallow water, or in other words when the wave length λ is relatively long, the distance of the scouring trough from the breakwater is larger. Then the beneficial influence of the deposited ridge can be more significant than the unfavourable influence of the scouring trough on the safety factor of stability (Fig. 60a). F_3 are 6.1 and 7.3% less than F_1 for case 1 and 4 respectively when $h/\lambda = 0.125$. F_3 is the same as F_1 when $h/\lambda = 0.075$, because the arc of the most dangerous slip circle does not cross the eroded part of the sea bed. This means that the shorter wave can be more dangerous for the same h and H for scouring pattern Type "fine".

2. Fig. 41c shows F_2 decreases with decreasing h/λ for scouring pattern Type "coarse" which is in contrast with scouring pattern Type "fine". F_2 are 5.3 and 20.5 % less than F_1 when h/λ = 0.125 and 0.075 respectively. This is because the scouring trough is near to the breakwater, and the maximum scouring depth Z_{sm} increases with decreasing h/λ (Fig. 42). F_3 is only a little bit less than F_2 when h/λ = 0.125. There is no difference between F_3 and F_2 when $h/\lambda \lesssim 0.100$, because the arc of the most dangerous slip circle does not cross the deposited part of the sea bed (Fig. 60b).

3. The reduction of the safety factor is more significant for scouring Type "coarse" than for scouring Type "fine" in relatively shallow water. Of course, this does not mean that the sea bed composed of coarser material is always less stable than that composed of finer material in relatively shallow water when h, H and λ are all the same. Because the internal friction angle ϕ of coarser material should be larger than that of finer material. Fig. 61d shows the influence of ϕ on F_1 and F_2 for scouring Type "coarse". Although the percentages of the reduction of the safety factor from F_1 to F_3 are almost the same for $\phi = 25^{\circ}$ and 30°, the value of F_3 for $\phi = 30^{\circ}$ is very close to that for $\phi = 25^{\circ}$ for scouring Type "fine".

4. From Fig. 61a and b, $F_3 = F_1$ when h/λ = 0.075 for scouring Type "fine". This means that the scouring troughs do not influence the stability of the breakwaters, even though the maximum scouring depth $Z_{sm} = H$ in these cases. It can be concluded in such a situation extending the protective layer to a distance $L = \lambda/4$, which is 33.3 and 50 m for case 1 and 4 respectively, is definitely unnecessary. Perhaps, a few meters long protective layer protecting the toe of the breakwater is enough.
In the case when the safety factor is less than needed, the length of the protective layer can be increased step by step until the required safety factor is reached.

5. In case 2 (Fig. 61c) F_2 or F_3 is less than 1.0 when h/λ = 0.075, therefore a protective layer will be very necessary. However, it can be seen in Fig. 60b that the criterion of $L = \lambda/4$ is still too long in this case.

Chapter 12. Conclusions

The scouring process of a sand bed around a structure is characterized by:

- the geometrical shape of the scouring hole;
- the ultimate scouring depth, and
- the development of the scouring as a function of time.

These aspects have been dealt with for the local scour in front of a vertical breakwater under the action of standing waves in the present study. The main conclusions can be expressed as:

1. There are two basic scouring patterns in front of a vertical breakwater. The type of the scouring pattern is dependent not only on the sand grain size but also on the wave condition. Two criteria have been found, both of which may distinguish between two types of scouring pattern. When $(u_{max}-u_{crit})/W \geq 16.5$ or $(u_{*m}-u_{*c})/W \geq 1.12$ scouring will occur at the nodes. The values of these two parameters are relatively high, which means that the majority of the material will be moved as suspended load rather than as bed load, so this is the case for relatively fine material.
2. The measured orbital velocities are close to those predicted by the first order theory of standing waves at the beginning of the tests. The near-bottom velocities decrease with time since they are influence by the developing scouring patterns.
3. The critical velocities for sand particles obtained in the tests under standing wave conditions have been compared with those calculated from different formulae based on the tests with oscillatory flow or progressive waves. On the whole, the test data of u_{crit} are lower than those predicted by the formulae. The results of the Bagnold formula are most close to but still a little higher than the test data. The reason for this discrepancy lies in the method used to determine u_{crit} in the tests.
4. The heights of the sand ripple measured in the tests have been compared with those collected by Nielson (1979) from tests with oscillatory flow or progressive waves. It seems that the former are a little higher than the latter.
5. The scouring troughs are usually broader and flatter than the deposited ridges for relatively fine material. This profile can be described by a trochoid as an approximation.

   The relative scouring depth Z_s/H increases with time or the number of waves N acting on the sea bed. The number of waves required to reach the equilibrium condition N_{max} is about 6,500 to 10,000 dependent on

the relative water depth h/λ as well as the wave steepness H/λ. Z_s/H increases very rapidly at first, reaching half of its ultimate value Z_{sm}/H in 1,000 to 2,000 waves. Z_{sm}/H is a function of h/λ, or

$$Z_{sm} = \frac{0.4\ H}{(\sin h\ 2\pi \frac{h}{\lambda})^{1.35}}$$

Bijker et al (1971, 1976) pointed out that the sand transport under standing waves for relatively fine material is caused by the mass transport current. The mechanism of sand transport has also been discussed in the present paper. When the equation of mass transport velocity presented by Longuet-Higgins (1952) as well as that of the concentration of suspended sediment derived by Hattori (1969) is substituted into the equation of continuity for local scour, a theoretical bottom profile can be obtained, which is quite similar to the measured profiles. In this way, the assumption of that the mass transport is the driving current may be proved in turn.

6. When there is a protective layer on the sand bed composed of relatively fine material in front of the breakwater, the length of which $L = \lambda/8$, $\lambda/4$ and $3\lambda/8$, the distance from the wall to the first scouring trough will increase with L, and the maximum depth of the first trough will decrease with increasing L. There is essentially no scouring over a distance $\lambda/2$ from the wall when $L = 3\lambda/8$.

7. The test started with a deformed bed reveals that the greater scouring depth once created by the storm waves, it is difficult to fill in the scouring trough by the following waves. This is probably due to the fact that the orbital velocities near the bottom are influenced by the bottom geometry.

8. The scouring profile for relatively coarse material can be described by an experimental curve when a length parameter $l_* = \frac{\lambda}{4} - l_r$ is introduced, l_r is the distance from the antinode to the nearest ripple. The development of the scouring depth for relatively coarse material is about the same as that for relatively fine material.
   It is proved by the tests that sand diameter, water depth as well as wave steepness has no obvious influence on the dimensionless scouring depth Z_{sm}/H, which can be expressed as a function of the relative water depth h/λ only.

9. The scale of the sand grain size n_D can be obtained via the similarity of the parameter $(u_{max}-u_{crit})/W$ in model and in prototype. As an approximation,

$$n_D = n_l^{0.25} \qquad \text{(for finer sand)}$$

$$n_D = n_l^{0.5} \qquad \text{(for coarser sand)}$$

n_l is the length scale.

The scale of the scouring depth n_z is derived from the equation of motion of the sand particle along the slope of a dynamic equilibrium profile for relatively fine material. With some assumptions, the following simple relationship is obtained:

$$n_z = n_l$$

The mass transport velocity along the slope of the equilibrium profile u_o can also be obtained from the equation of motion, which is much smaller than the theoretical mass transport velocity derived from a flat bottom $\bar{U}_{max}$. The reduction of the mass transport velocity, as well as the reduction of the orbital velocity (Conclusion 2) near the bottom may explain why eventually an equilibrium profile can be reached.

10. When a train of irregular waves acts on the vertical breakwater, the wave energy decreases rather fast with increasing distance l from the wall. The maximum scouring depth of every scouring trough decreases even faster with increasing l.

    The ultimate maximum scouring depth of the first trough from the wall is compared with that obtained from the regular wave test. Some of the irregular wave test runs show that the equivalent wave length λ can be obtained from the mean wave period $\bar{T}$, and the equivalent wave height is roughly between the mean wave height $\bar{H}$ and the significant wave height H_s. For the time being, H_s is recommended as the equivalent wave height.

11. The dimensionless scouring depths measured from the tests as well as the recommended scouring profiles for both types of material have been applied to some typical prototype conditions to examine the influence of the scouring patterns on the stability of the foundations of the breakwaters. In some unfavourable conditions, the safety factor of stability reduces as much as 20%, which is demonstrated by the slip circle method. However, in some other cases, the influence of the scouring holes can almost be neglected, so that a relatively long protective layer of $L = \lambda/4$ to $3\lambda/8$ is quite unnecessary.

References

1. Bagnold, R.A. (1946): Motion of waves in shallow water: Interaction between waves and sand bottom, Proc. Royal Society of London, Series A, Vol. 187.

2. de Best, A., Bijker, E.W., and Wichers, J.E.W. (1971): Scouring of a sand bed in front of a vertical breakwater, Proc. 1st Conf. on Port and Ocean Engi. under Arctic Conditions, Vol. 2.

3. Bijker, E.W., van Hijum, E., and Vellinga, P. (1976): Sand transport by waves, Proc. 15th Coastal Engi. Conf. Vol. 2.

4. Breusers, H.N.C., Nicollet, G., and Shen, H.N. (1977): Local scour around cylindrical piers, in H.N.C. Breusers (editor): "Local Scour", IHE, Delft, The Netherlands.

5. Davies, A.G., and Wilkinson, R.H. (1978): Sediment motion caused by surface water waves, Proc. 16th Coastal Engi. Conf., Vol. 2.

6. Eagleson, P.S., and Dean, R.G. (1959), Wave-induced motion of bottom sediment particles, Journal of the Hydraulics Division, Proc. ASCE, Vol. 85, No. HY10.

7. Hallermeier, R.J. (1980): Sand motion initiation by water waves: Two asymptotes, Journal of the Waterway, Port, Coastal and Ocean Division, Proc. ASCE, Vol. 106, No. WW3.

8. Hattori, M. (1969): The mechanics of suspended sediment due to standing waves, Coastal Engi. in Japan, Vol. 12.

9. Hattori, M. (1971): A further investigation of the distribution of suspended sediment concentration due to standing waves, Coastal Engi. in Japan, Vol. 14.

10. Herbich, J.B., and Ko, S.C. (1968): Scour of sand beaches in front of seawalls, Proc. 11th Coastal Engi. Conf., Vol. 1.

11. van Hijum, E. (1976): Equilibrium profiles and longshore transport of coarse material under oblique wave attack, Proc. 15th Coastal Engi. Conf., Vol. 2.

12. Hotta, S., and Marui, N. (1976): Local scour and current around a porous breakwater, Proc. 15th Coastal Engi. Conf., Vol. 2.

13. Jonsson, I.G. (1966): Wave boundary layers and friction factors, Proc. 10th Coastal Engi. Conf..

14. Komar, P.D., and Miller, M.C. (1974): Sediment threshold under oscillatory waves, Proc. 14th Coastal Engi. Conf., Vol. 2.

15. Lates, M. (1963): On the distribution curves of wave height in the coast zone, (in French, with English synopsis) Proc. 10th Congress of IAHR, Vol. 1.

16. Le Méhauté, B., Divoky, D., and Lin, A. (1968): Shallow water waves. A comparison of theories and experiments, Proc. 11th Coastal Engi. Conf., Vol. 1.

17. Longuet-Higgins, M.S. (1952): Mass transport in water waves, Phil. Trans. Royal Society of London, Series A, Vol. 245, No. 903.

18. Madson, O.S., and Grant, W.D. (1976): Sediment transport in the coastal environment, Report No. 209, Department of Civil Engi. MIT, Cambridge, Mass..

19. Nielson, P. (1979): Some basic concepts of wave sediment transport, Series Paper 20. Insti. Hydrodynamics and Hydraulic Engi., Tech. U. of Denmark.

20. Noda, H. (1968): A study on mass transport in boundary layers in sranding waves, Proc. 11th Coastal Engi. Conf., Vol. 1.

21. Ochi, M.K. (1979): A series of JONSWAP wave spectra for offshore structure design. Proc. 2nd International Conf. on Behaviour of Off-Shore Structures, Vol. 1.

22. Sato, S., Tanaka, N., and Irie, I. (1968): Study on scouring at the foot of coastal structures, Proc. 11th Coastal Engi. Conf., Vol. 1.

23. Silvester, R., and Mogridge, G.R. (1970): Reach of waves to the bed of the continental shelf, Proc. 12th Coastal Engi. Conf., Vol. 2.

24. Swart, D.H. (1977): Weighted value of depth of initiation of movement, Stellenbosch.

25. Wells, D.R., and Sorensen, R.M. (1970): Scour around a circular cylinder due to wave motion, Proc. 12th Coastal Engi. Conf., Vol. 2.

Appendix 1. Main Symbols

a_b	amplitude of orbital motion at the bottom
B	width of the breakwater
C_D	coefficient of drag of the sand particle
C_x	concentration of suspended sediment at x
C_o	concentration of suspended sediment at the node
D_{50}	sand particle diameter (50% by weight exceeded in size)
f	frequency of the wave component
f_d	net drag force
f_m	peak frequency of wave spectrum
f_w	wave friction factor
F	safety factor, or fetch length
F_d	drag force
F_f	friction force
F_g	component of the gravitational force
g	accelaration of gravity
h	water depth
h*	a dimensionless parameter equal to $\bar{H}/h$
H	wave height
H_p	a wave height, the probability of exceedance of which is P_H
H_r	sand ripple height
H_s	significant wave height
$\bar{H}$	mean wave height
K	wave number
$K_u^2(f)$	transfer function of the velocity spectrum
l	distance measured from the wall
l_r	a distance measured from the antinode to the nearest ripple
l*	a length parameter equal to $\frac{\lambda}{4} - l_r$
L	length of the protective layer
n	scale
N	number of waves
N_{max}	number of waves when the equilibrium condition is reached
P	wave force on breakwater
P_H	probability of exceedance of wave height
P_u	probability of exceedance of orbital velocity
r	bed roughness
r_p	arm of the wave force to the center of the slip circle
R	radius of the slip circle, or a parameter for describing the trochoid

Re	Reynolds Number
S	sand transport rate
S(f)	wave spectrum
S(u)	velocity spectrum
t	time
t_{max}	time of wave action when the equilibrium condition is reached
T	wave period
T_m	peak period of wave spectrum
$\bar{T}$	mean wave period
u	horizontal compoenent of the orbital velocity of the standing waves
u_b	maximum orbital velocity at the bottom
u_p	horizontal orbital velocity, the probability of exceedance of which is P_u
u_s	significant value of the horizontal orbital velocity, or velocity of a sand particle along the slope of an equilibrium profile
$\bar{u}$	mean value of the horizontal orbital velocity
u_o	net water velocity along the slope of an equilibrium profile
u_α	water velocity along the slope of an equilibrium profile
$u_{crit.}$	critical velocity for sand particle
u_{max}	maximum orbital velocity at the bottom at the node
u_+	orbital velocity in the same direction with the propagation of the waves
u_-	orbital velocity in the opposite direction with the propagation of the waves
u_*	shear velocity
U	wind speed
$\bar{U}$	mass transport velocity at the bottom
$\bar{U}_{max}$	maximum mass transport velocity at the bottom
U(x)	driving velocity of suspended sediment
w	fall velocity of the sand particle
W_i	weight of the ith slice
W_s	weight of the sand particle in water
x	horizontal coordinate measured from the node, positive towards the wall
x_t	horizontal coordinate of the trochoid
X	horizontal coordinate of an experimental curve
z	vertical coordinate measured from the sill water level, positive upward
z_b	vertical coordinate measured from the bottom, positive upward

z_c	height of a high concentration layer above the bottom
z_t	vertical coordinate of the trochoid, measured from a height z_o above the bottom, positive upward
Z	scouring depth, positive downward
Z_s	maximum scouring depth of the trough at time t
Z_{sm}	ultimate maximum scouring depth of the trough
Z'_{sm}	ultimate maximum scouring depth of the first trough from the wall when there is a protective layer on the sand bed
α	angle of the slope of an equilibrium profile measured at the place where Z = 0
α_i	angle between the gravitational force and the normal force on the arc of the slip circle
Δ	relative mass density of sand
θ	a parameter for describing the trochoid
λ	wave length
λ_r	sand ripple length
ν	kinematic viscosity of water
ρ	mass density of water
ρ_s	mass density of sand
τ	bottom shear stress
ϕ	natural repose angle, or internal friction angle of sand
ψ	Shields Parameter
ω	angular frequency

Appendix 2. Derivations of Eqs. 39 and 40

1. For Re < 100, from eqs. 33, 36 and 37

$$F_d = \frac{\pi}{8} \rho C_1 \nu D_{50} (u_o + u_1 \cos \theta) \tag{A.1}$$

in which $\theta = \omega t$.

$$f_d = \frac{1}{2\pi} \int_0^{2\pi} F_d \, d\theta$$

$$= \frac{\pi}{8} \rho C_1 \nu D_{50} u_o \tag{A.2}$$

Substituting $C_D = \frac{C_1 \nu}{u_o D_{50}}$ into eq. A.2, then

$$f_d = \rho C_D \frac{\pi D_{50}^2}{8} u_o^2 \tag{39}$$

2. For Re > 1,000, from eqs. 33, 36 and 38

$$F_d = \frac{1}{2} \rho C_2 \frac{\pi D^2}{4} (u_o + u_1 \cos \theta) \left| u_o + u_1 \cos \theta \right| \tag{A.3}$$

$$f_d = \frac{1}{2\pi} C_3 \int_0^{2\pi} (u_o + u_1 \cos \theta) \left| u_o + u_1 \cos \theta \right| d\theta \tag{A.4}$$

in which $C_3 = \frac{1}{2} \rho C_2 \frac{\pi D^2}{4}$. When $0 \lesssim \frac{u_o}{u_1} < 1$, then

$$f_d = \frac{C_3}{2\pi} \left\{ \int_{-(\frac{\pi}{2} + \Delta\theta)}^{\frac{\pi}{2} + \Delta\theta} (u_0^2 + 2 u_o u_1 \cos \theta + u_1^2 \cos^2 \theta) \, d\theta \right.$$

$$\left. + \int_{\frac{\pi}{2} + \Delta\theta}^{\frac{3}{2}\pi - \Delta\theta} [-(u_o^2 + 2 u_o u_1 \cos \theta + u_1^2 \cos^2 \theta)] \, d\theta \right\} \tag{A.5}$$

in which $\Delta\theta$ depends on the value of u_o/u_1. When u_o/u_1 is small, then $\Delta\theta$ can be neglected (Fig. A1). Therefore

$$f_d = \frac{C_3}{2\pi} \left\{ \int_{-\frac{\pi}{2}}^{\frac{\pi}{2}} u_o^2 \, d\theta + \int_{-\frac{\pi}{2}}^{\frac{\pi}{2}} 2 u_o u_1 \cos \theta \, d\theta + \int_{-\frac{\pi}{2}}^{\frac{\pi}{2}} u_1^2 \cos^2 \theta \, d\theta \right.$$

$$\left. - \int_{\frac{\pi}{2}}^{\frac{3\pi}{2}} u_o^2 \, d\theta - \int_{\frac{\pi}{2}}^{\frac{3\pi}{2}} 2 u_o u_1 \cos \theta \, d\theta - \int_{\frac{\pi}{2}}^{\frac{3\pi}{2}} u_1^2 \cos^2 \theta \, d\theta \right\}$$

$$= \frac{C_3}{2\pi} \left\{ u_o^2 \pi + 4 u_o u_1 + u_1^2 \frac{\pi}{2} - u_o^2 \pi + 4 u_o u_1 - u_1^2 \frac{\pi}{2} \right\}$$

$$= \frac{C_3}{\pi} 4 u_o u_1 = \frac{1}{2} \rho C_D D_{50}^2 u_o u_1 \qquad (40)$$

Appendix 3. Computer Program for the Stability Analysis of the Breakwater Influenced by the Scouring of the Sea Bed

```
FTN4
      PROGRAM XIE10
      DIMENSION IPRAM(5),X(300),YA(300),YB(300),W(300)
      DIMENSION IDCB(144),NAME(3),IBUF(50)
C
      CALL RMPAR(IPRAM)
      INP=IPRAM(1)
      IF(INP.EQ.0) INP=1
      LIST=IPRAM(2)
      IF(LIST.EQ.0) LIST=INP
C
      WRITE(INP,10)
   10 FORMAT(5X," NN ?")
      READ(INP,*) NN
      WRITE(INP,20)
   20 FORMAT(5X," ANGLE OF INTERNAL FRICTION : PH ?")
      READ(INP,*) PH
      WRITE(INP,30)
   30 FORMAT(5X," UNIT WEIGHT OF SOIL : G ?")
      READ (INP,*) G
      WRITE(INP,40)
   40 FORMAT(5X," WAVE FORCE : F ?")
      READ (INP,*) F
      WRITE(INP,70)
   70 FORMAT(5X," HEIGHT OF WAVE FORCE : YF ?")
      READ (INP,*) YF
      WRITE(INP,100)
  100 FORMAT(5X," X---COORDINATE OF BREAKWATER : XL ?")
      READ (INP,*) XL
      WRITE(INP,120)
  120 FORMAT(5X," GIVE THE FILE NAME")
      READ (INP,130) (NAME(I),I=1,3)
  130 FORMAT(3A2)
      CALL OPEN(IDCB,IERR,NAME)
      IF(IERR.LE.0) STOP
      DO 140 L=1,NN
      JJ=10*(L-1)
      CALL READF(IDCB,IERR,IBUF,35,LEN)
      CALL CODE
      READ(IBUF,135) (YB(JJ+I),I=1,10)
  135 FORMAT(10F7.0)
  140 CONTINUE
C
      CALL CLOSE(IDCB,IERR)
C
      WRITE(LIST,152) PH,G,F,YF,XL
  152 FORMAT("1",/," BREAKWATER STABILITY ",//,
     1     10X,"PH=",F8.3,5X,"G=",F8.3,5X,"F=",F8.3,5X,"YF=",F8.3,5
     2          "XL=",F8.3)
      LL=10*NN
      WRITE(LIST,155) (YB(I),I=1,LL)
```

```
 155 FORMAT(10X,"YB(I)",10F10.3)
     PH=PH*3.14159/180.
     TP=TAN(PH)
 200 WRITE(INP,220)
 220 FORMAT(5X," CENTER OF CIRCLE (X,Y) : XC,YC ?")
     READ (INP,*) XC,YC
     R=XC-XL
     N=INT(2*R)
     R=SQRT(R*R+YC*YC)
     X(1)=XL+0.5
     DO 300 I=2,N
300  X(I)=X(I-1)+1
     DO 400 I=1,N
     A=X(I)-XC
400  YA(I)=YC-SQRT(R*R-A*A)
     DO 450 I=1,N
450  W(I)=G*(YB(I)-YA(I))
     P=0
     Q=0
     DO 500 I=1,N
     A=X(I)-XC
     B=YC-YA(I)
     C=SQRT(A*A+B*B)
     SI=A/C
     CO=B/C
     P=P+W(I)*CO*TP
     Q=Q-W(I)*SI
500  CONTINUE
     S=P/(Q+F*(YC-YF)/R)
     S=0.001*INT(1000*S+0.5)
     WRITE(INP,700) XC,YC,S
     WRITE(LIST,700) XC,YC,S
700  FORMAT(5X,/,5X,"XC=",F8.3,5X,"YC=",F8.3,5X,"S=",F8.3,/)
     WRITE(INP,750)
750  FORMAT(3X," DO YOU WANT TO CONTINUE ? Y/NO")
     READ (INP,760) MMM
760  FORMAT(A2)
     IF(MMM.NE.2HNO)GO TO 200
     WRITE(LIST,850)
850  FORMAT(1H1)
     STOP
     END
     END$
```

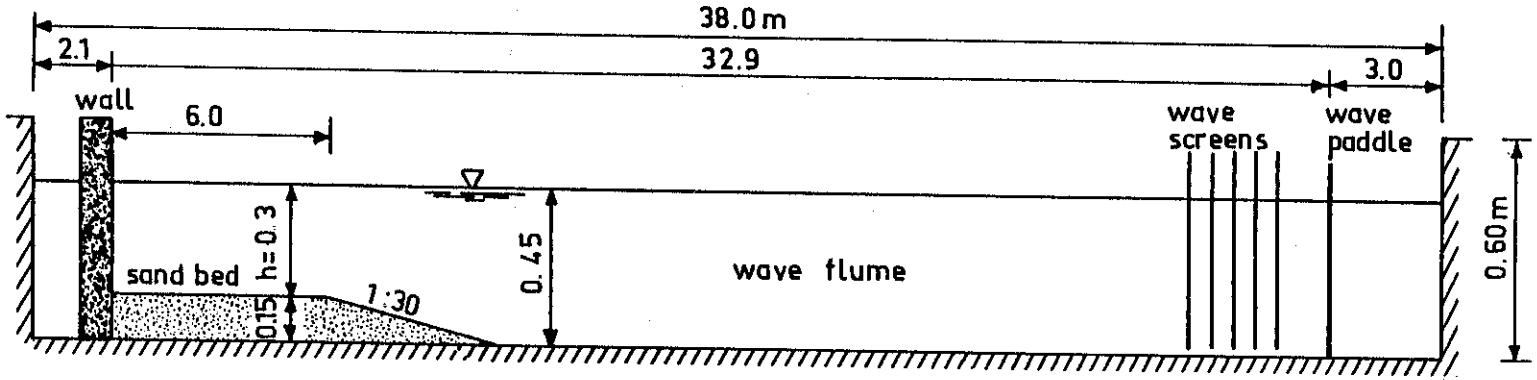

Fig.1 Experimental arrangement in the small flume

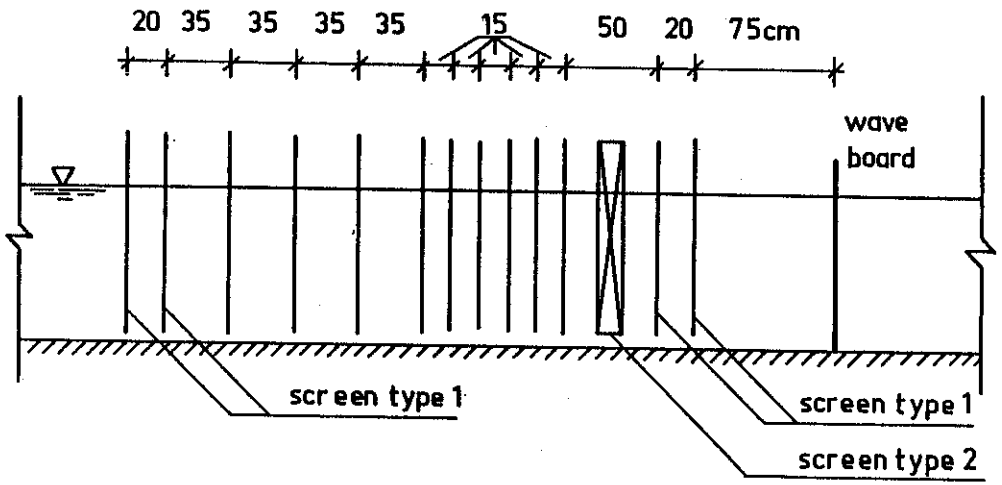

Fig.2 Wave screen system

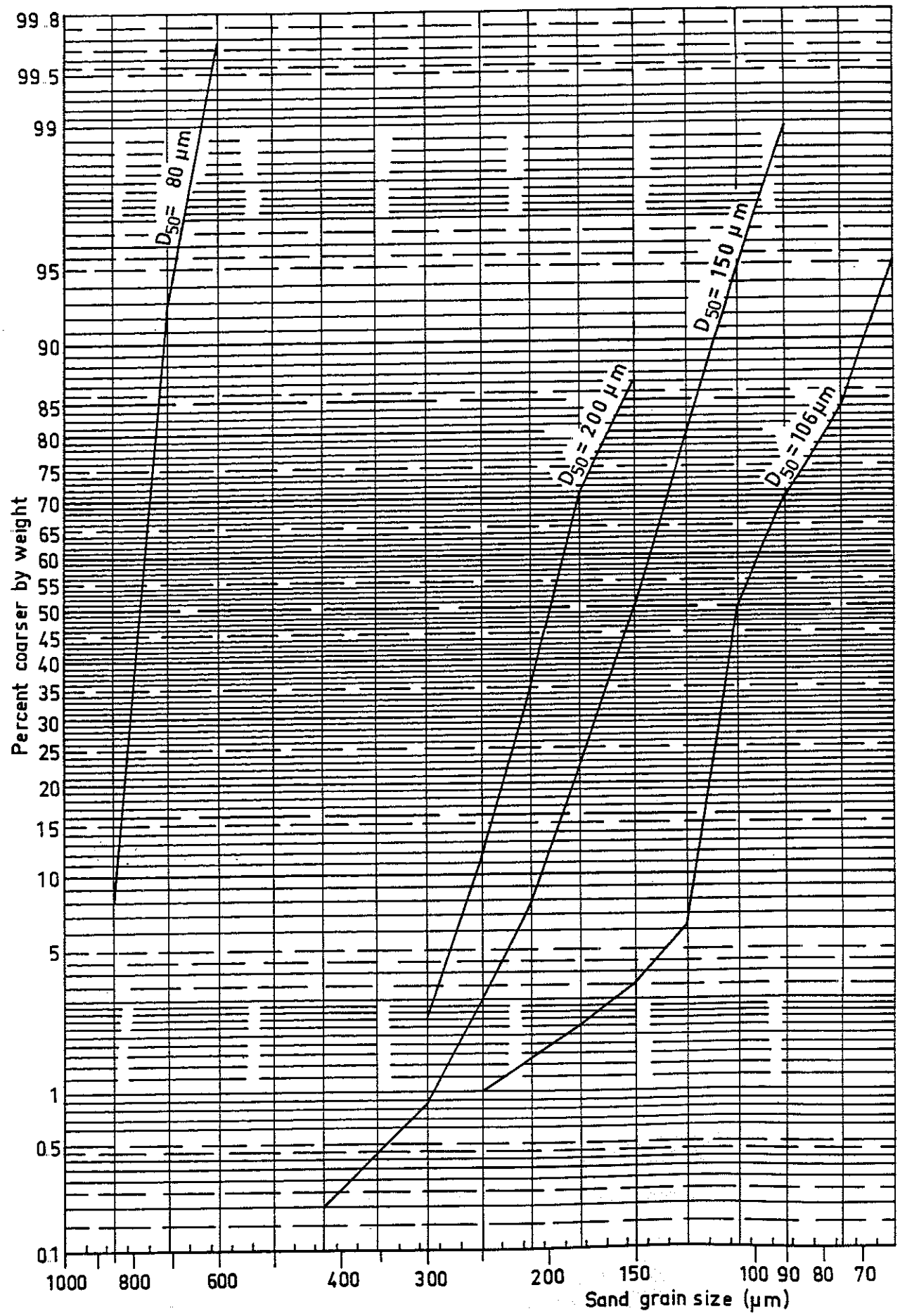

Fig.5 Sand grain size distribution curves

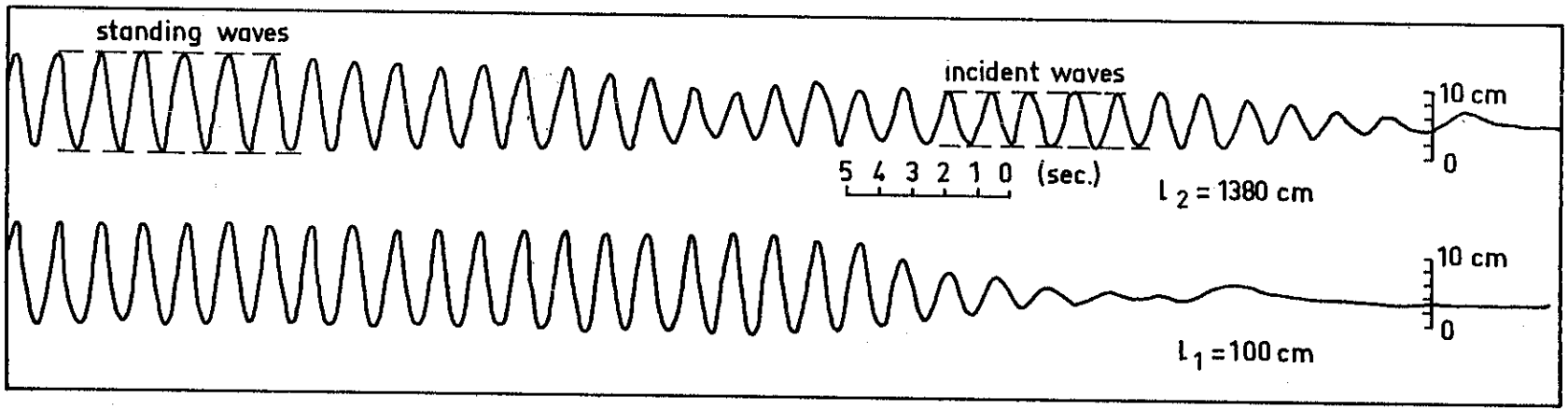

Fig. 6 Wave profiles of test No.2a
(H = 7.5^{cm}, T = 1.32^{s}, at the beginning of the test)

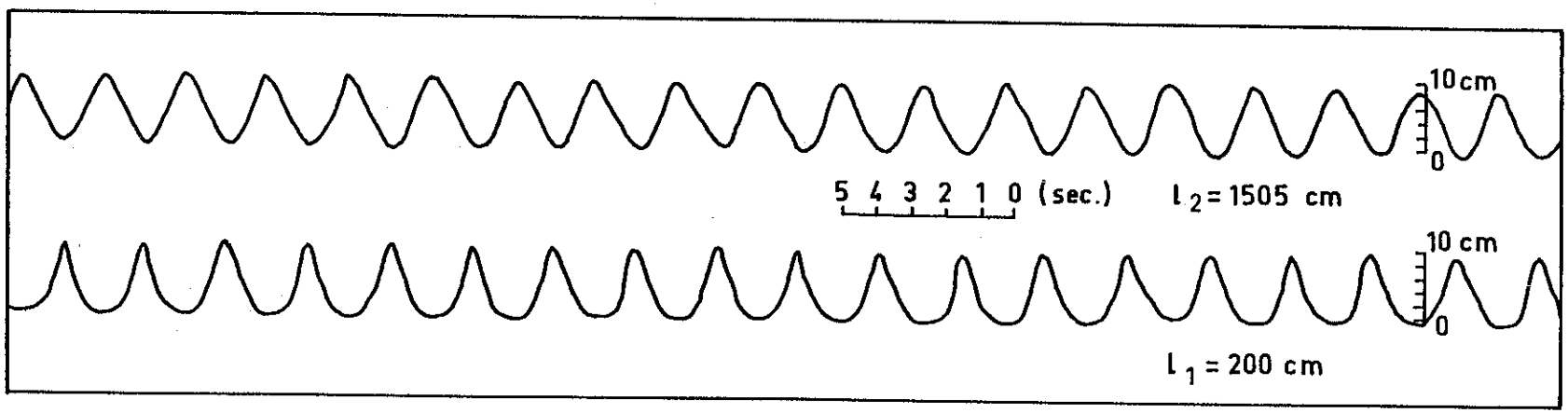

Fig. 7 Wave profiles of test No.25a
(H = 5.0^{cm}, T = 2.41^{s}, at the end of the 4th hour)

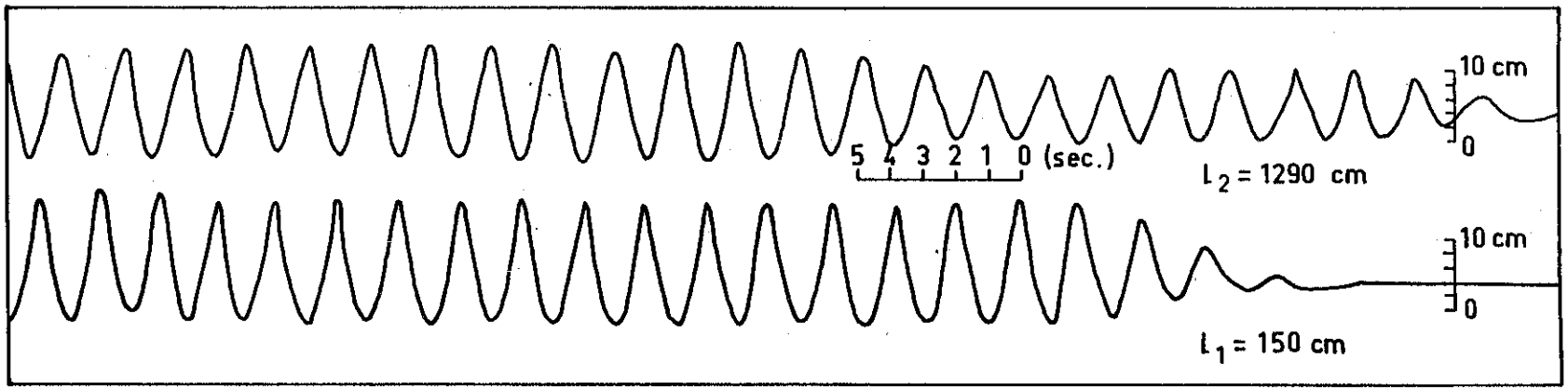

a, at the beginning of the first hour

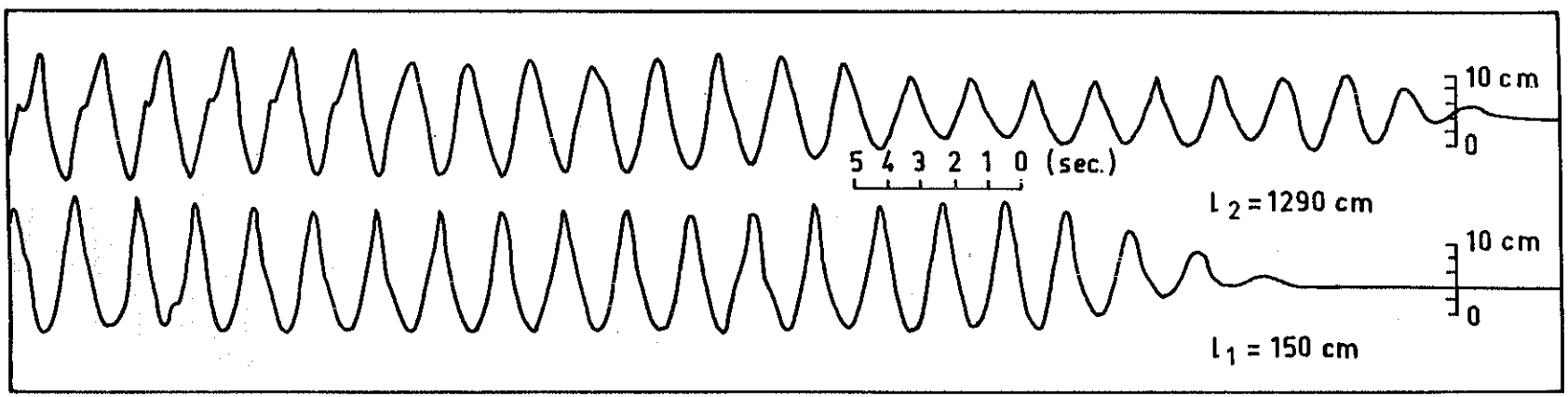

b, at the beginning of the third hour

Fig. 8 Wave profiles of test No.6a

($H = 9.0^{cm}$, $T = 1.86^{s}$)

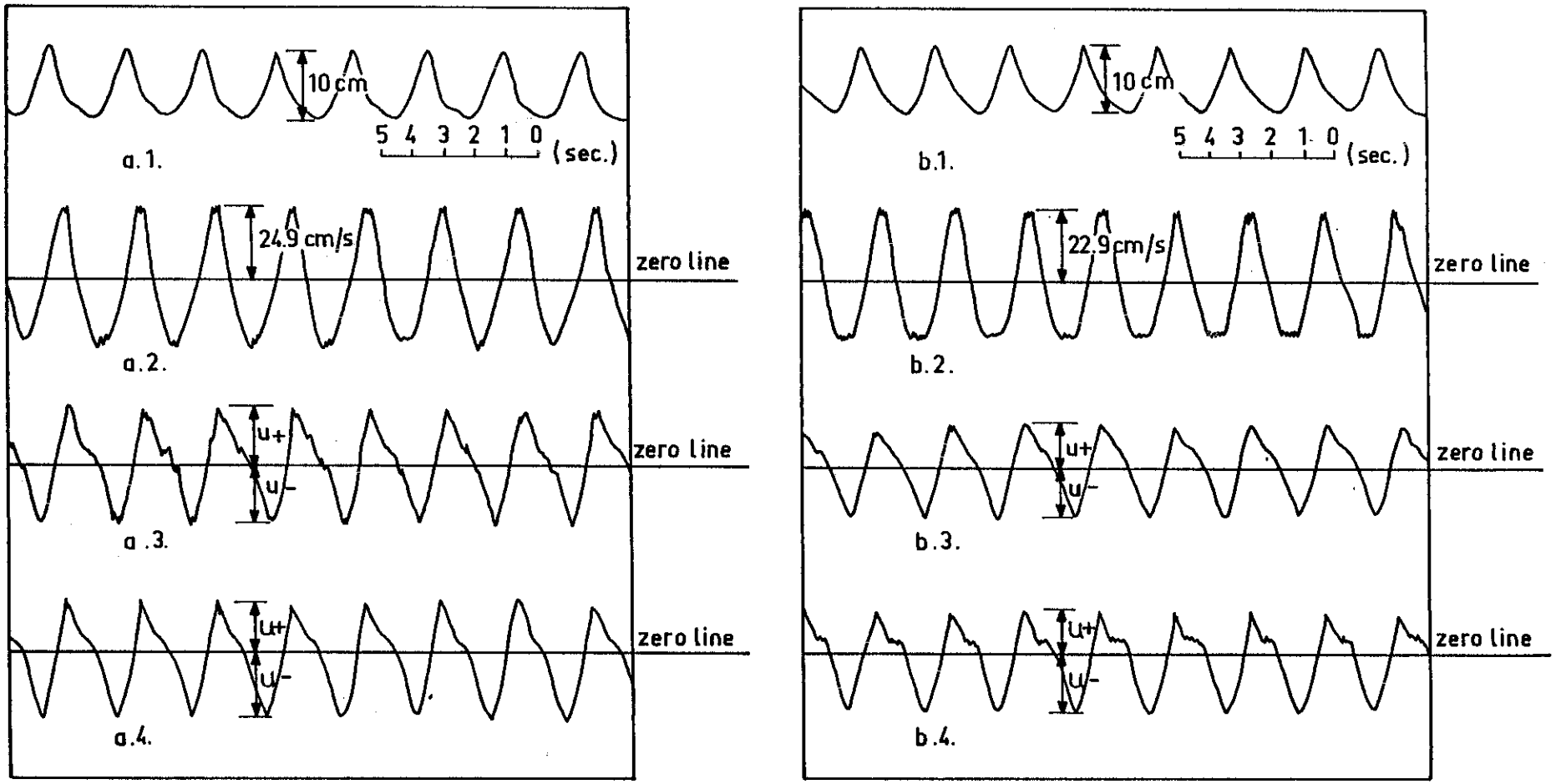

Fig. 9 Wave and orbital velocity profiles of test No.25a

($H = 5.0^{cm}$, $T = 2.41^{s}$)

a. measured at the beginning of the test,
b. measured at the end of the test.

1. Wave profile.

2. Velocity at $x = 0$, $Z_b = 5$ cm, 3. Velocity at $x = \frac{\lambda}{8}$, $Z_b = 3$ cm,

4. Velocity at $x = \frac{\lambda}{8}$, $Z_b = 20$ cm

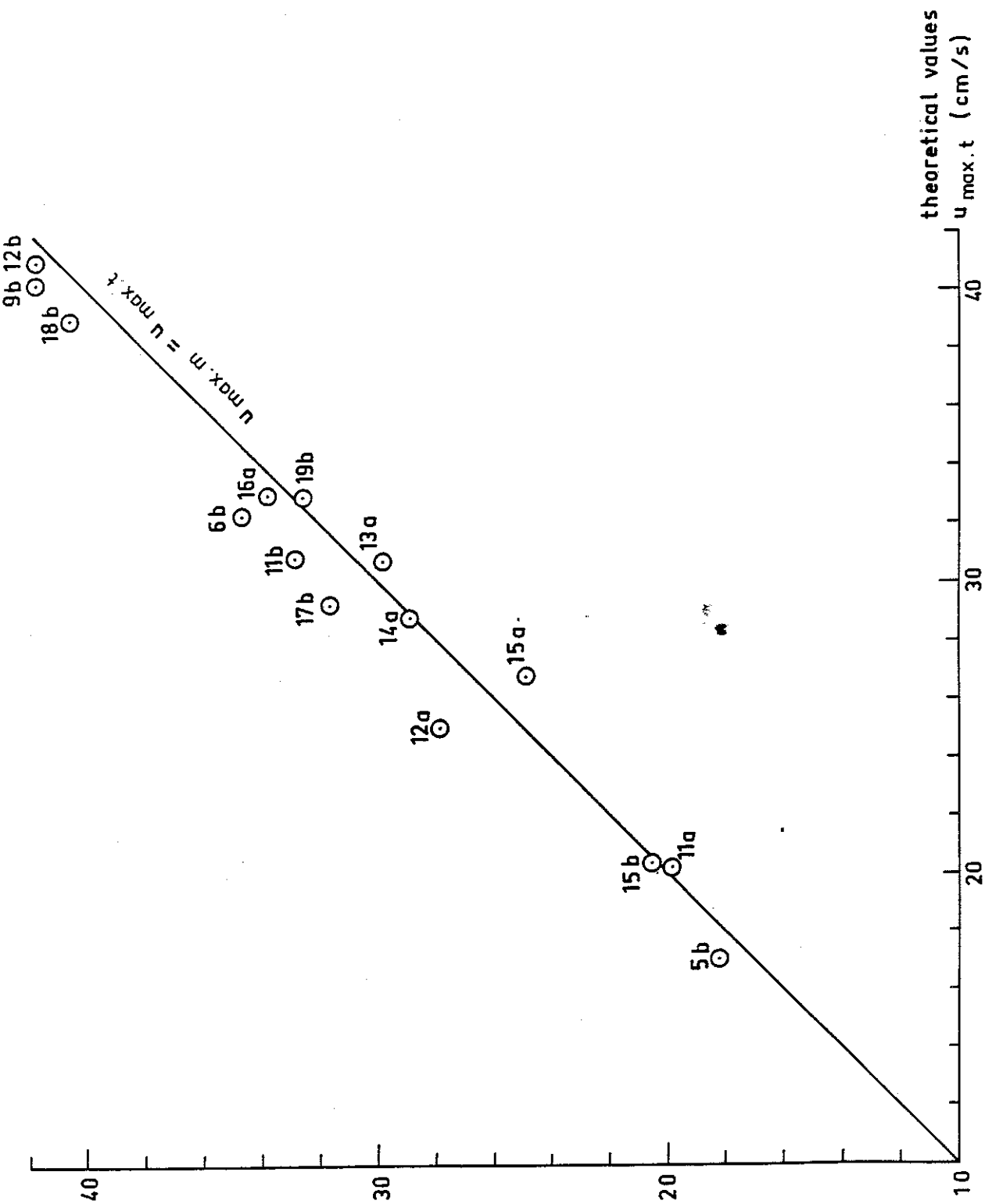

Fig. 10 Comparison of bottom orbital velocities at nodes (x = 0)

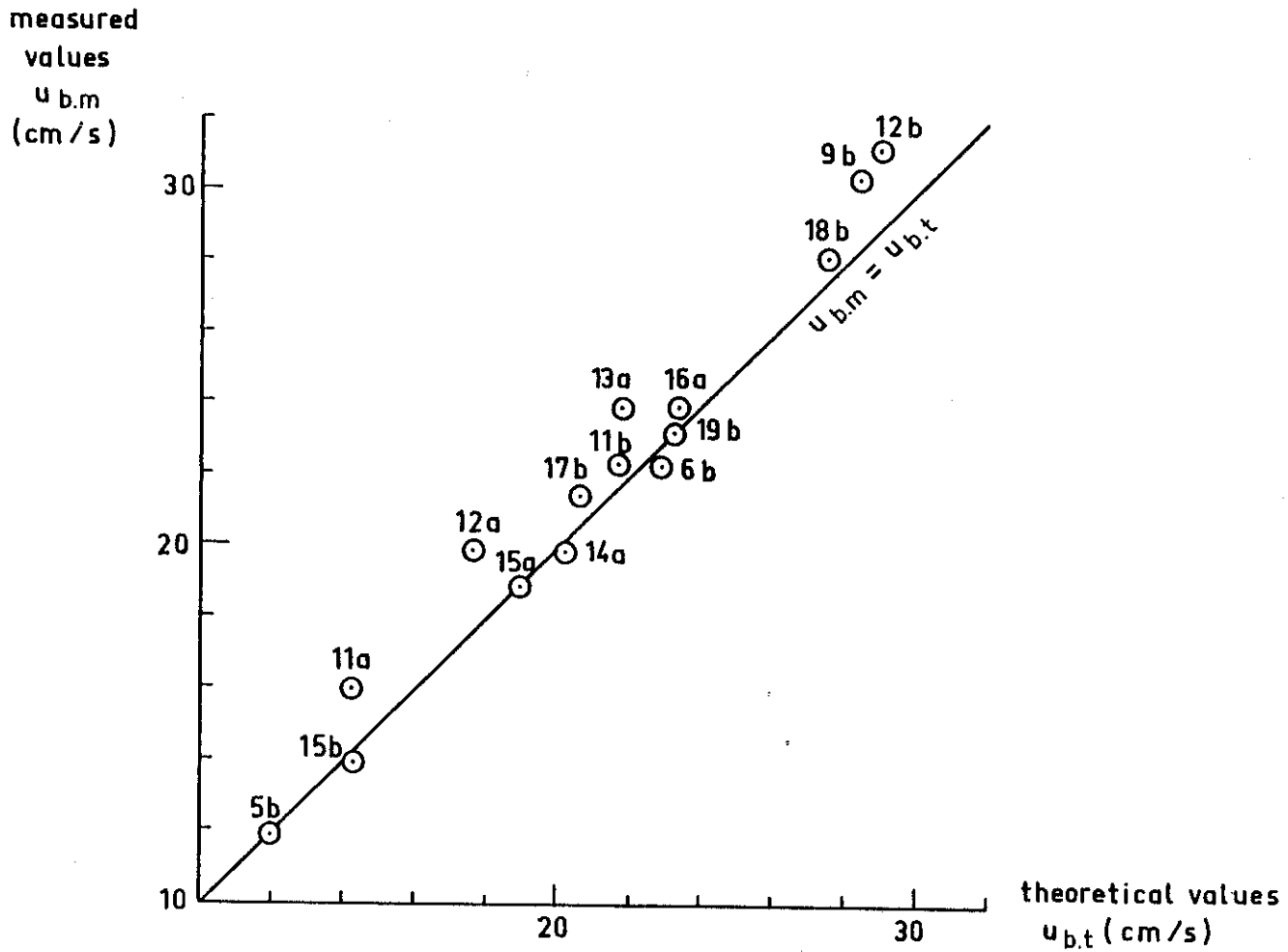

Fig. 11 Comparison of bottom orbital velocities at x = $\lambda/8$

($u_{b.t}$ is from the first order theory)

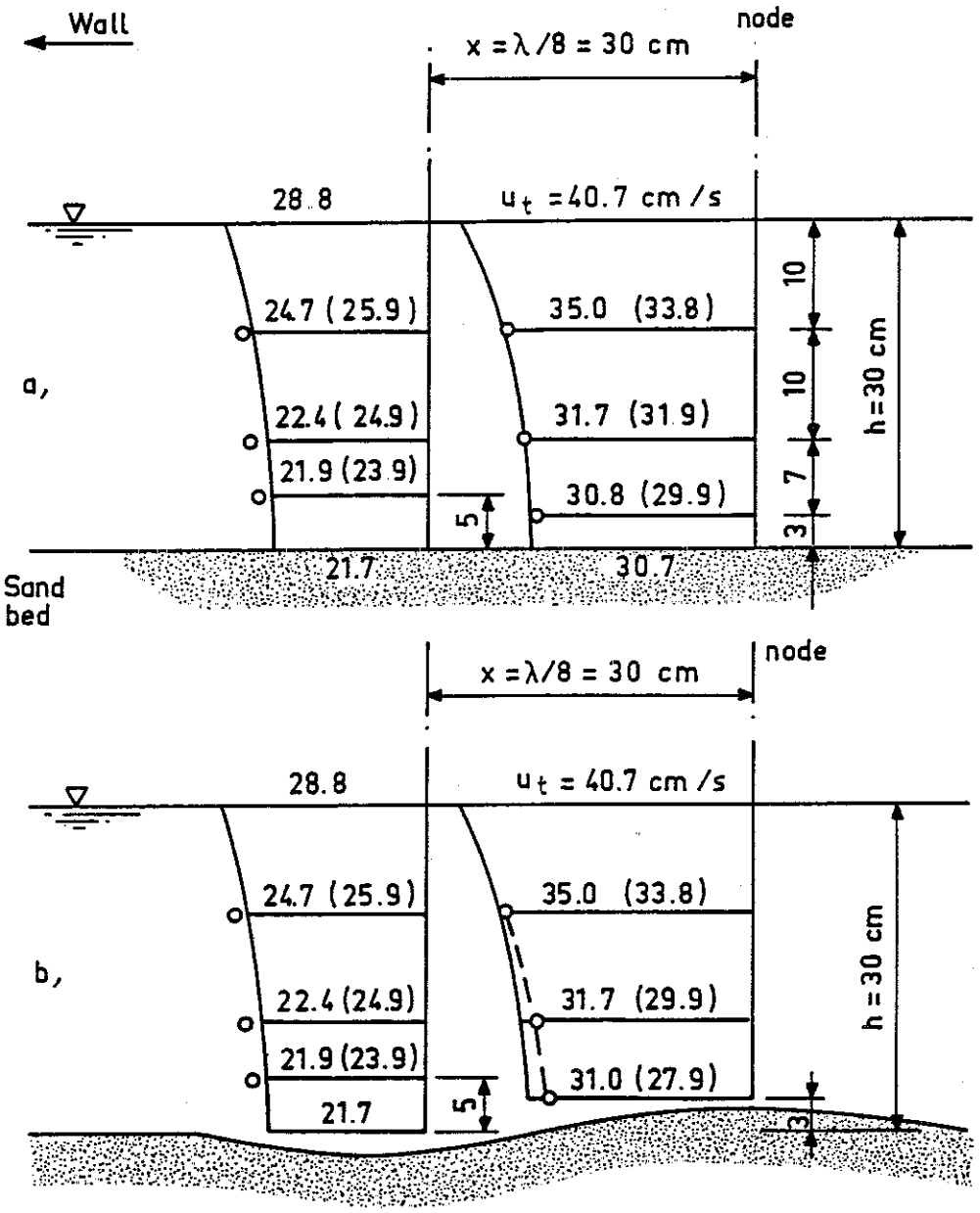

Fig. 12 Orbital velocity field patterns of test No.13a
($H = 6.5^{cm}$, $T = 1.53^{s}$)

a, at the beginning of the first hour

b, at the end of the fourth hour

u_t ———— theoretical horizontal velocity component; the small open circle represents the measured velocity component, its value is shown in the brackets.

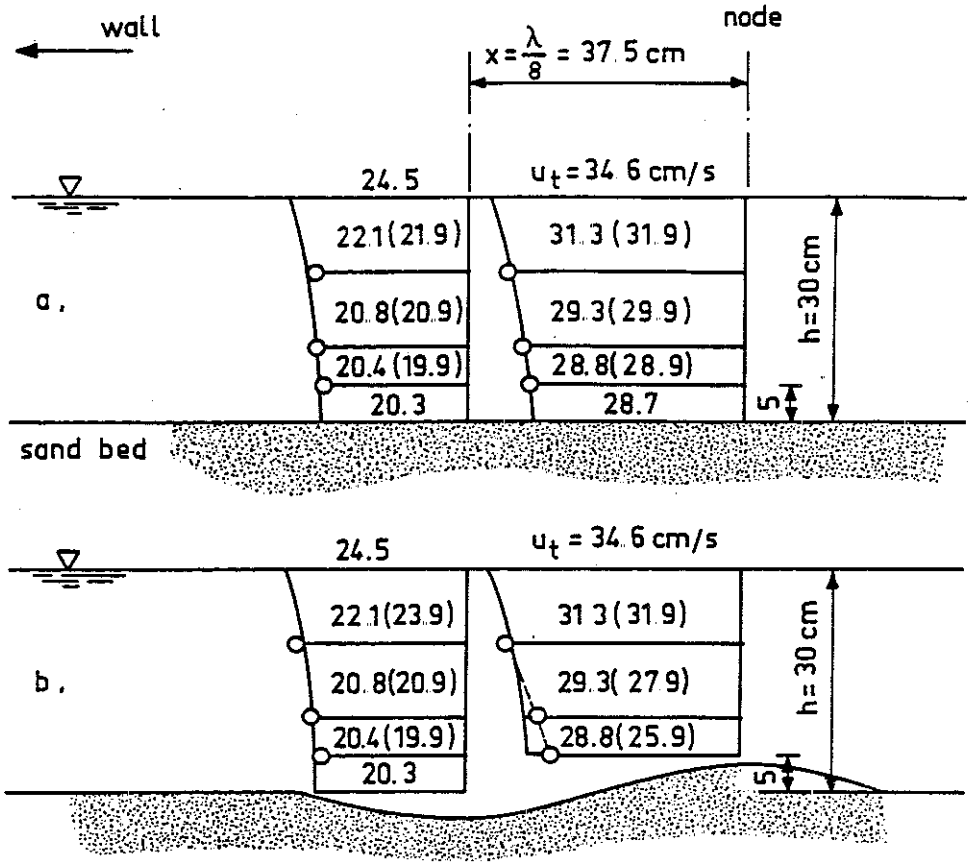

Fig. 13 Orbital velocity field patterns of test No.14a
(H = 5.7 cm, T = 1.86 s)

a, at the beginning of the first hour
b, at the end of the fourth hour

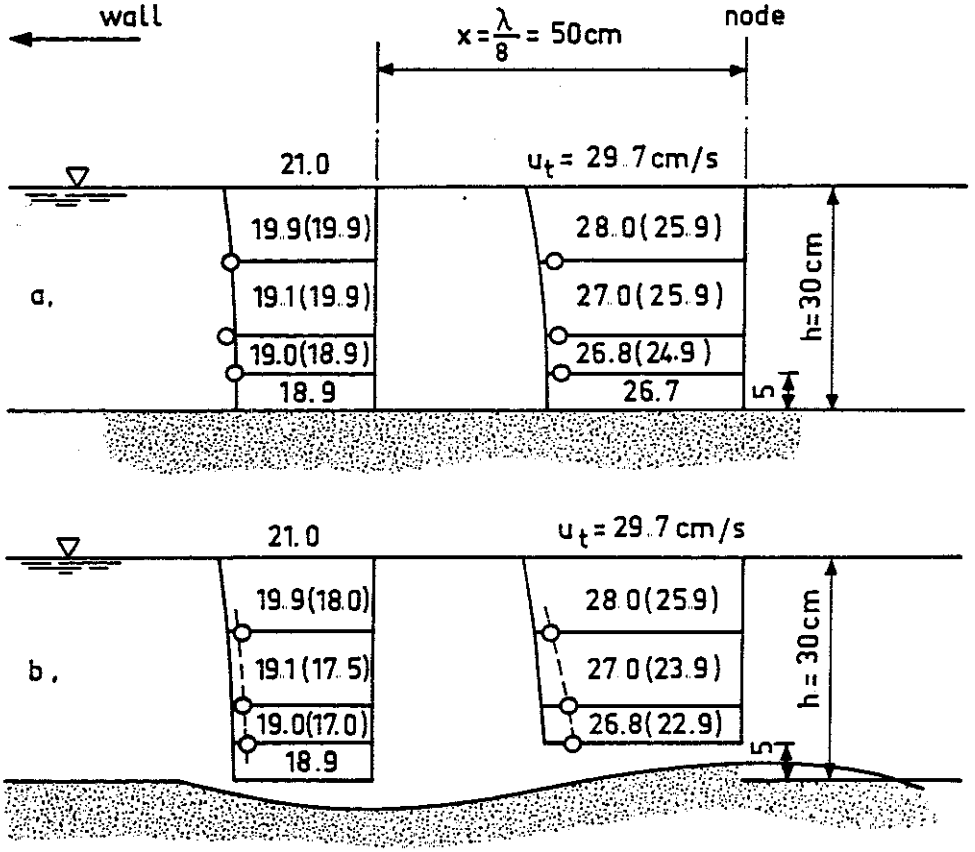

Fig. 14 Orbital velocity field patterns of test No.15a
(H = 5.0 cm, T = 2.41 s)

a, at the beginning of the first hour,
b. at the end of the fourth hour

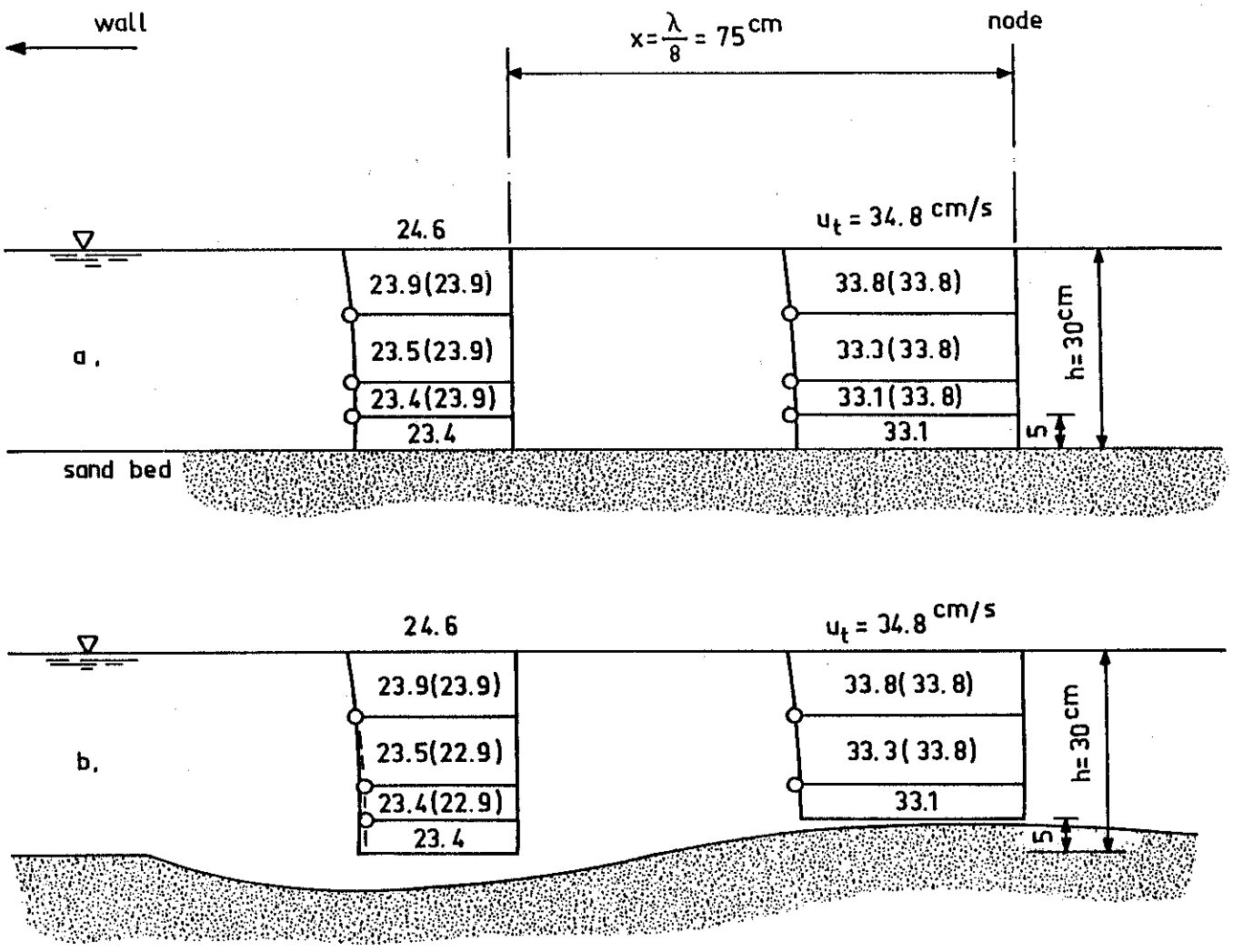

Fig. 15 Orbital velocity field patterns of test No.16a
(H = 6.0 cm, T = 3.56 s)

a, at the beginning of the first hour
b, at the end of the fifth hour

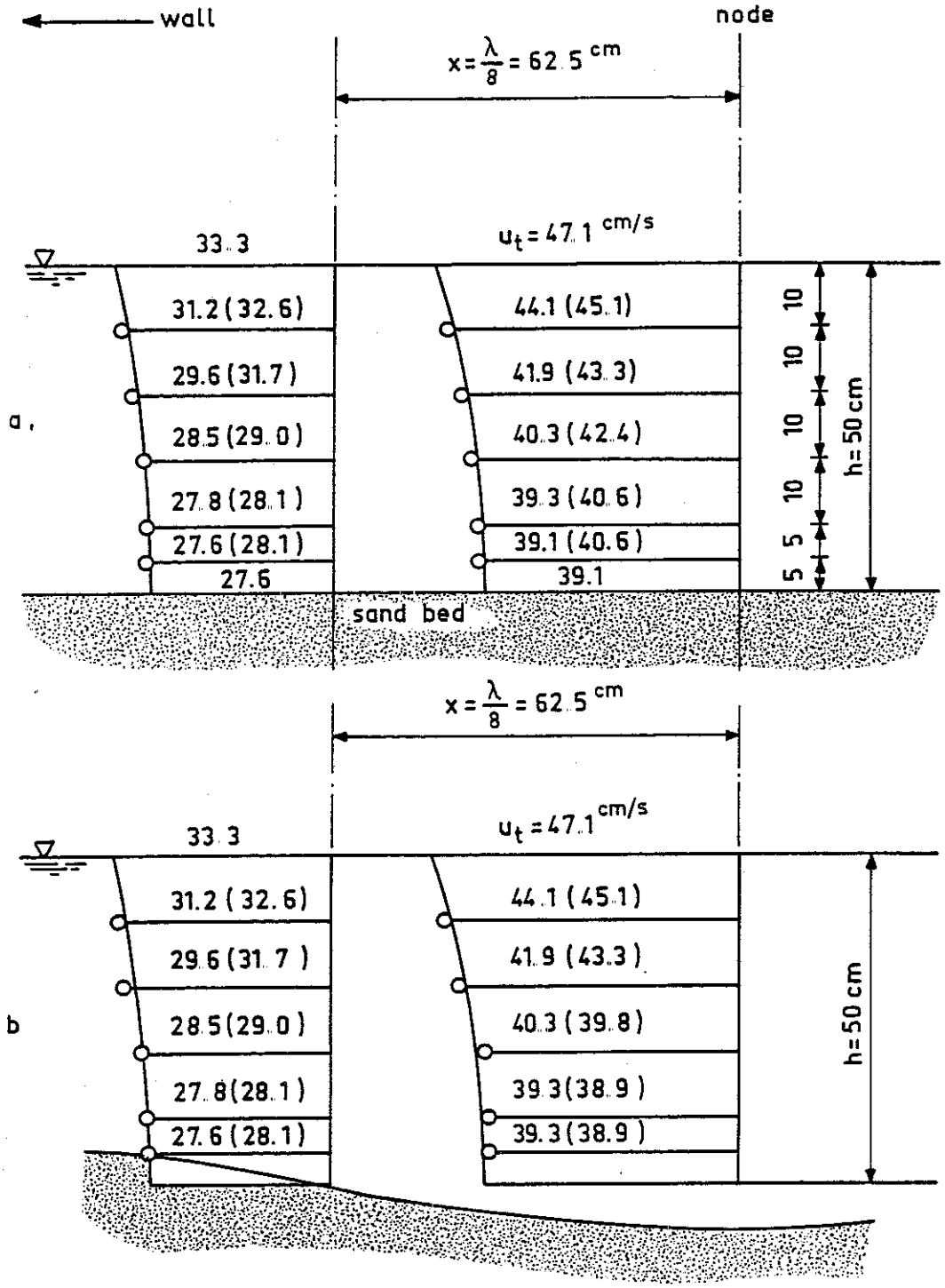

Fig. 16 Orbital velocity field patterns of test No.18b
(H = 10.0 cm, T = 2.40 s)

a, at the beginning of the first hour
b, at the end of the sixth hour

b, at the end of the fifth hour

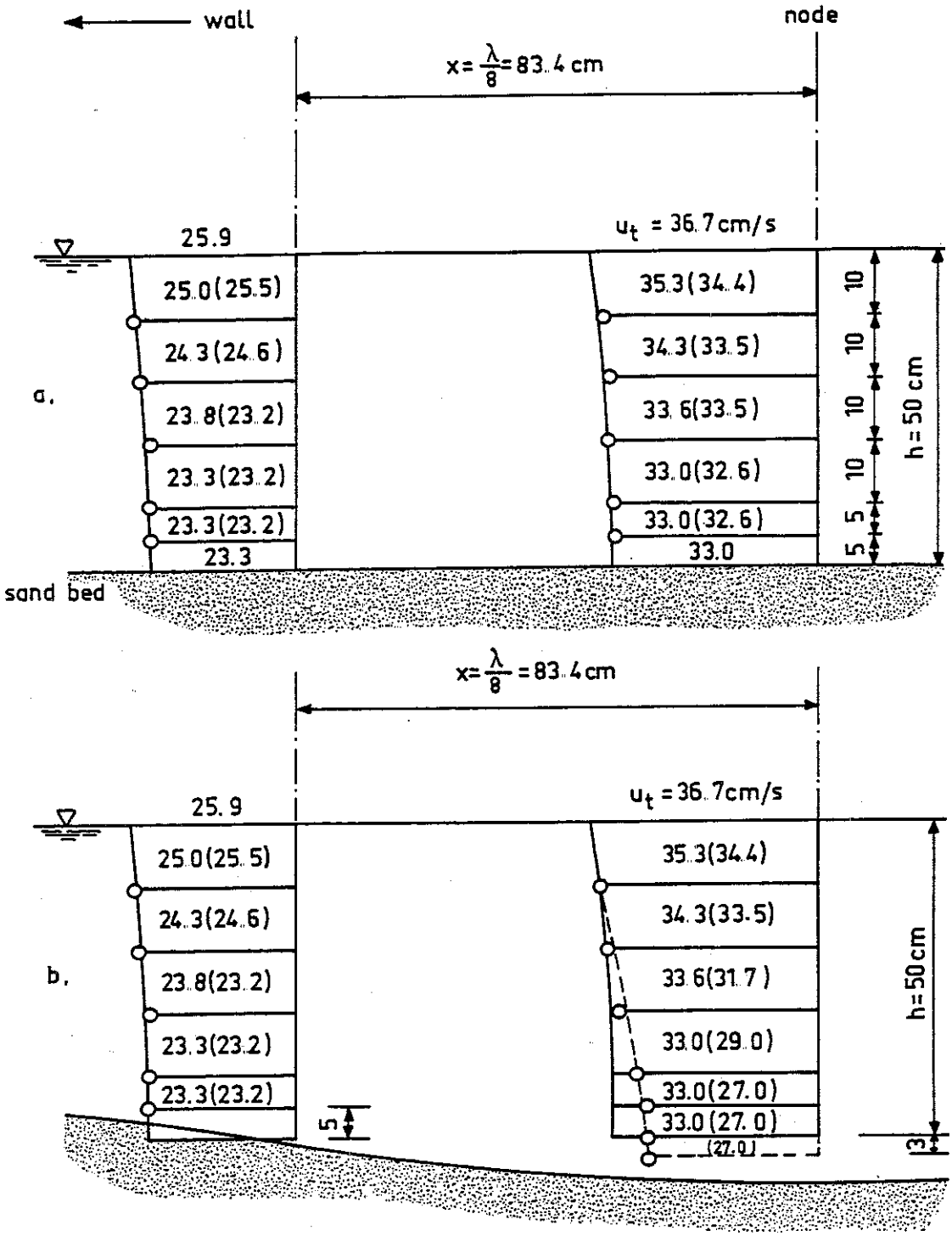

Fig. 17 Orbital velocity field patterns of test No.19b
(H = 8.0 cm, T = 3.12 s)

a, at the beginning of the first hour
b, at the end of the seventh hour

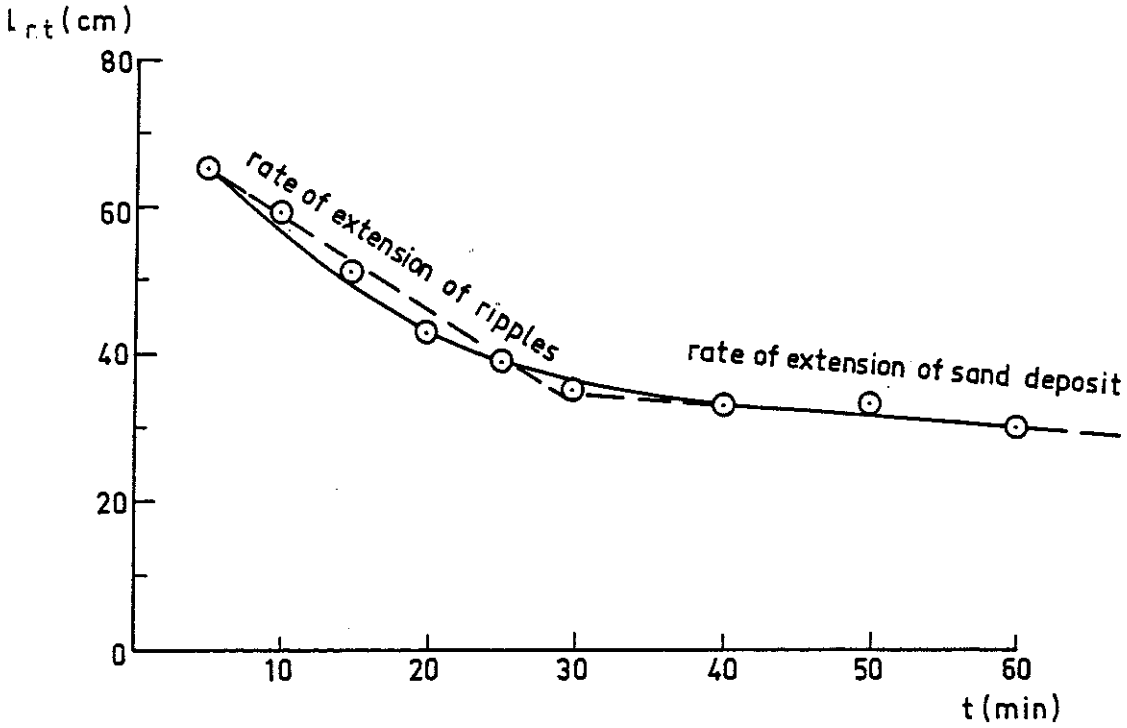

Fig. 18 $l_{r.t.}$ as function of t

(test No.19b, h = 50 cm, H = 8.0 cm, T = 3.12 s , D_{50} = 106 µm)

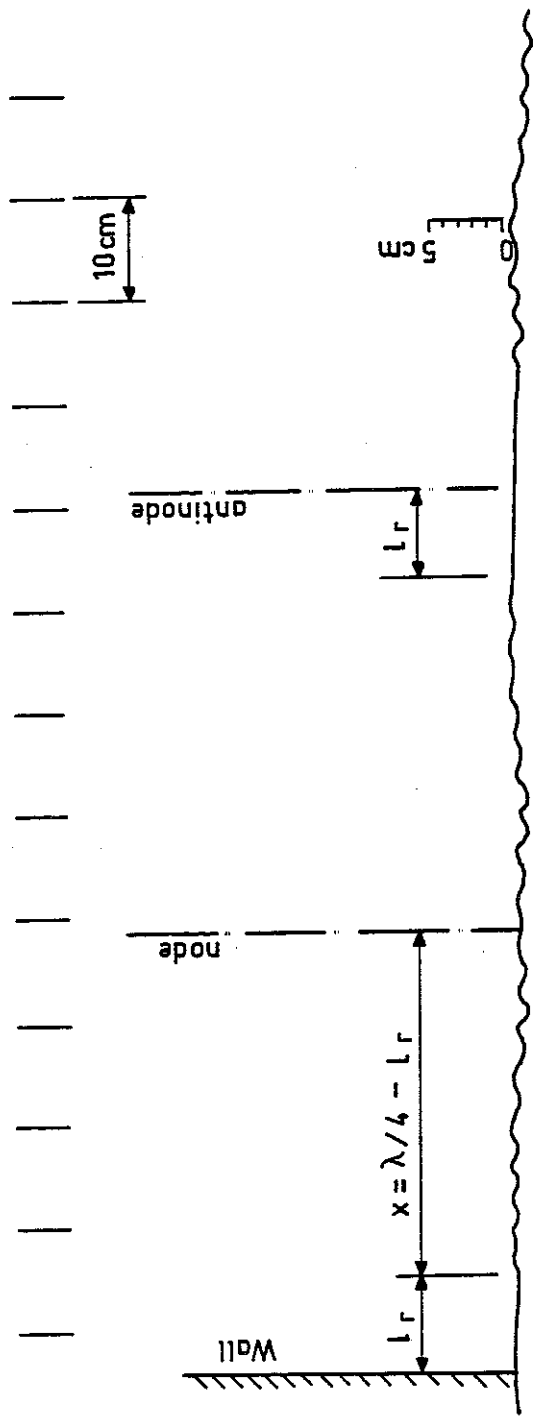

Fig. 19 Bottom profile of test No.1a

(H = 5.0 cm, T = 1.17 s, 30 min. after starting waves)

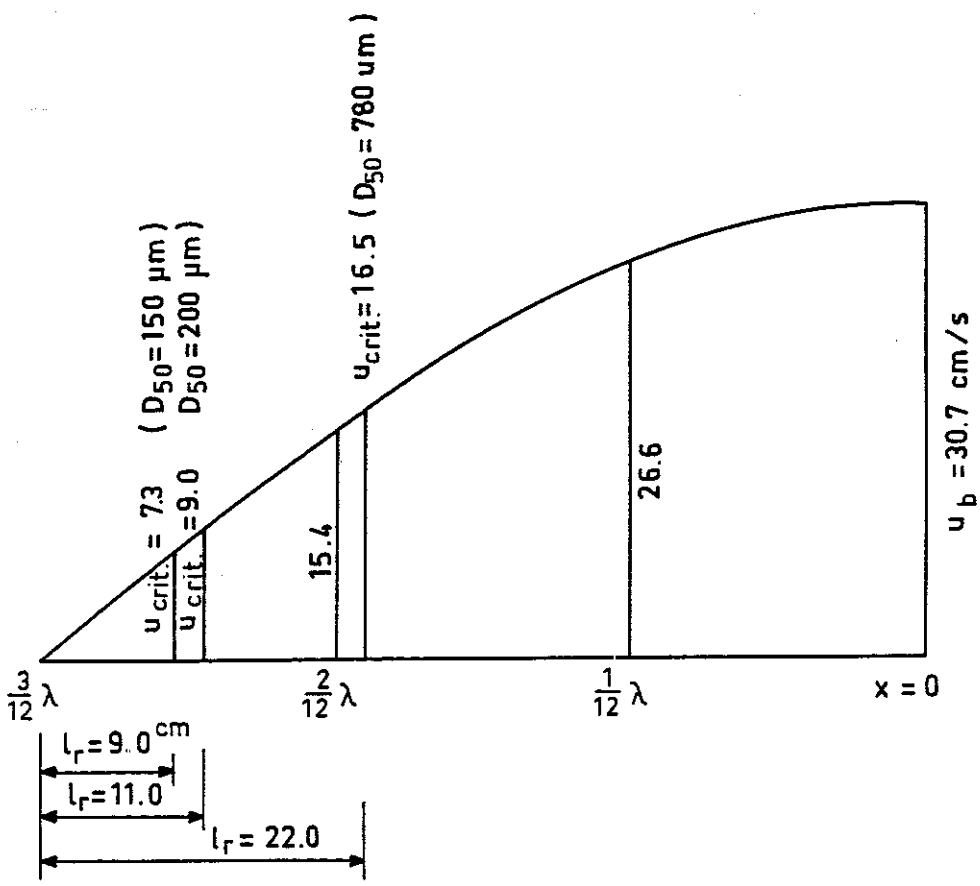

Fig. 20 Maximum orbital velocities at bottom as function of x of tests No. 13a, 17a and 23a ($H = 6.5$ cm, $T = 1.53$ s)

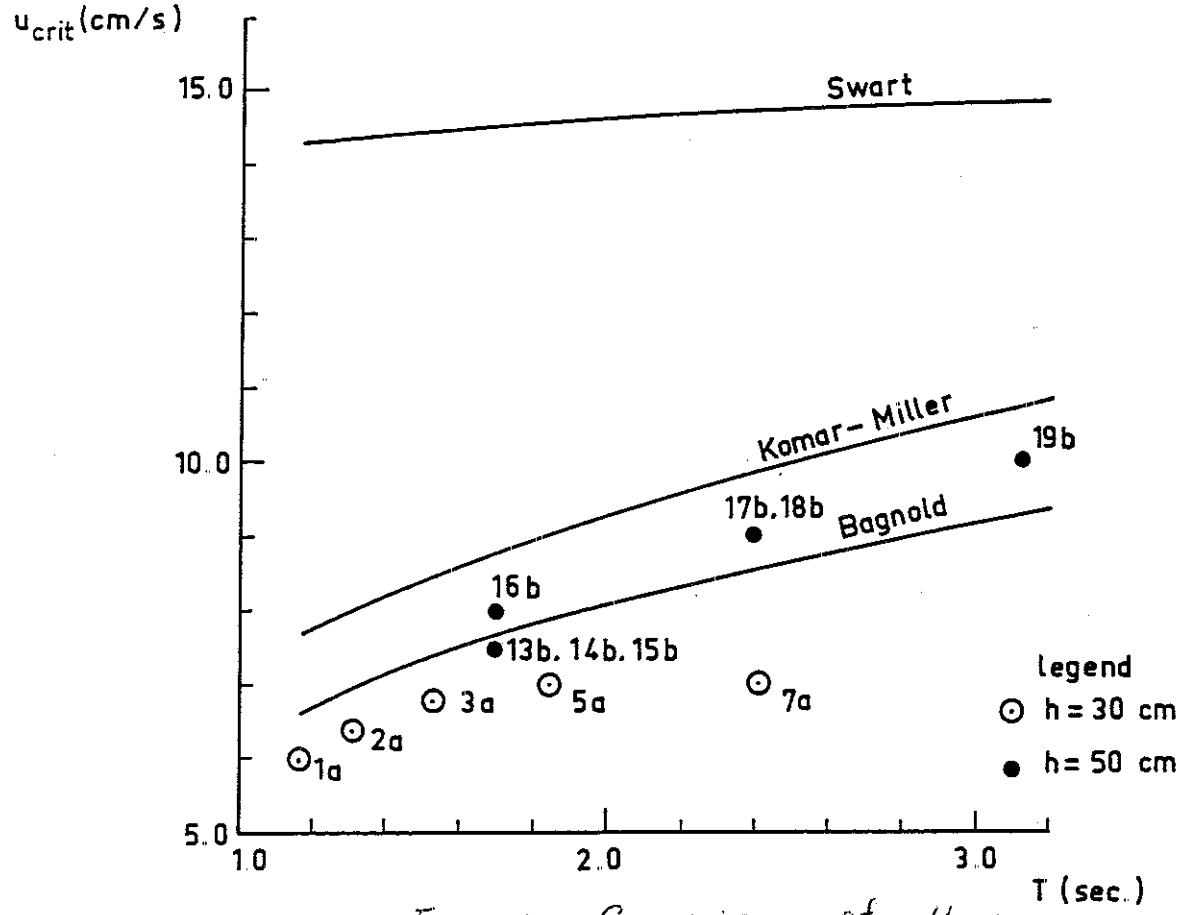

Fig. 21 Comparison of u_{crit}
(D_{50} = 106 µm)

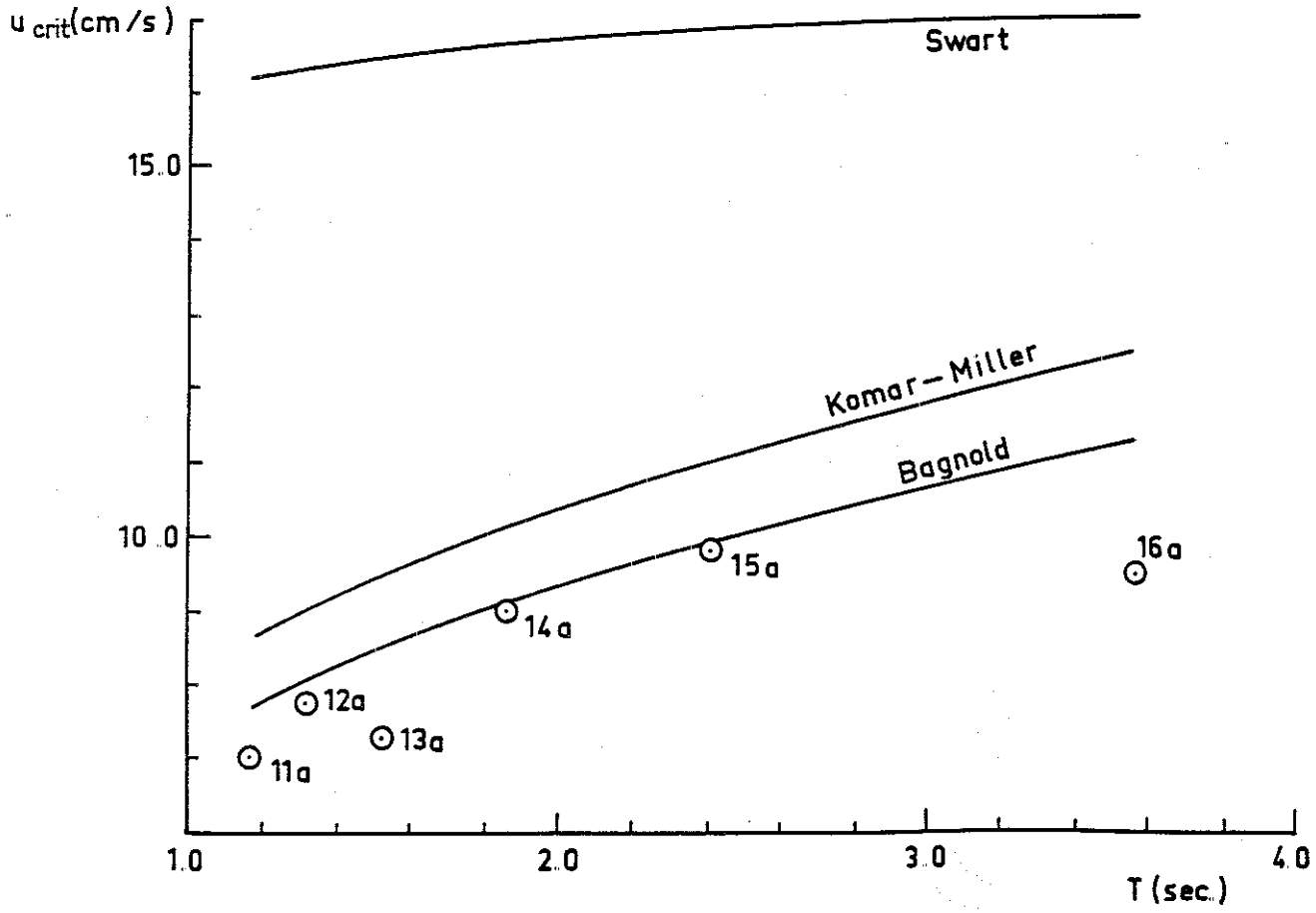

Fig. 22 Comparison of u_{crit}
(D_{50} = 150 µm)

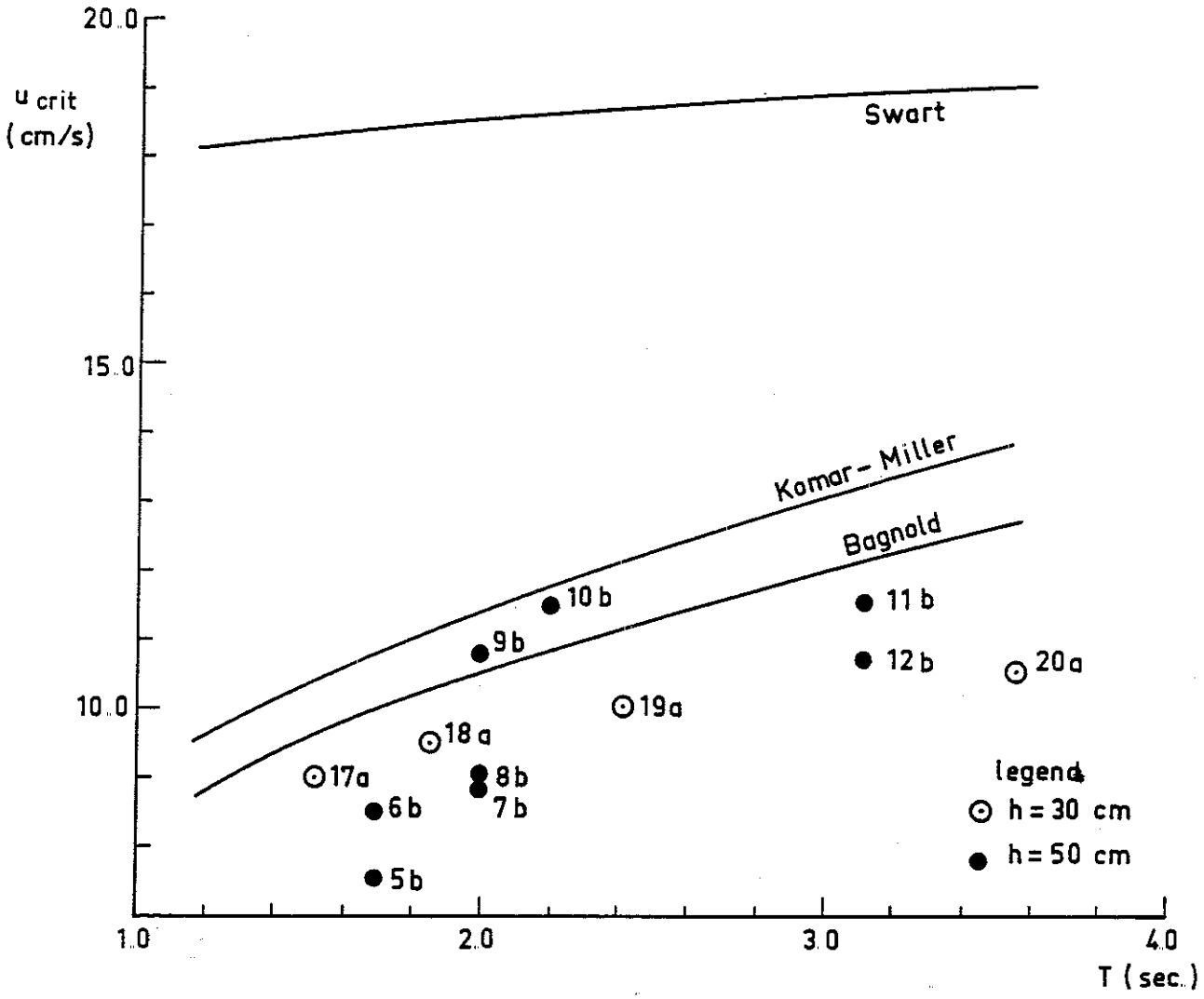

Fig. 23 Comparison of u_{crit}

(D_{50} = 200 µm)

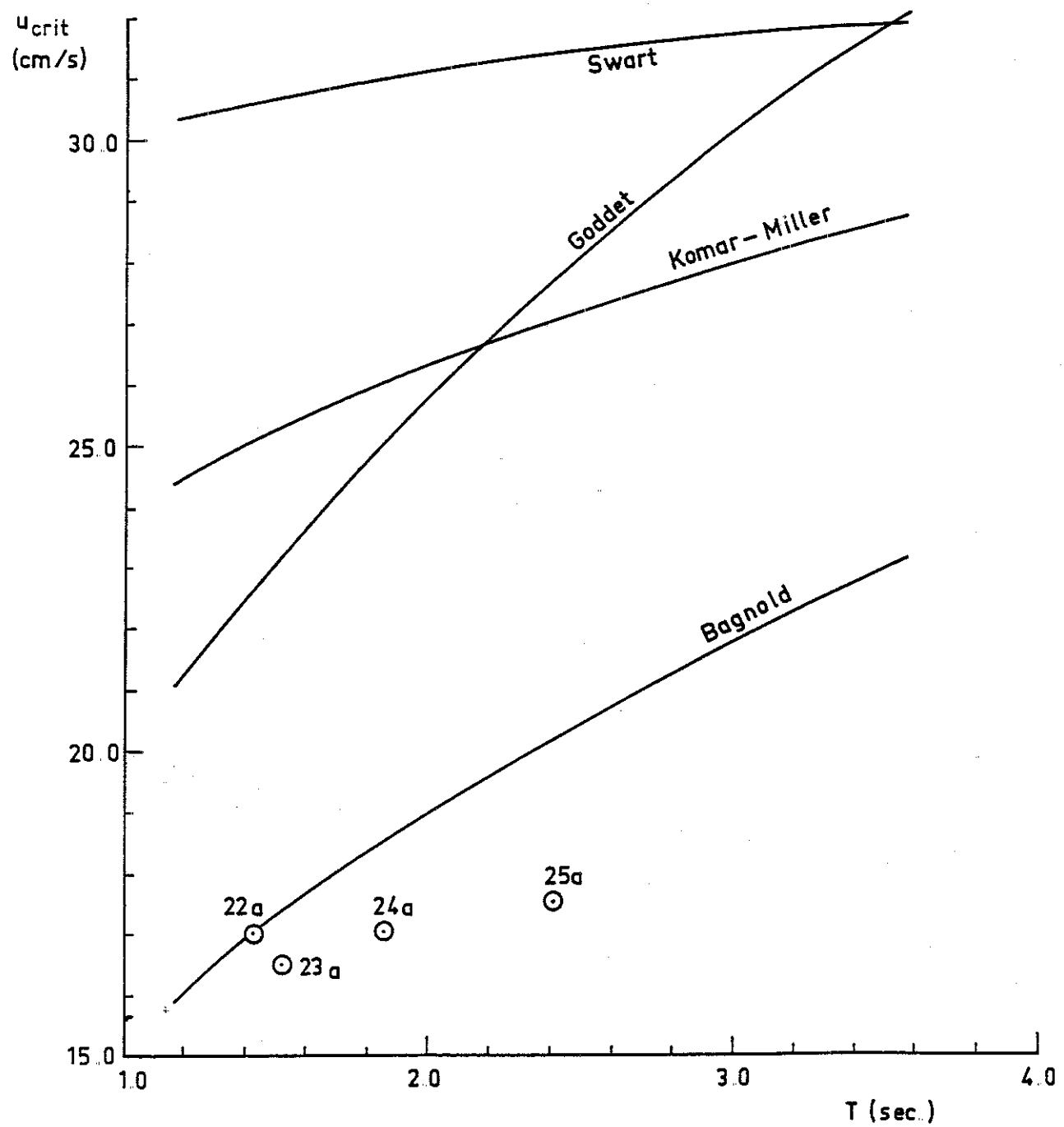

Fig. 24 Comparison of u_{crit}

(D_{50} = 780 µm)

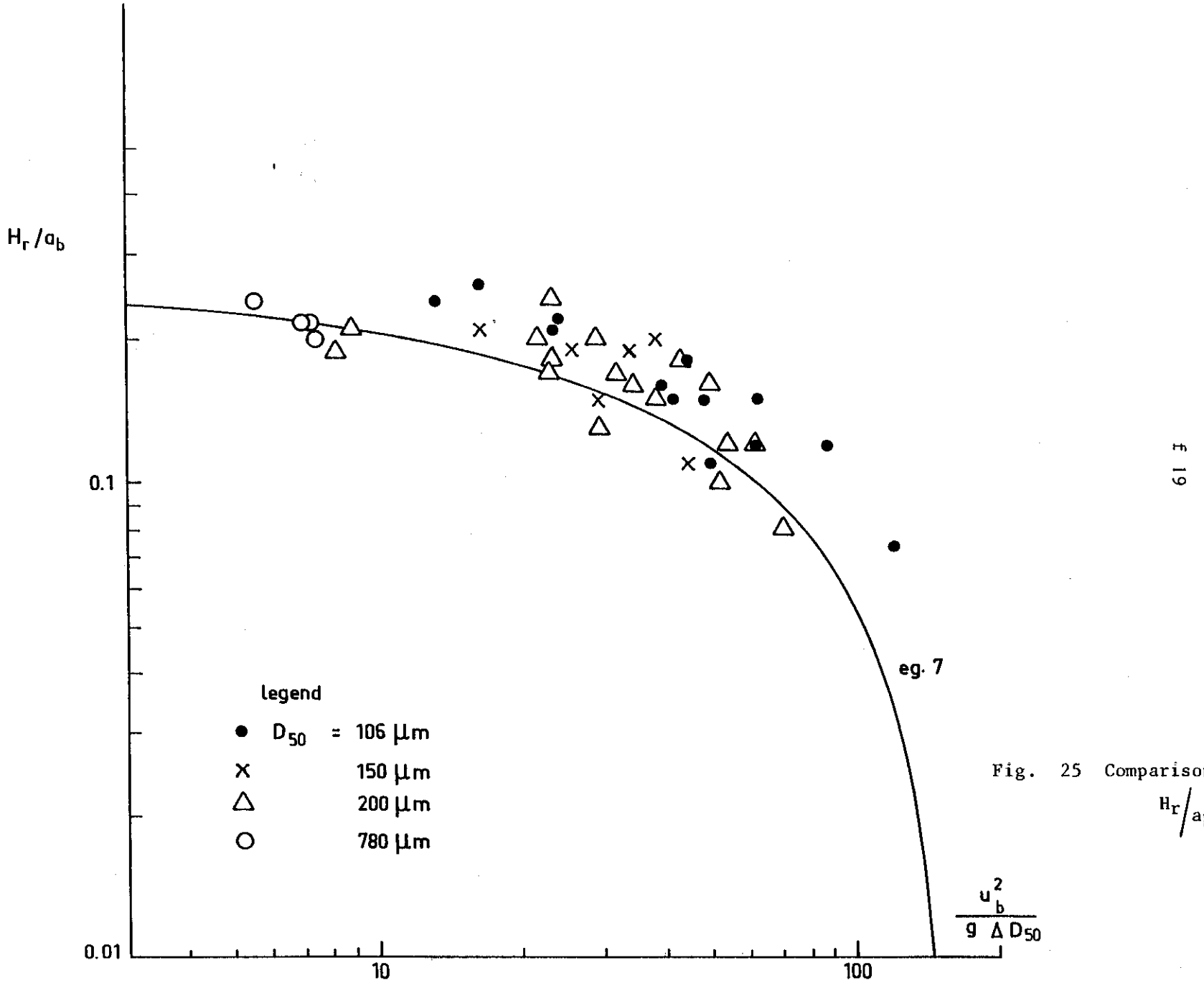

Fig. 25 Comparison of H_r/a_b

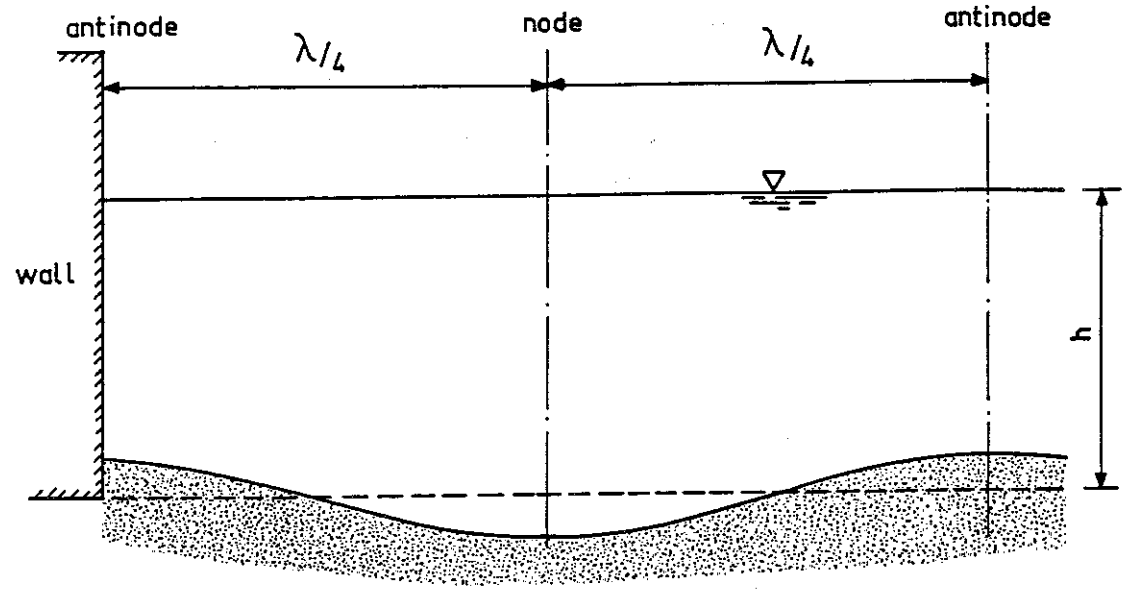

a. for relatively fine sand

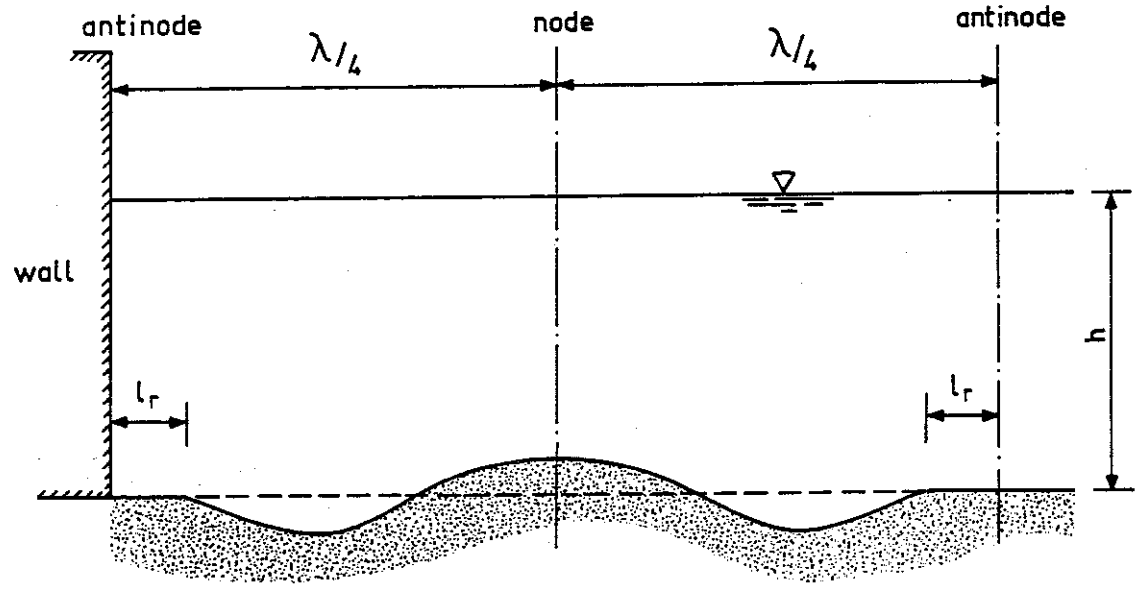

b. for relatively coarse sand

Fig. 26 Two basis scouring patterns
in front of a vertical wall

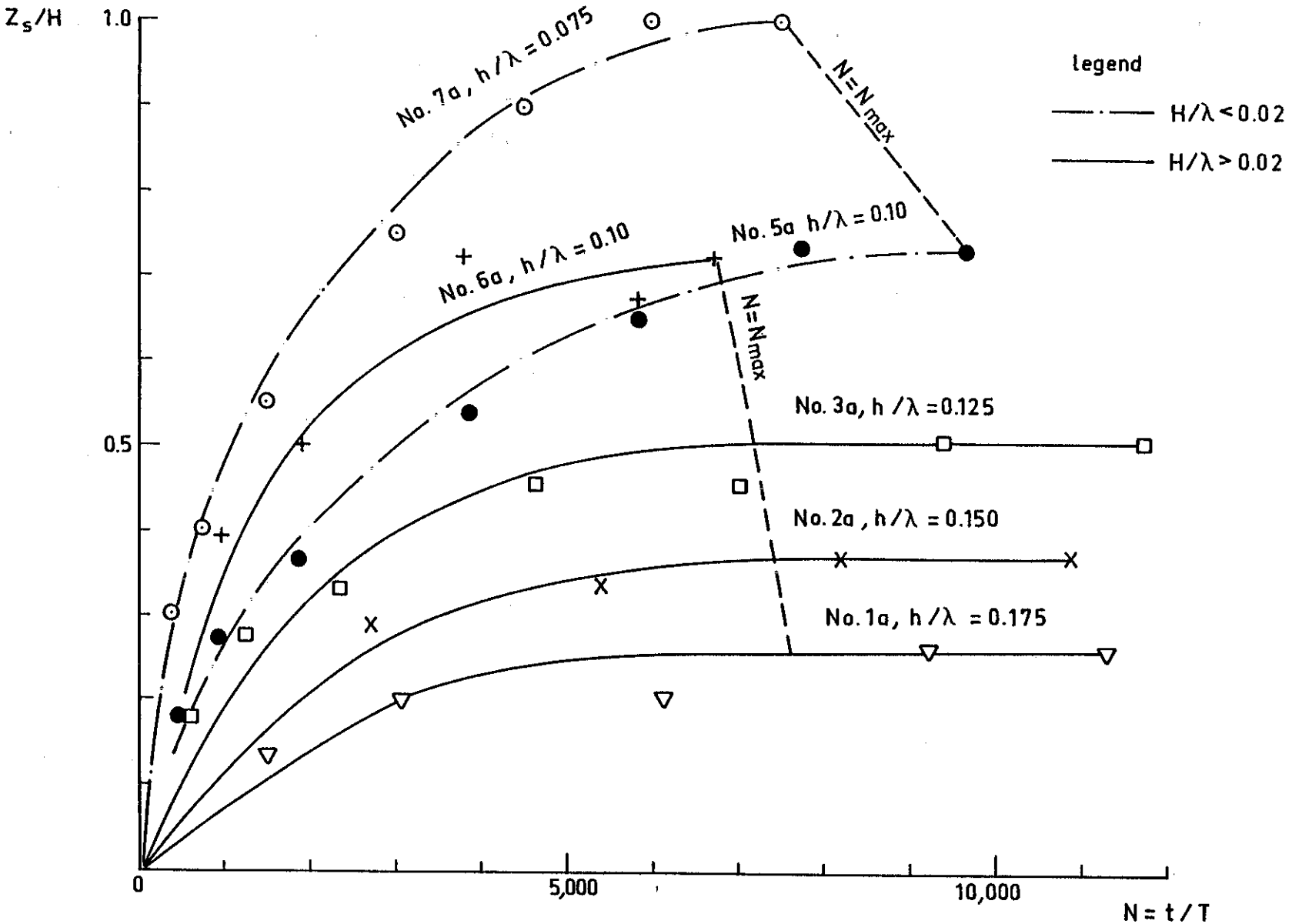

Fig. 27 Development of the scouring depth for relatively fine material

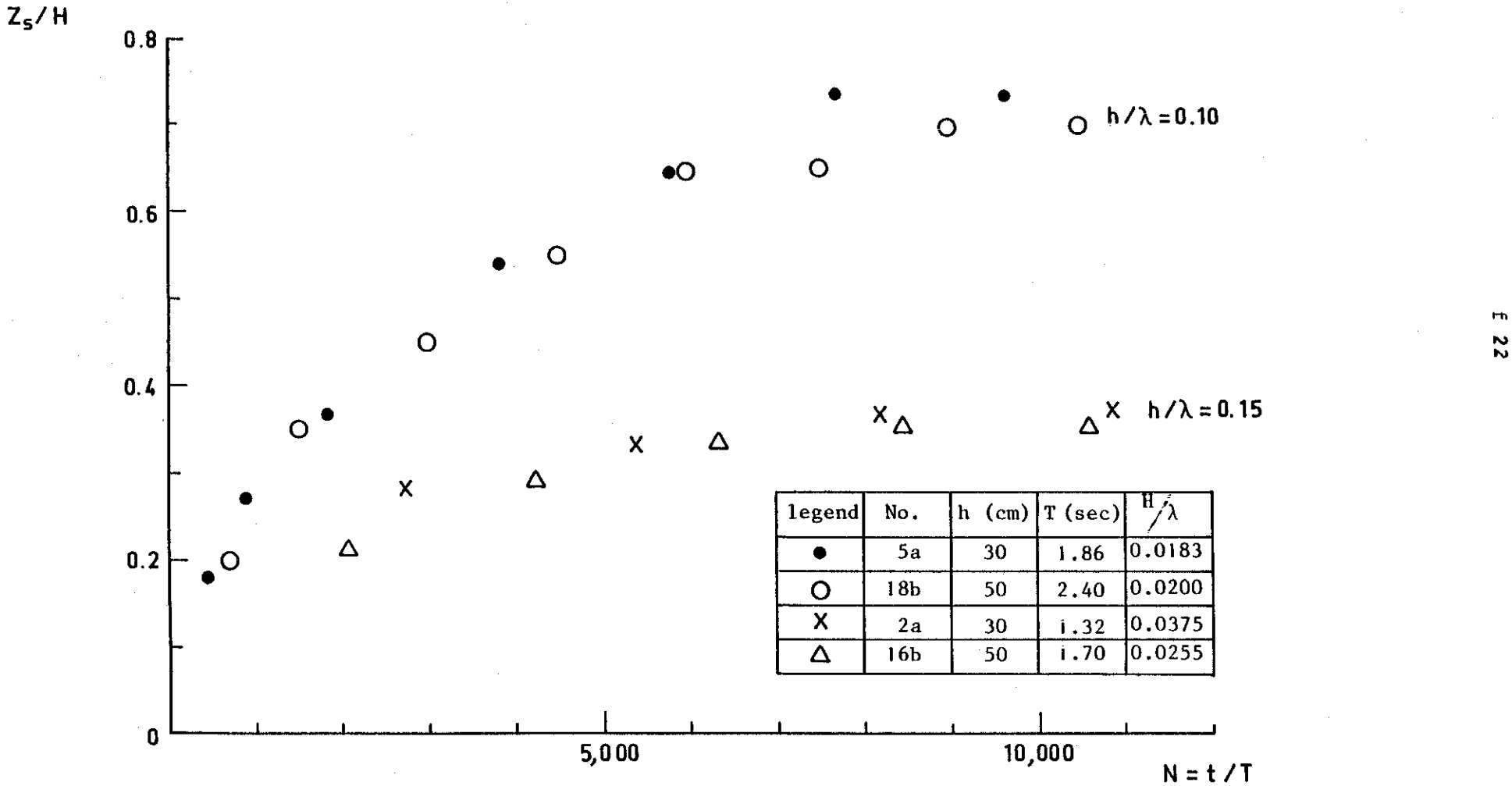

legend	No.	h (cm)	T (sec)	H/λ
●	5a	30	1.86	0.0183
○	18b	50	2.40	0.0200
X	2a	30	1.32	0.0375
△	16b	50	1.70	0.0255

Fig. 28 Z_s/H versus N for different water depth

(D_{50} = 106 μm)

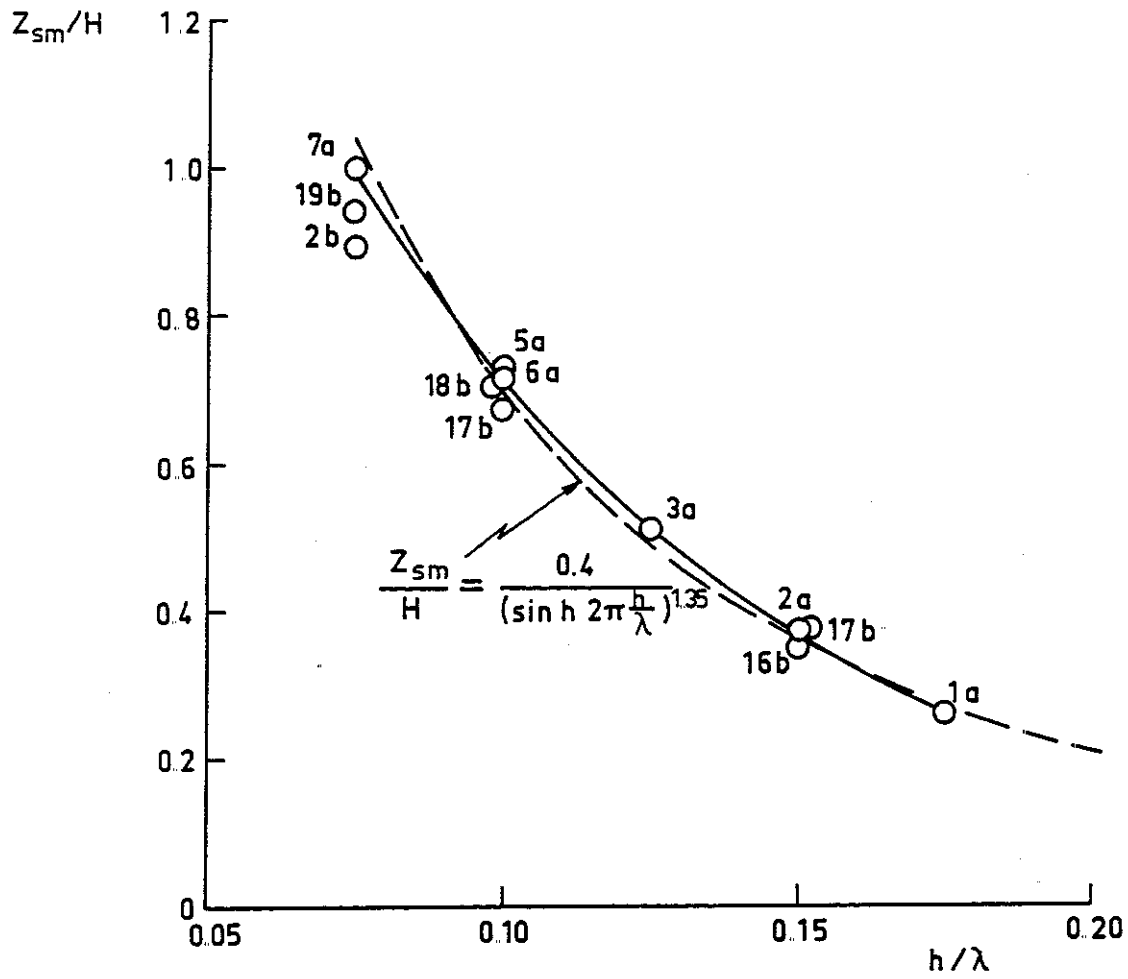

Fig. 29 $^{Z_{sm}}/_{H}$ as function of $^{h}/_{\lambda}$ for relatively fine material

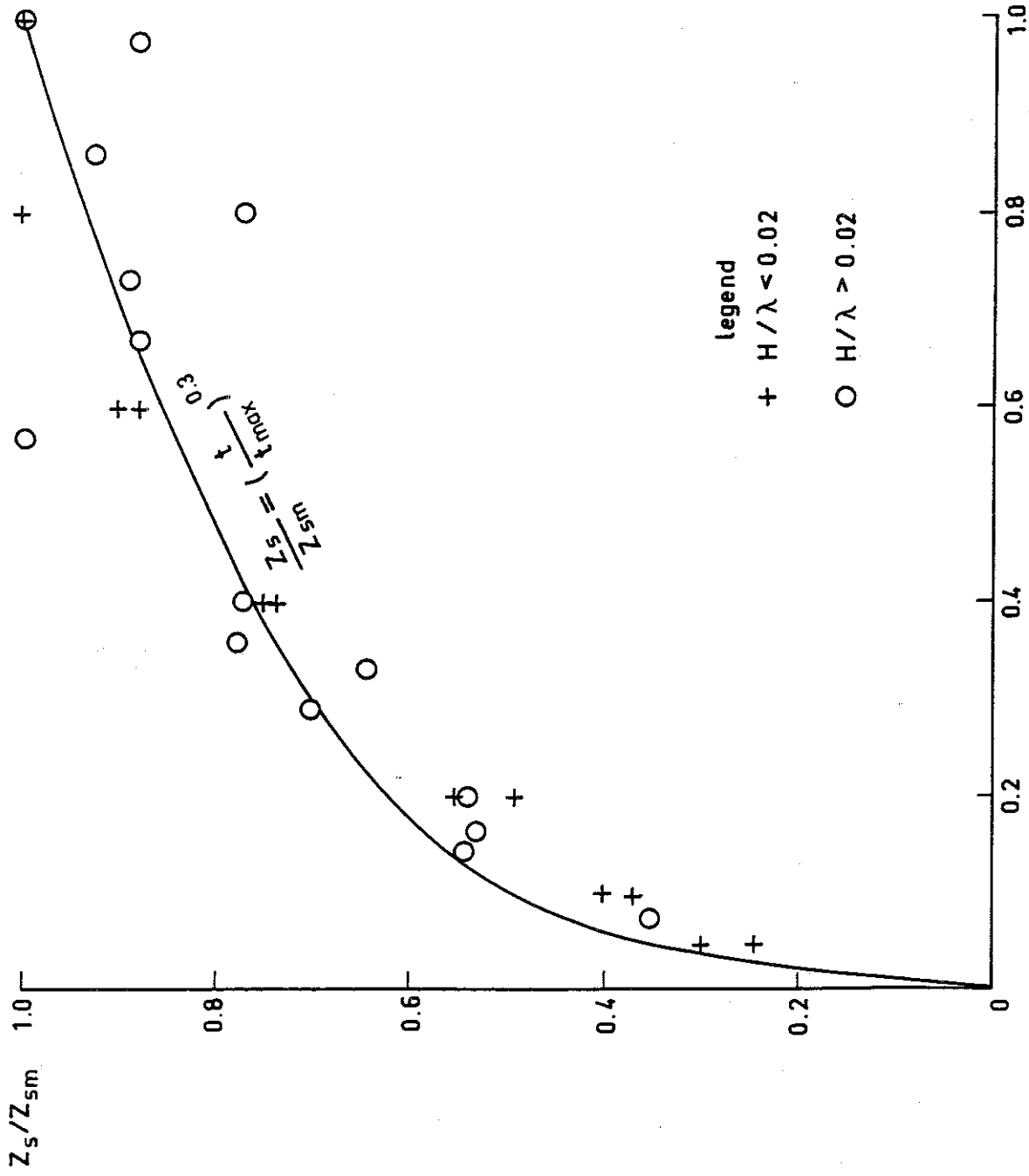

Fig. 30 Z_s/Z_{sm} as function of t/t_{max} for relatively fine material

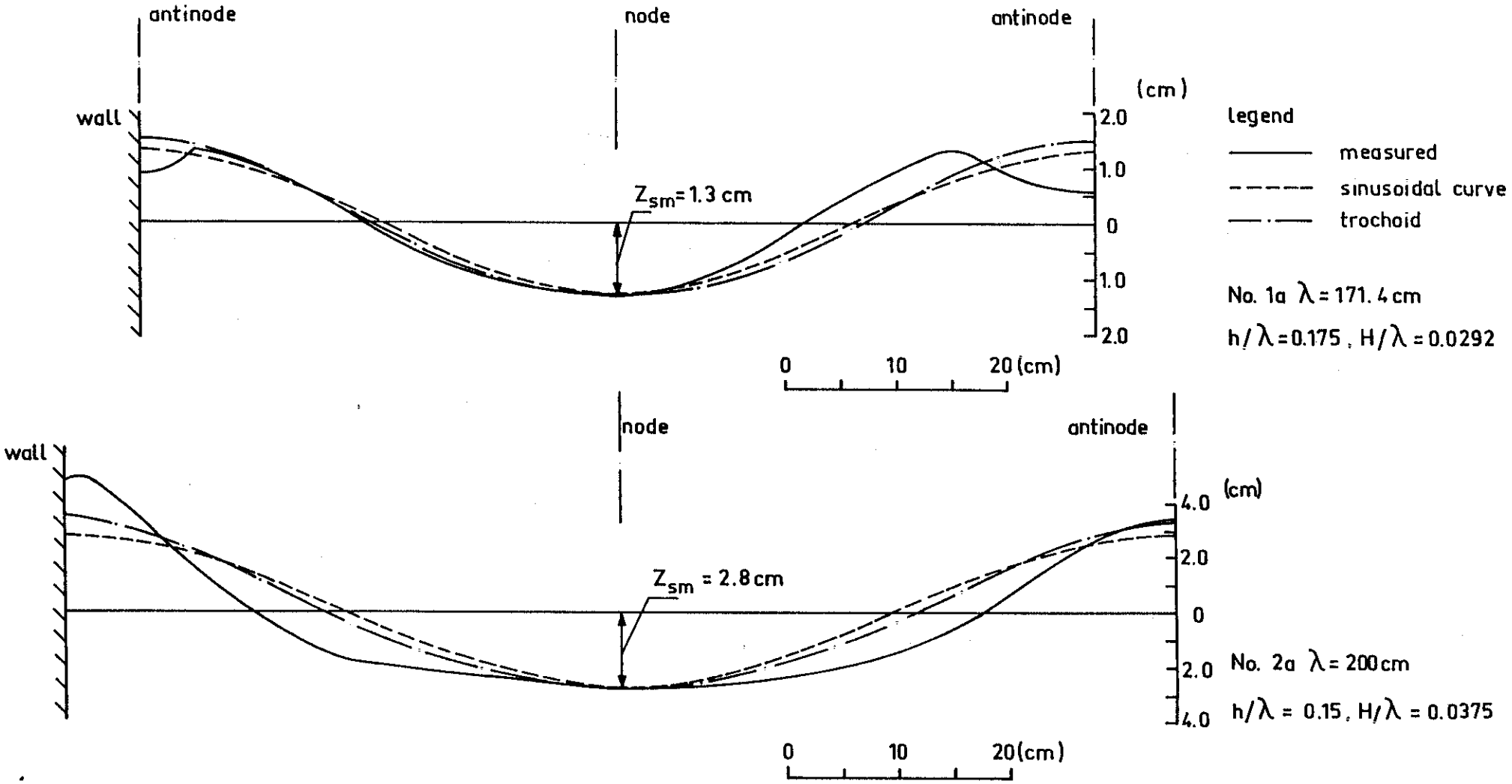

Fig. 31 Comparisons of bottom profiles (tests No.1a and 2a)

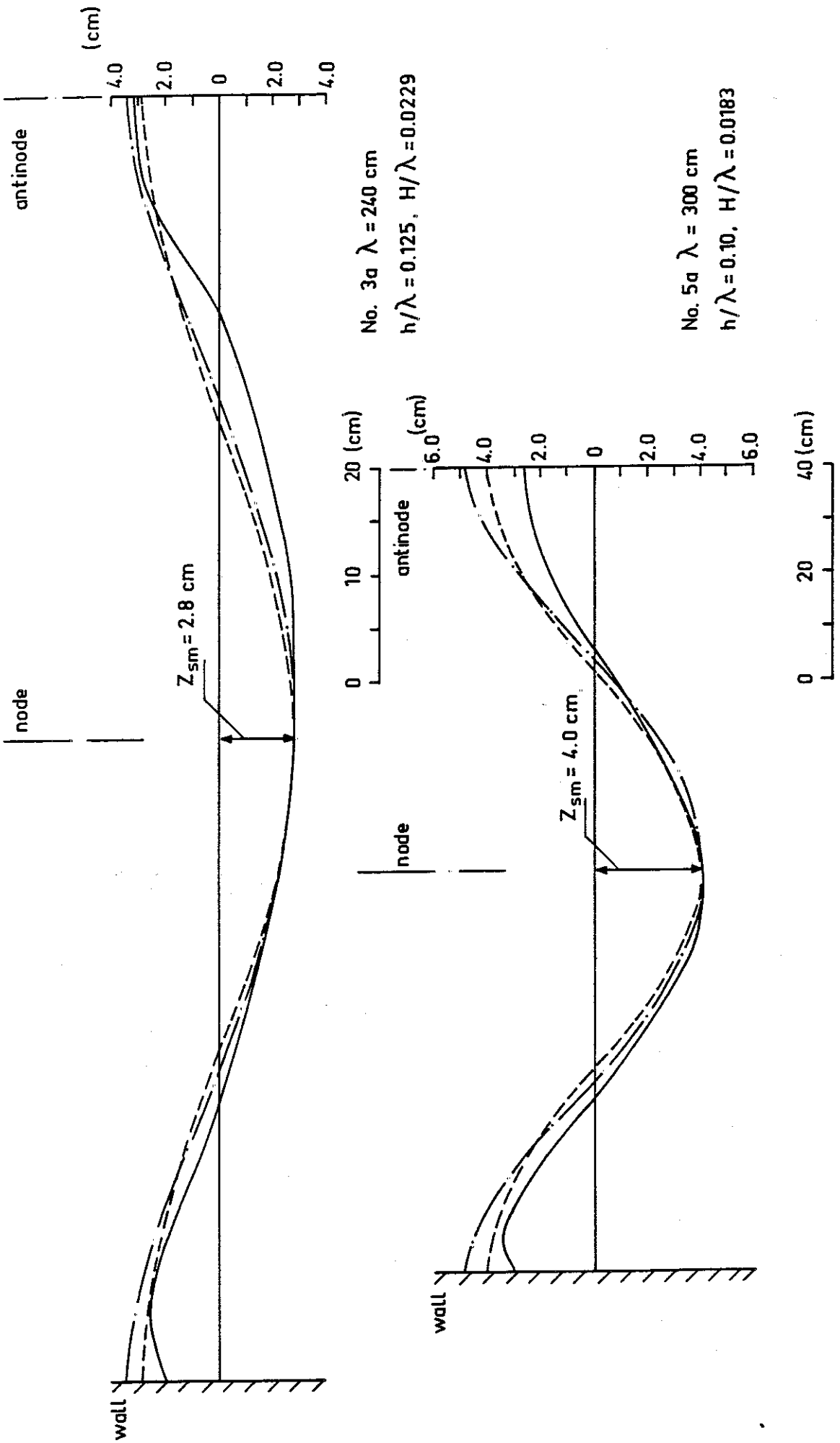

Fig. 32 Comparisons of bottom profiles (tests No.3a and 5a)

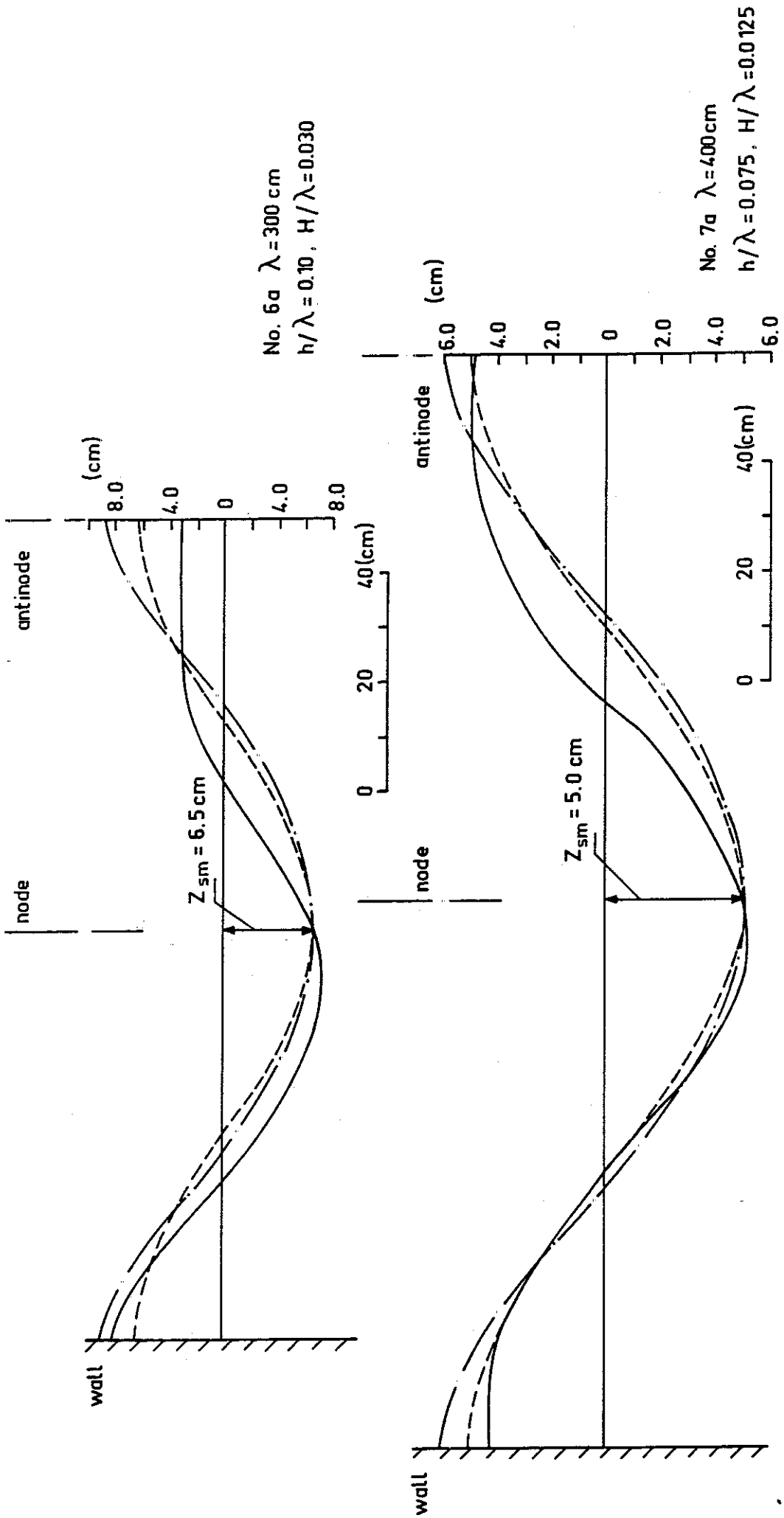

Fig. 33 Comparisons of bottom profiles (tests No.6a and 7a)

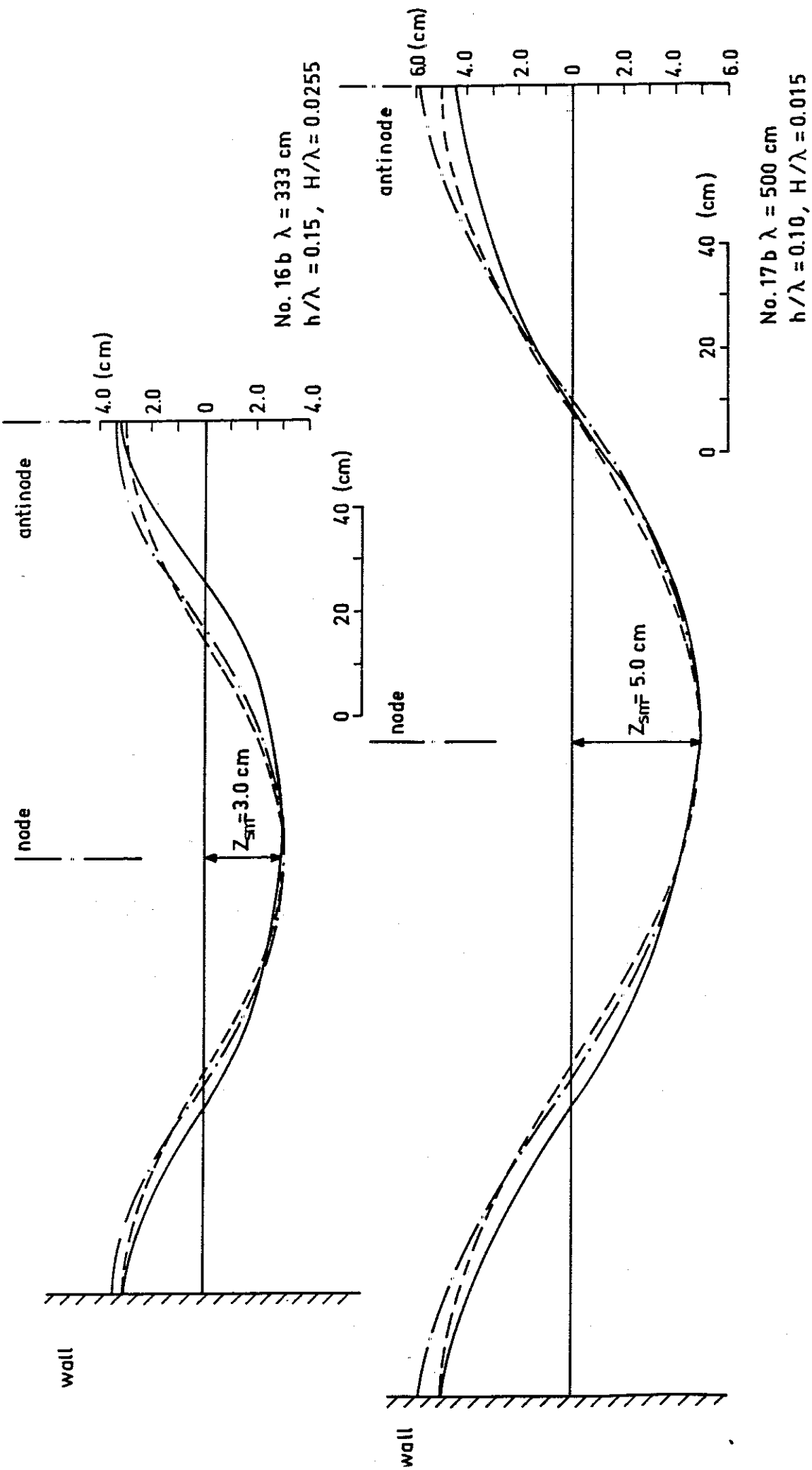

Fig. 34 Comparisons of bottom profiles (tests No. 16b and 17b)

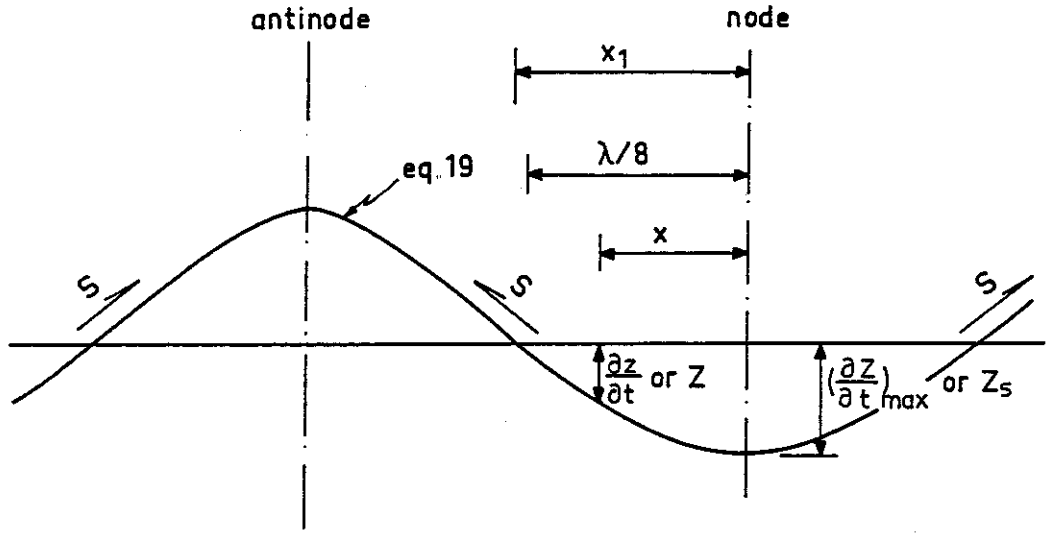

$x = \frac{\lambda}{4}$	$x = x_1 \simeq \frac{\lambda}{8}$	$x = 0$
$\bar{U} = 0$	$\bar{U} \simeq \bar{U}_{max}$	$\bar{U} = 0$
$S = 0$	$S = S_{max}$	$S = 0$
$\frac{\partial z}{\partial t} = (-\frac{\partial z}{\partial t})_{min}$	$\frac{\partial z}{\partial t} = 0$	$\frac{\partial z}{\partial t} = (\frac{\partial z}{\partial t})_{max}$
$Z = (-Z)_{min}$	$Z = 0$	$Z = Z_s$

Fig. 35 Mechanism of sand transport
for relatively fine material

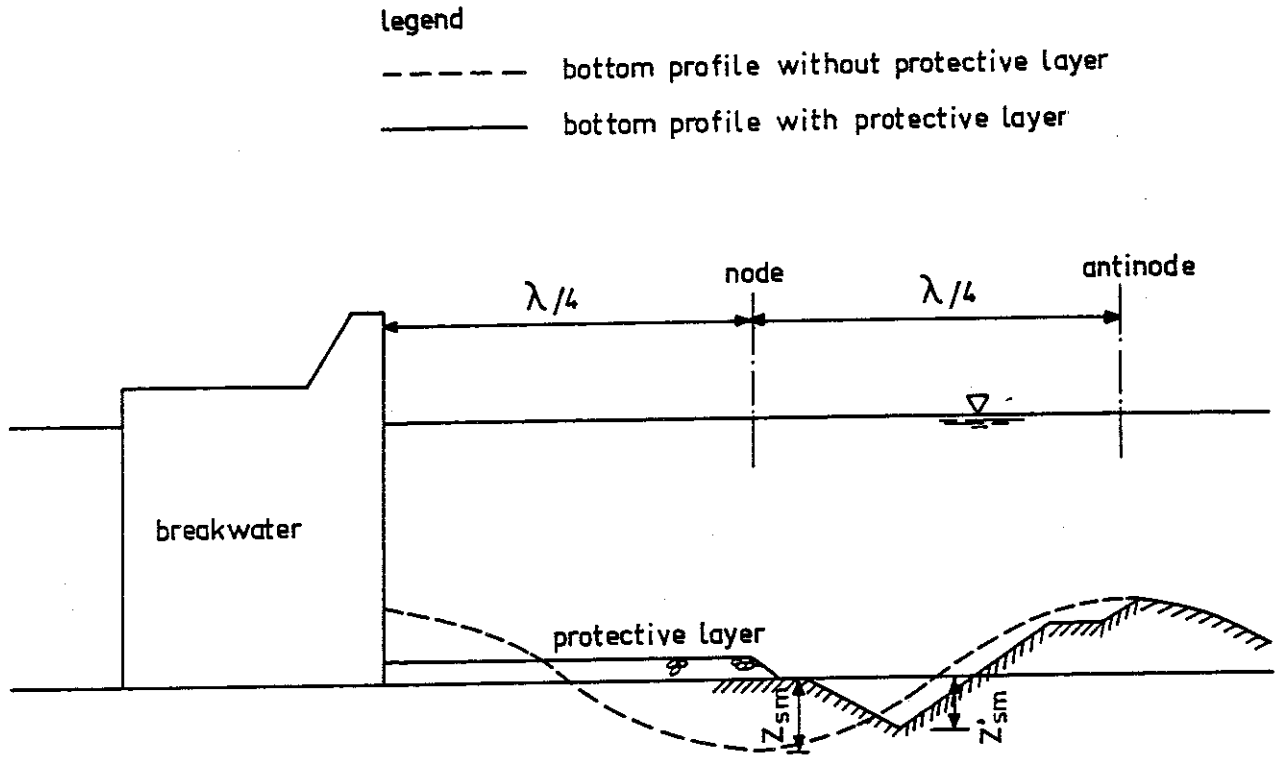

Fig. 36 Influence of the protective layer

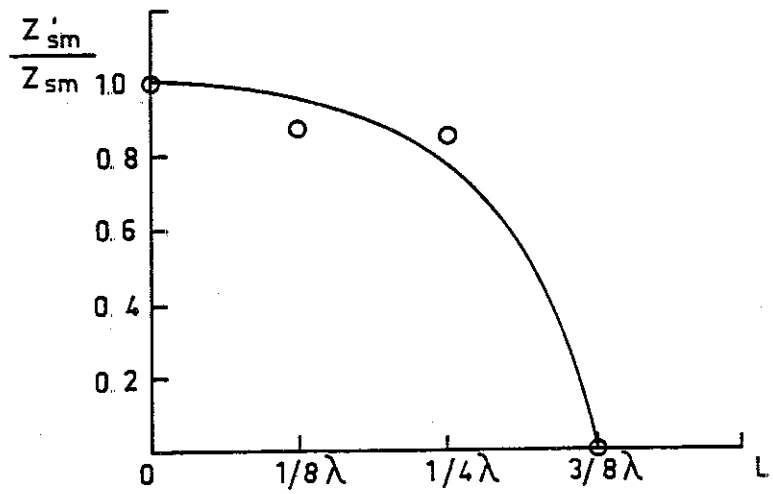

Fig. 37 Z_{sm}' / Z_{sm} versus L

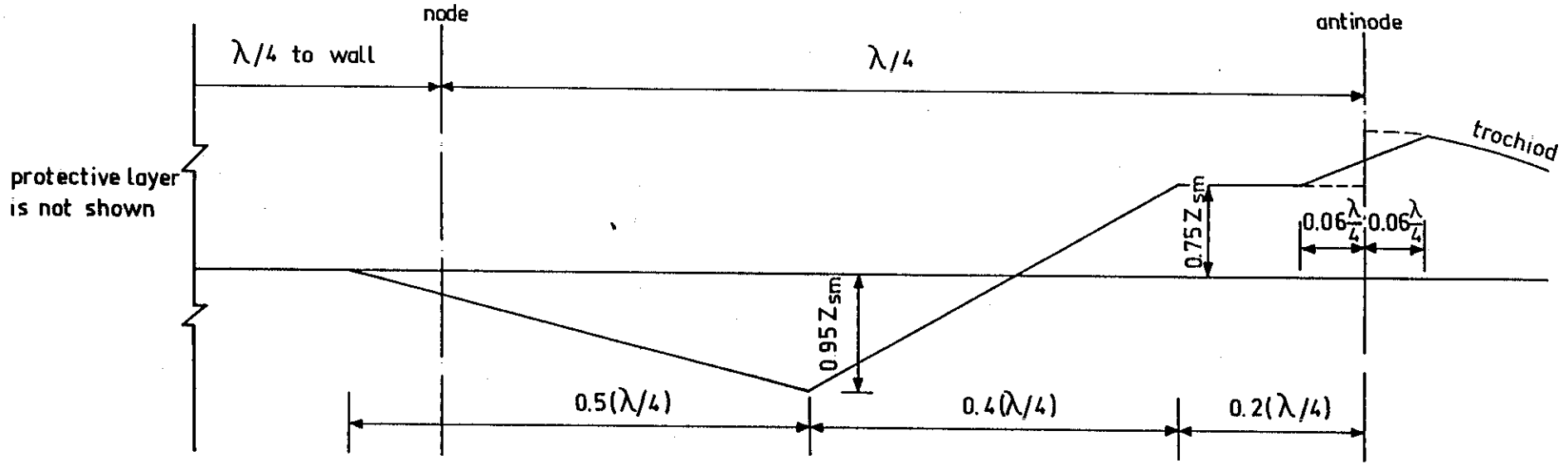

a. L = λ/8

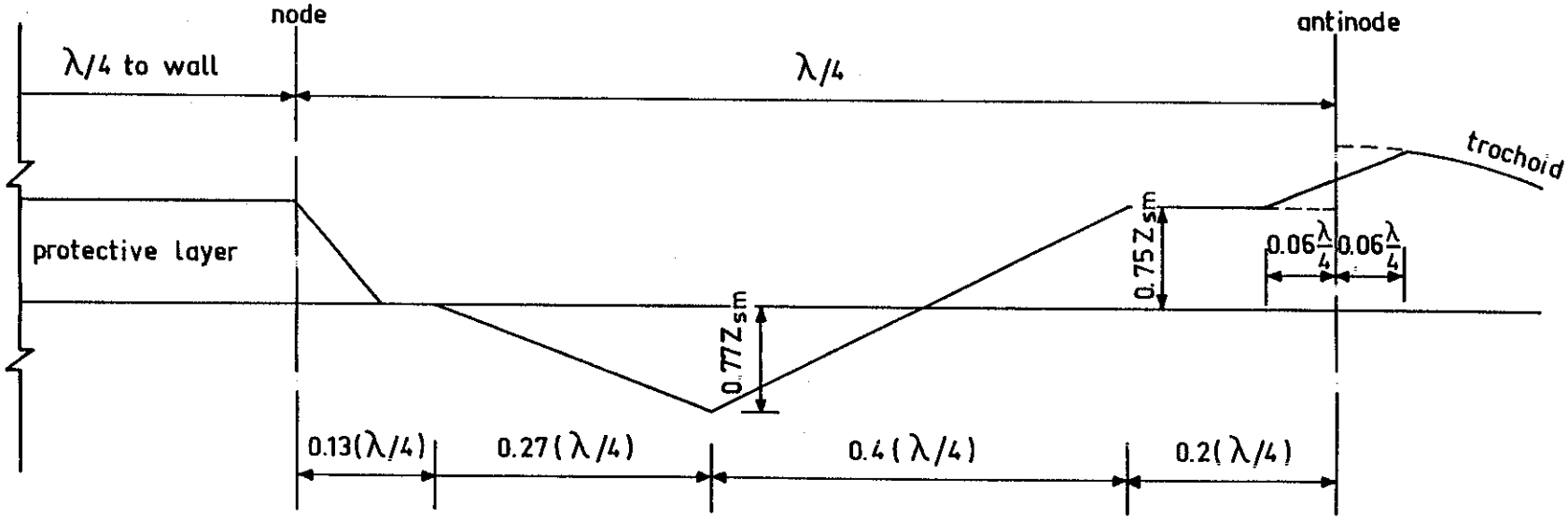

b. L = λ/4

Fig. 38 Detailed bottom profiles for L = $\lambda/8$ and $\lambda/4$

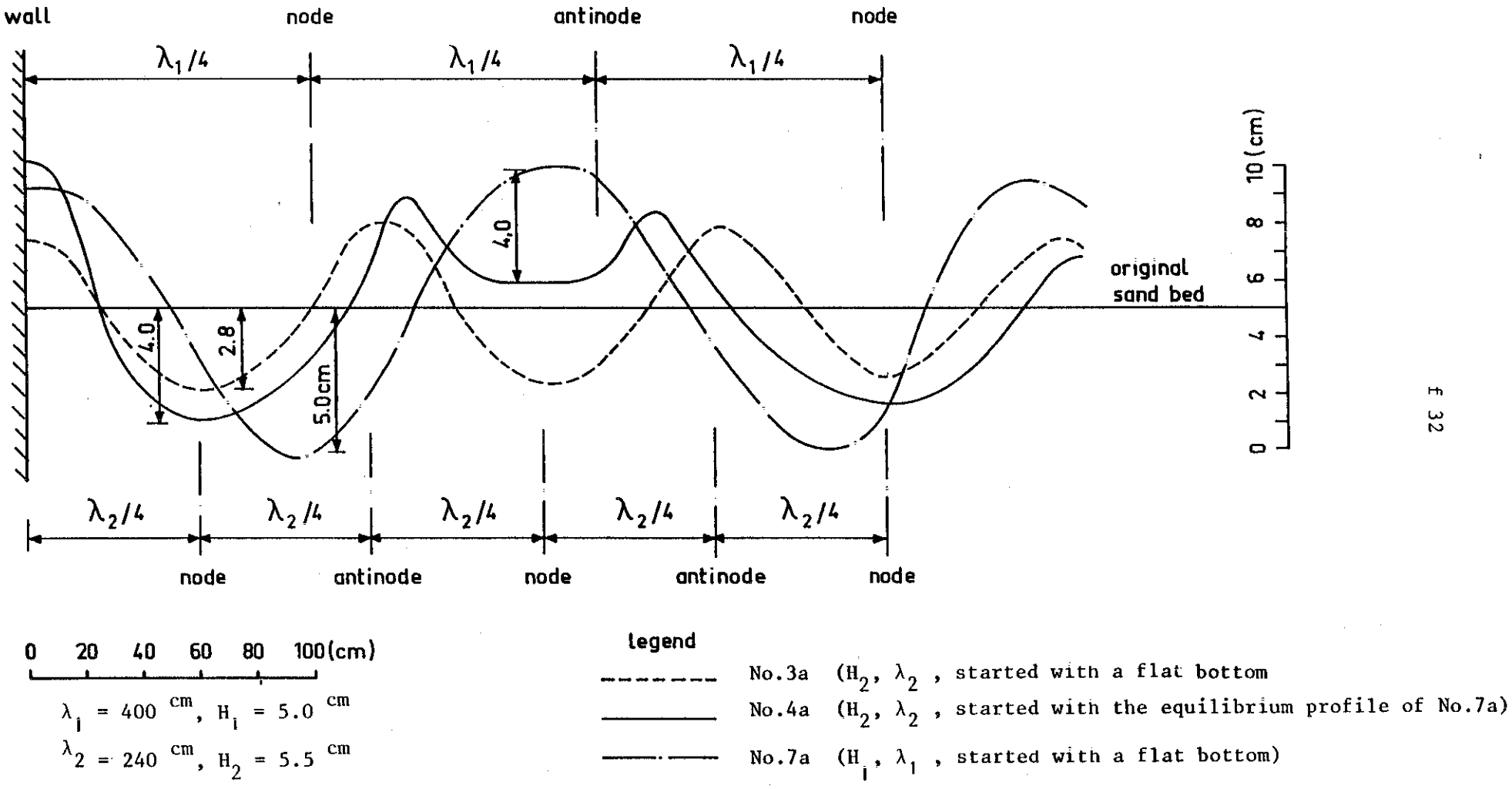

Fig. 39 Equilibrium bottom profiles of tests No. 3a, 4a and 7a

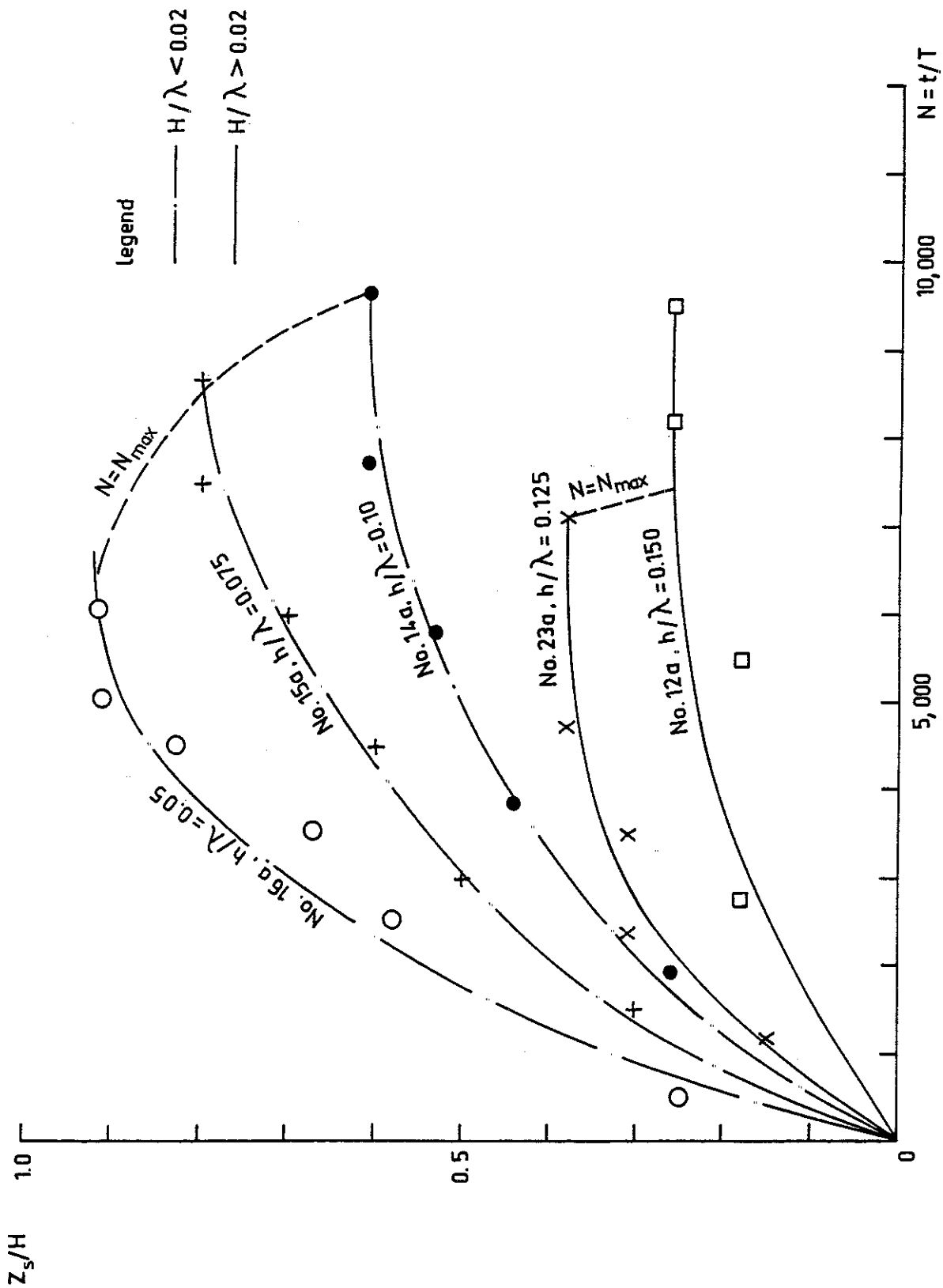

Fig. 40 Development of the scouring depth for relatively coarse material

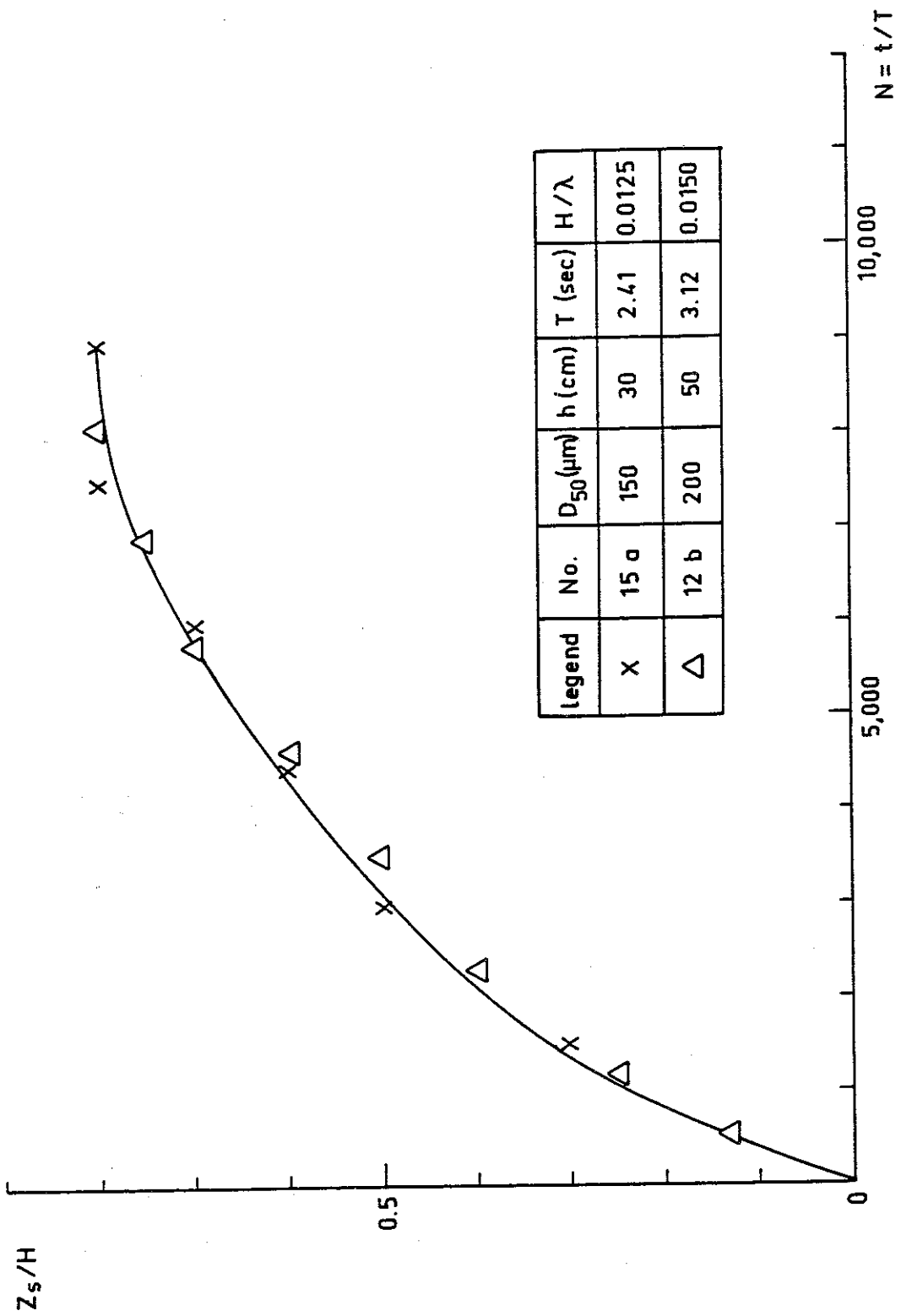

legend	No.	D_{50}(μm)	h (cm)	T (sec)	H/λ
X	15 a	150	30	2.41	0.0125
Δ	12 b	200	50	3.12	0.0150

Fig. 41 Z_s/H versus N for $h/\lambda = 0.075$

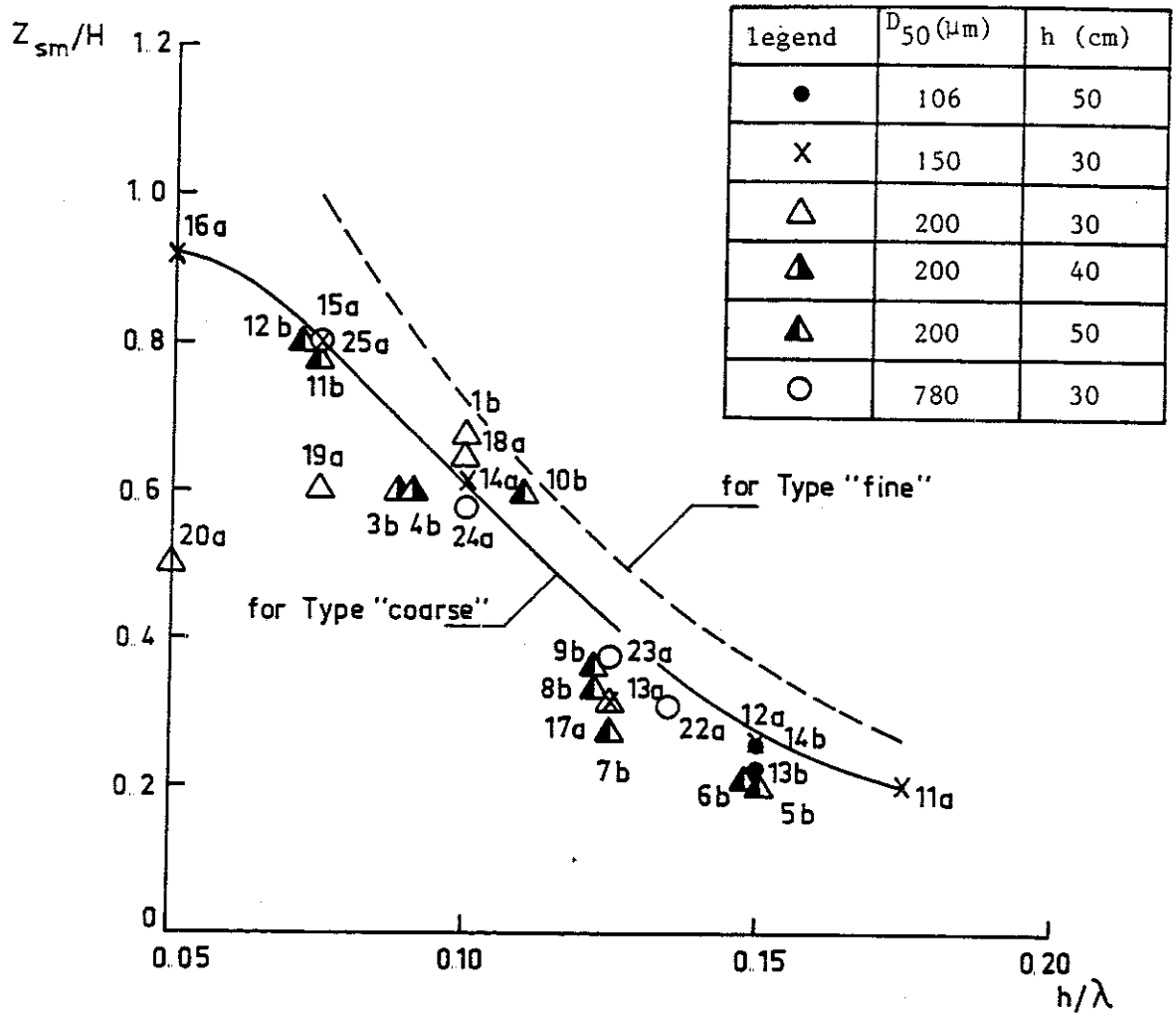

legend	D_{50} (µm)	h (cm)
●	106	50
×	150	30
△	200	30
◭	200	40
▲	200	50
○	780	30

Fig. 42 $Z_{sm}/_{H}$ as function of $h/_{\lambda}$
for relatively coarse material

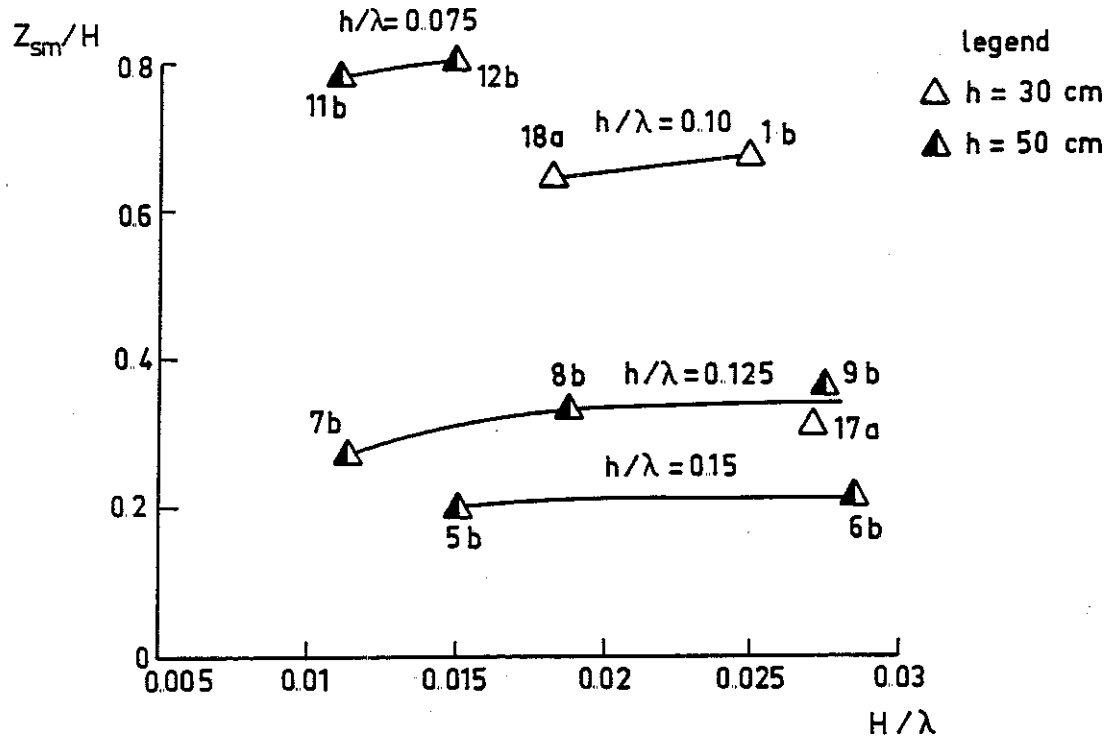

Fig. 43 Influence of H/λ on Z_{sm}/H

(D_{50} = 200 µm)

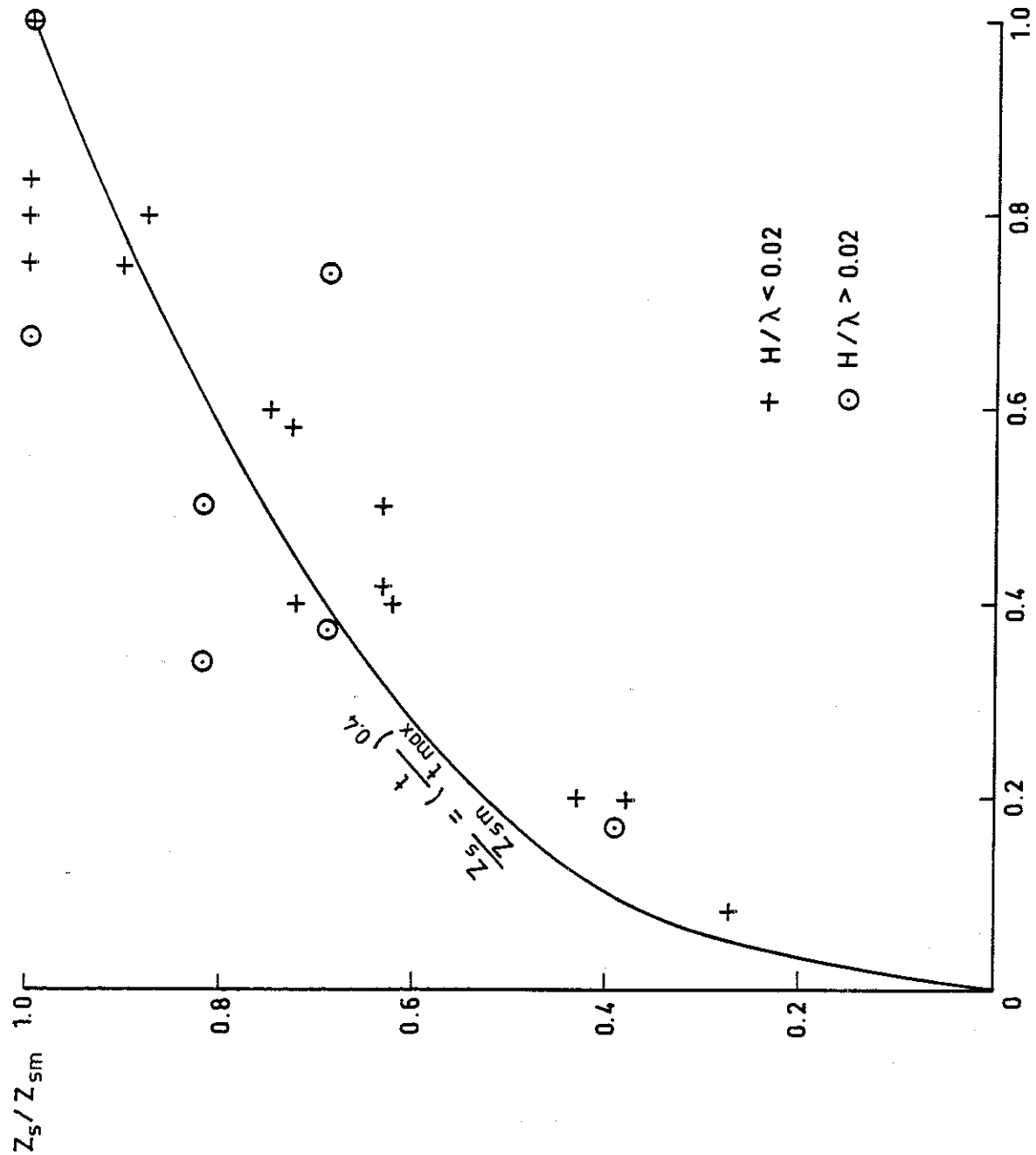

Fig. 44 Z_s/Z_{sm} as function of t/t_{max}
for relatively coarse material

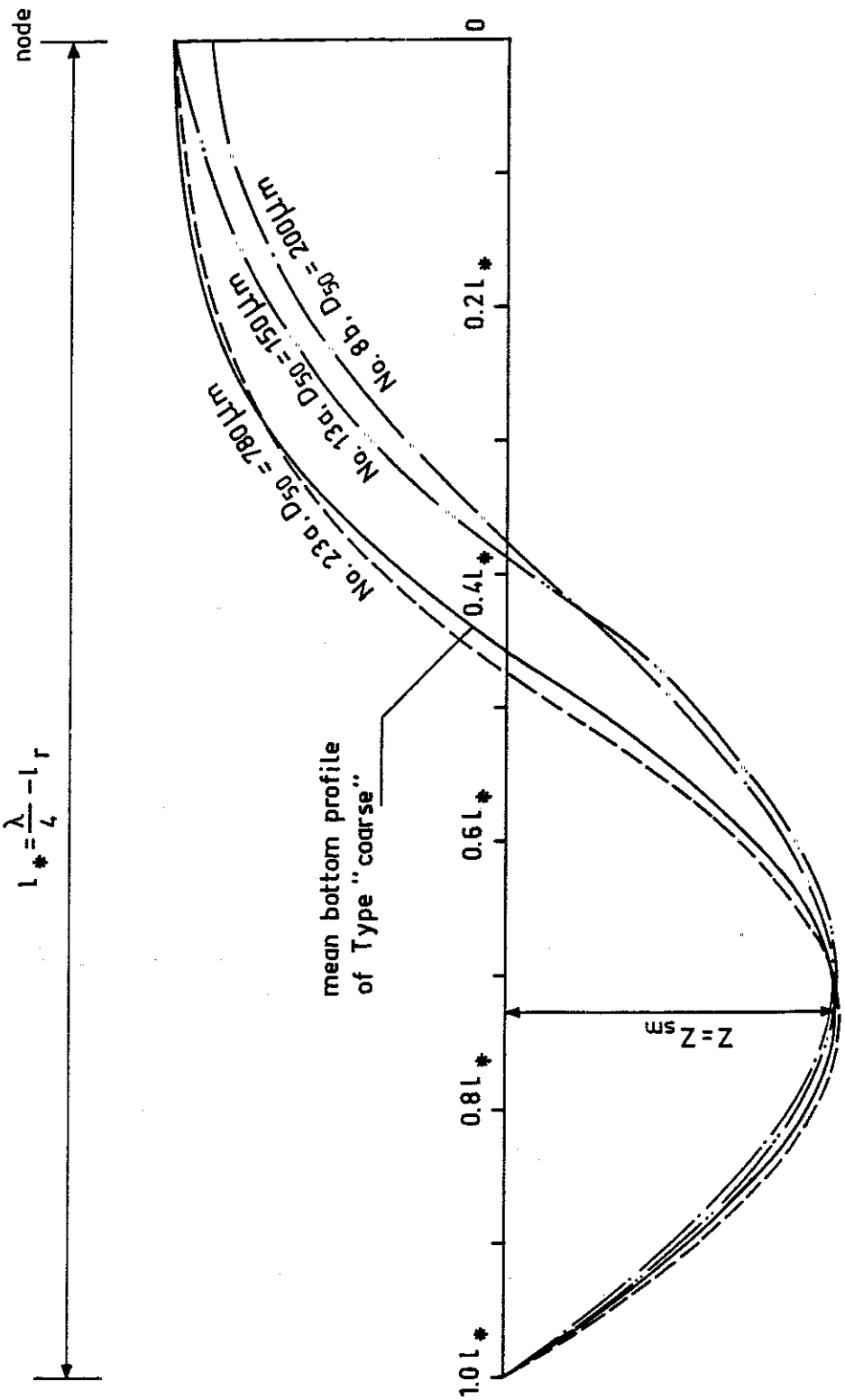

Fig. 45 Test bottom profiles for relatively coarse material

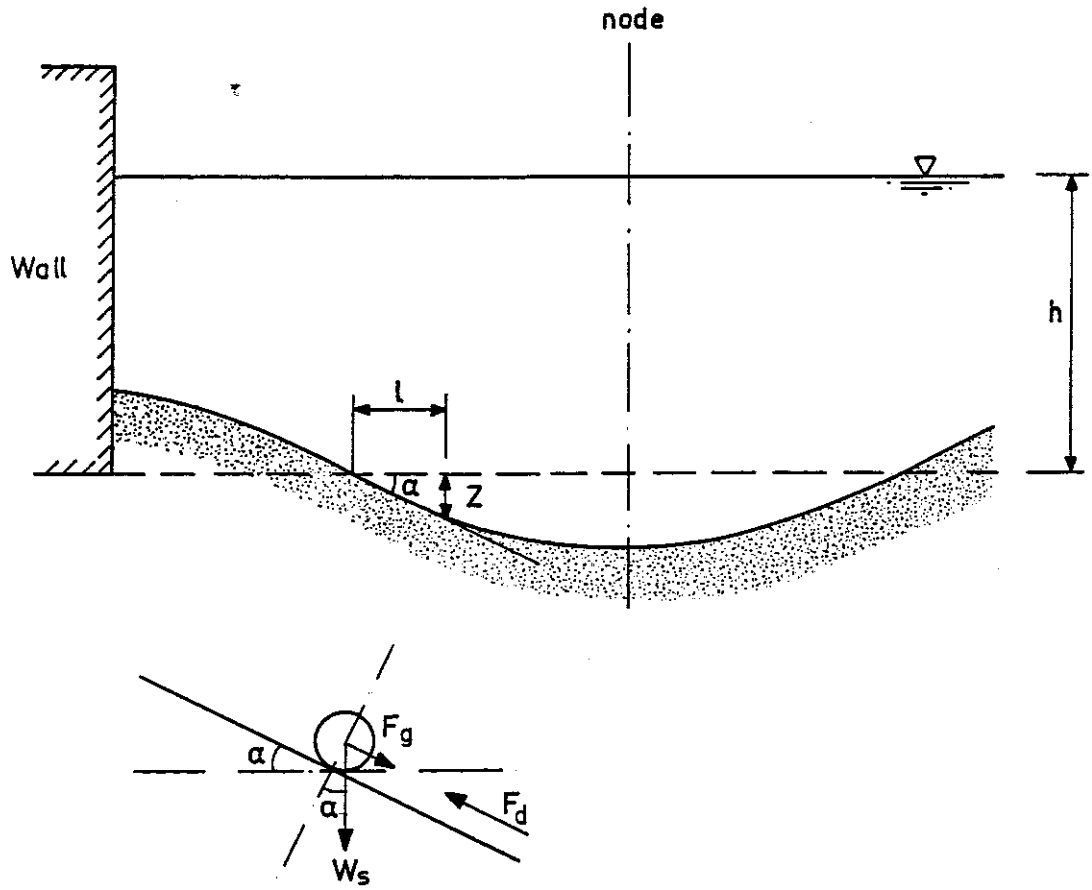

Fig. 46 Forces act on sand particle

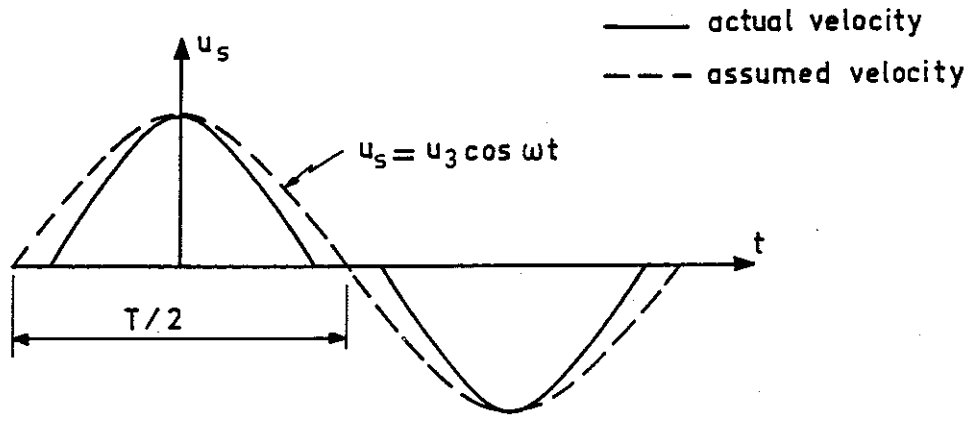

Fig. 47 Movement of sand particle

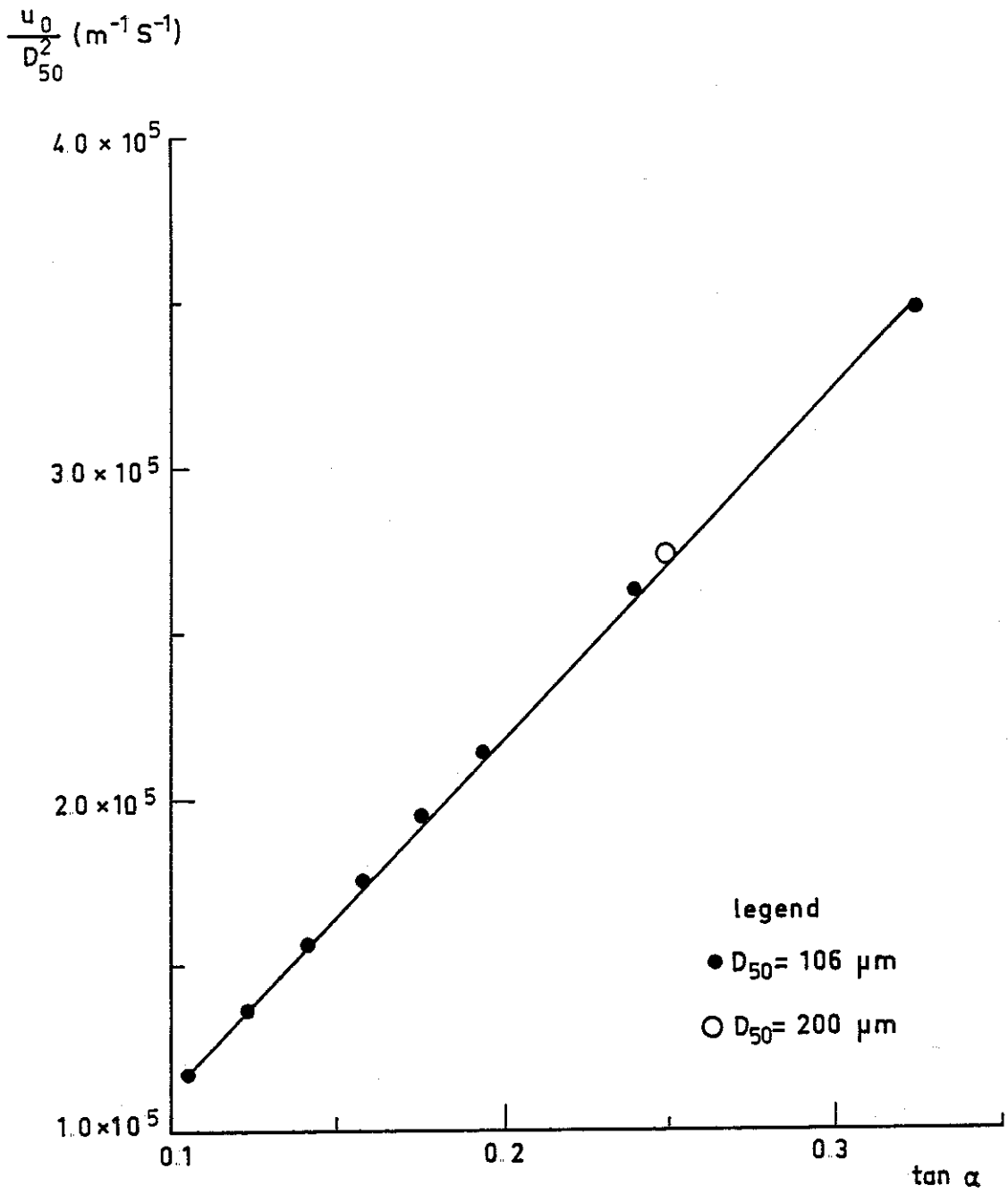

Fig. 48 u_o/D_{50}^2 versus tan α

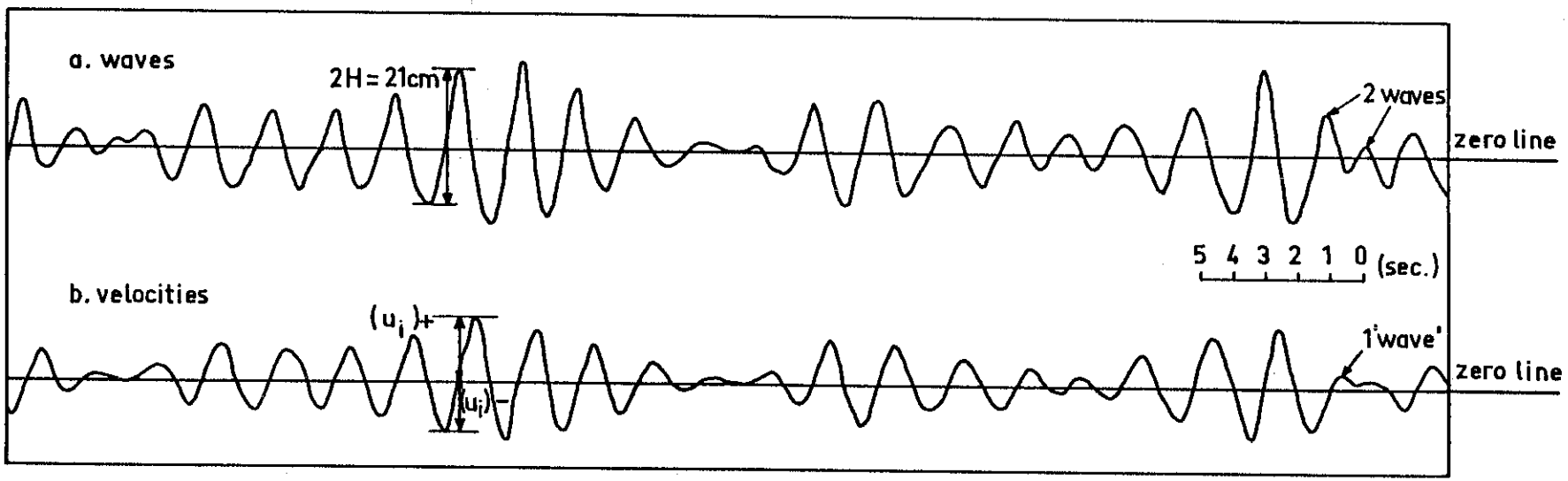

Fig. 49 Wave and orbital velocity profiles of test No.2c

(H_s = 9.1 cm, $\bar{T}$ = 1.98 s, h = 50 cm)

a. waves at $l_1 = 0$ ($x = \lambda/4$)

b. velocities at $l_2 = \lambda/4$ ($x = 0$), Z_b = 10 cm.

λ is the wave length obtained from $\bar{T}$ by eq. 53

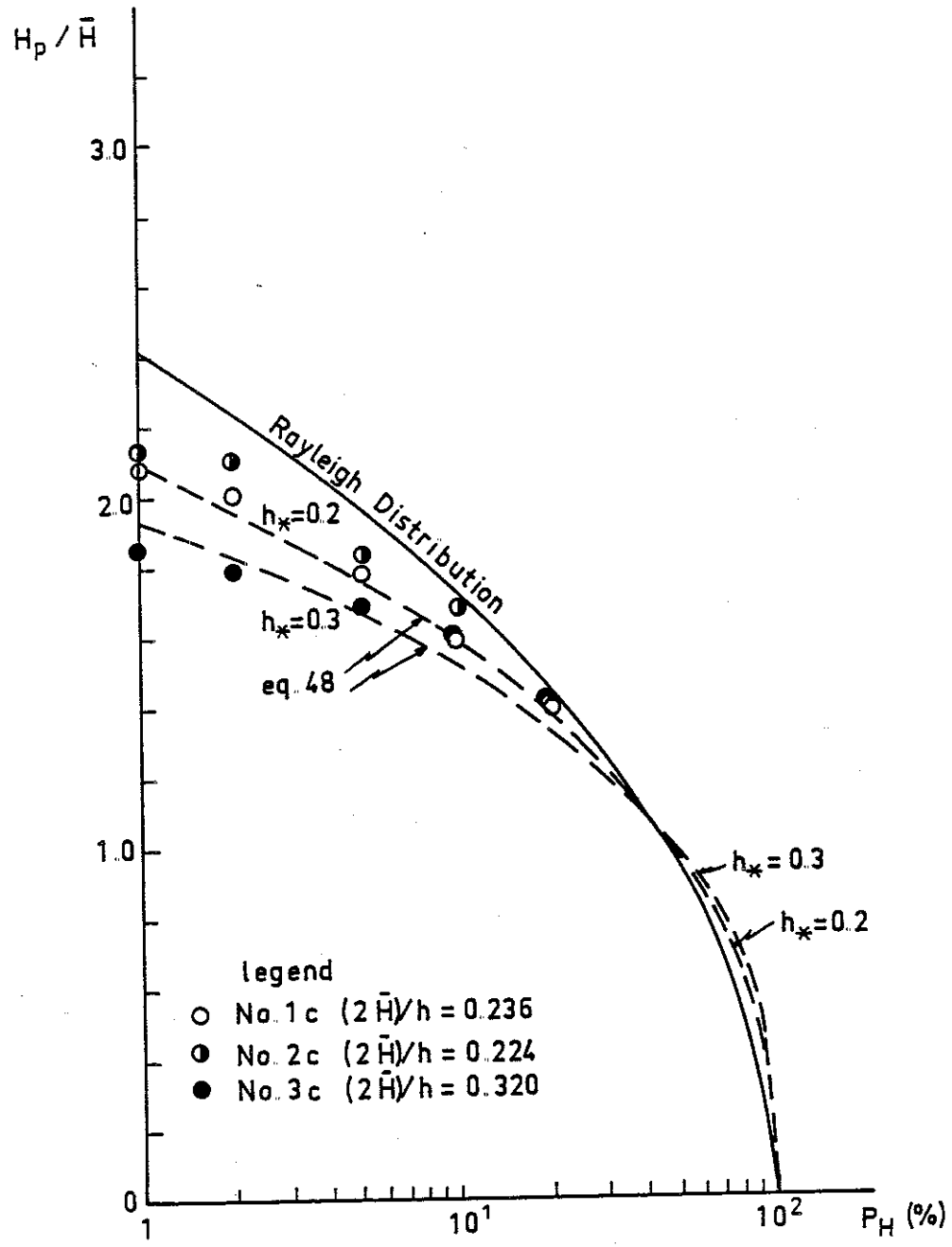

Fig. 50 Comparison of wave height distributions

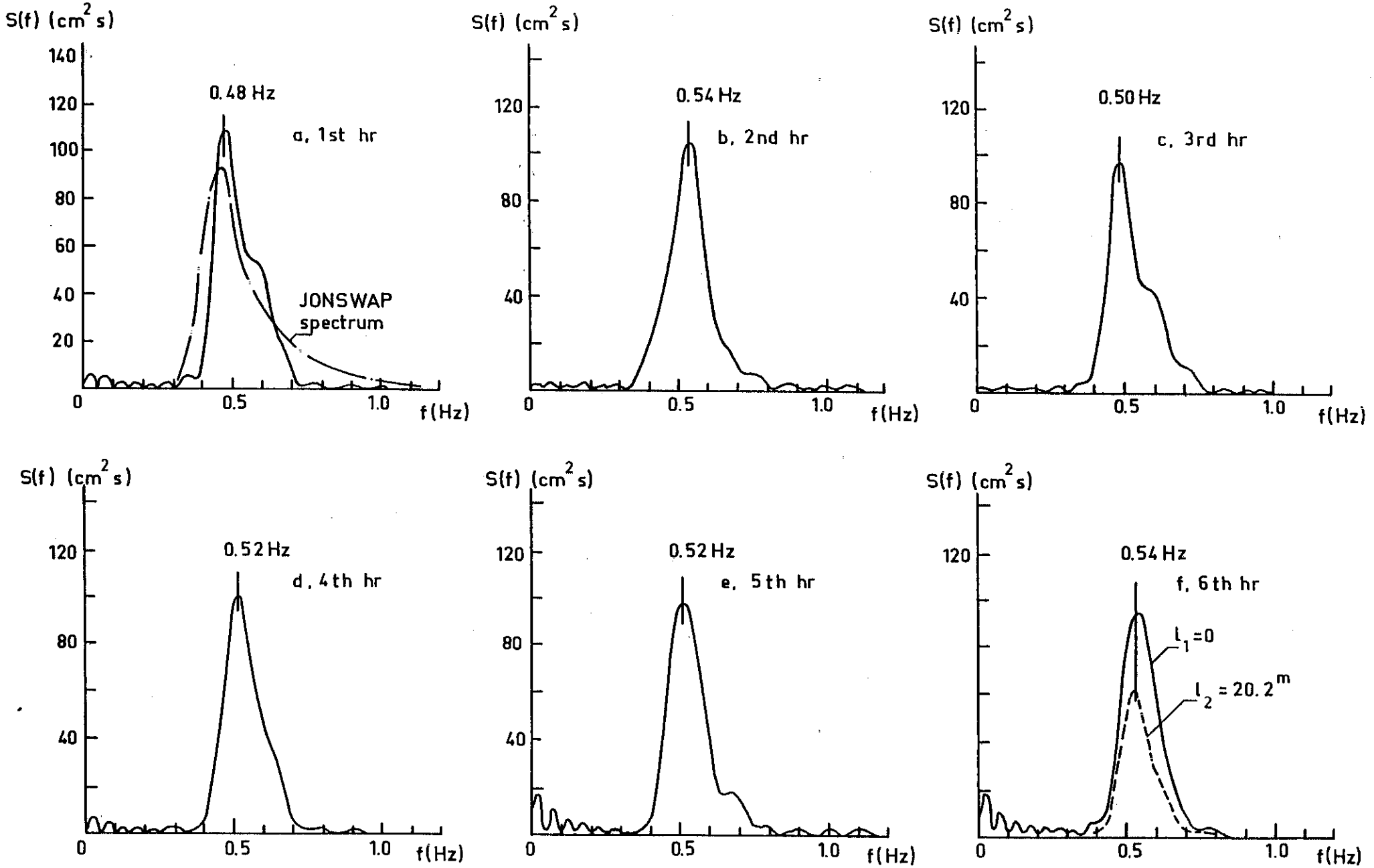

Fig. 5i Wave spectra of test No.ic

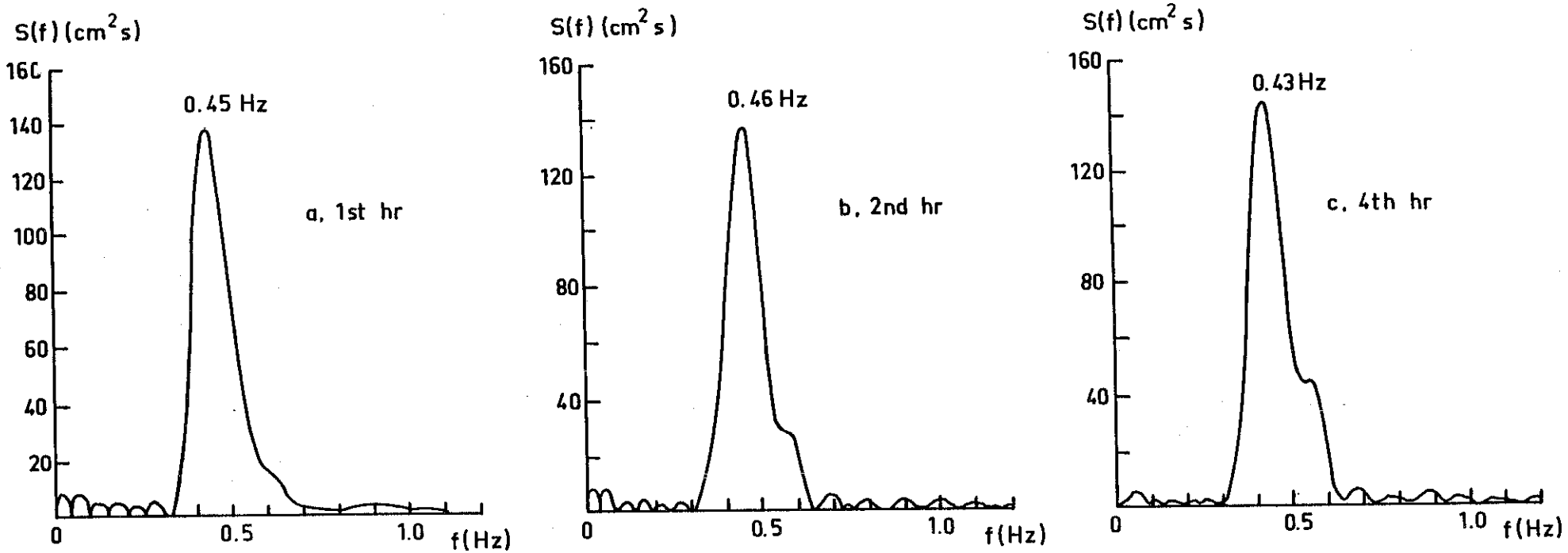

Fig. 52 Wave spectra of test No.2c

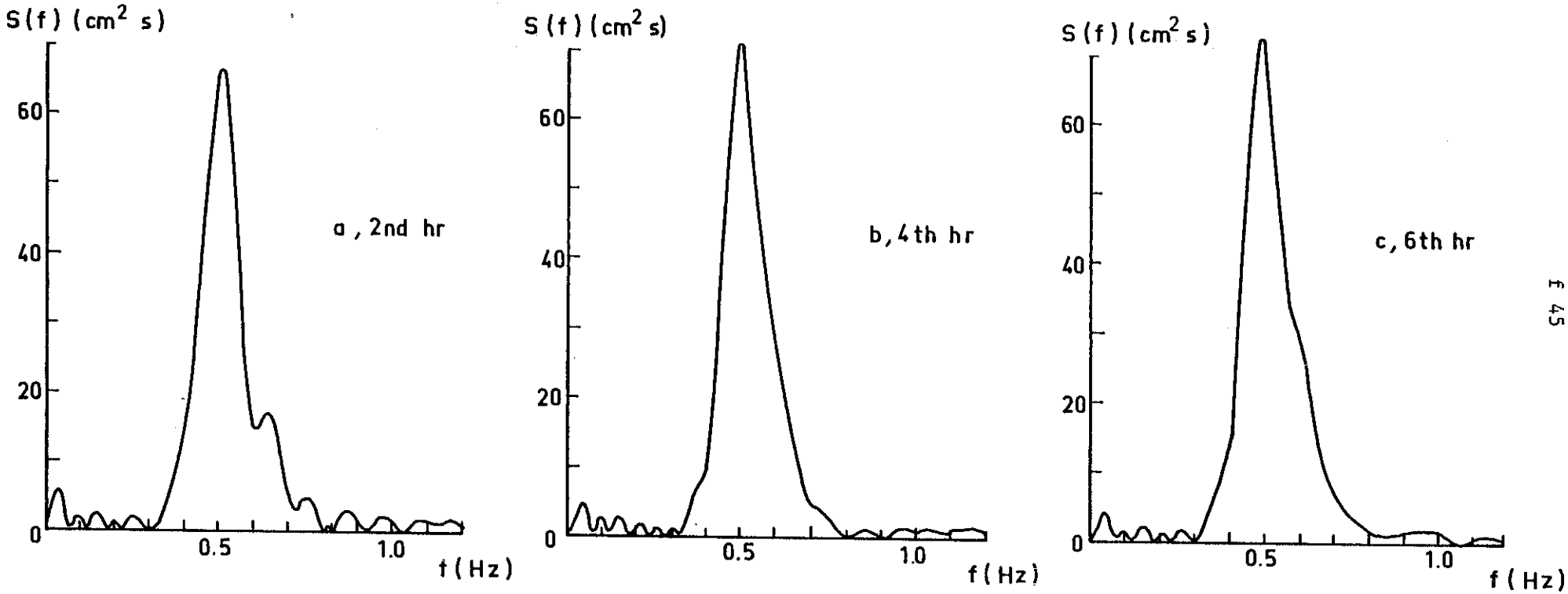

Fig. 53 Wave spectra of test No.3c

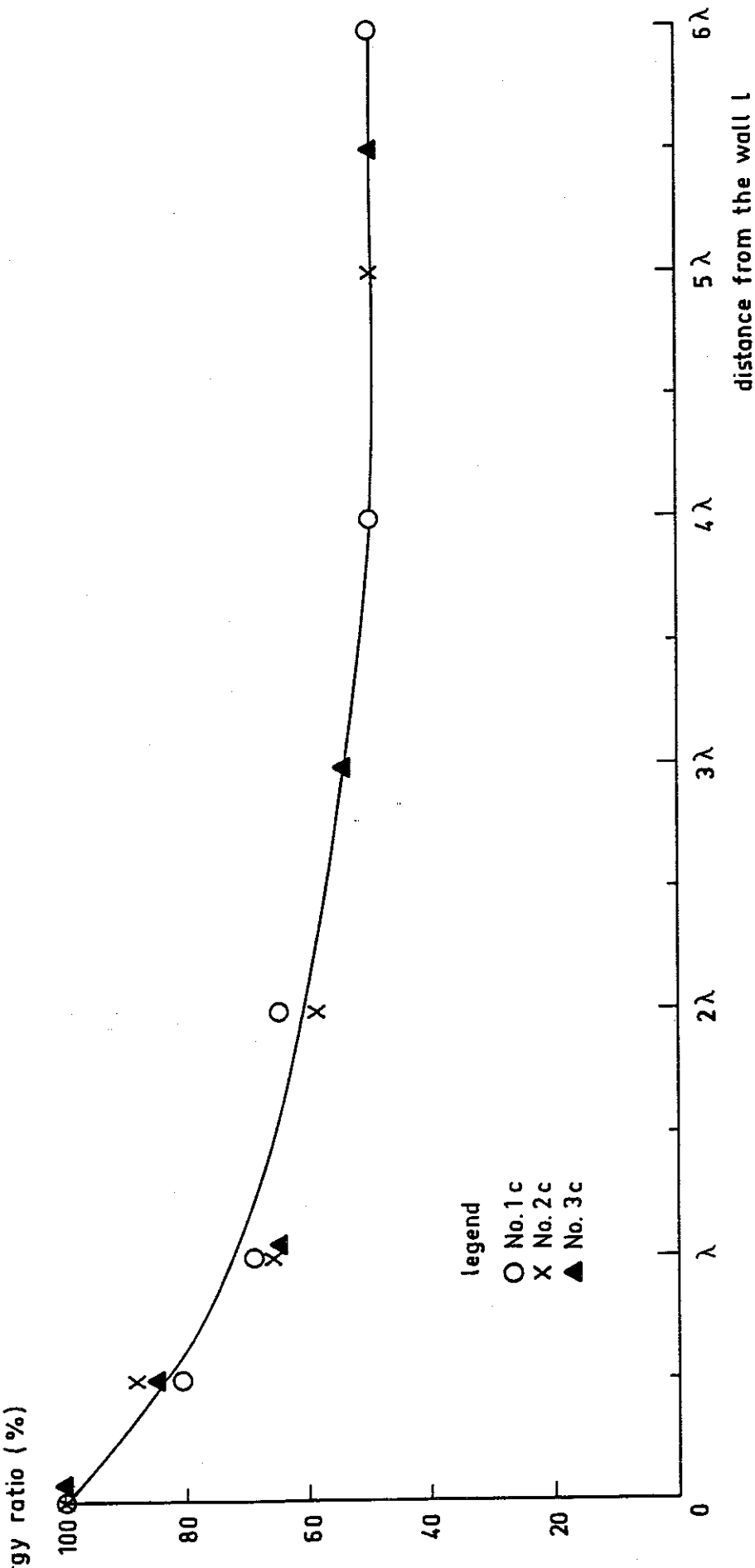

Fig. 54 Wave energy distribution in front of a vertical wall

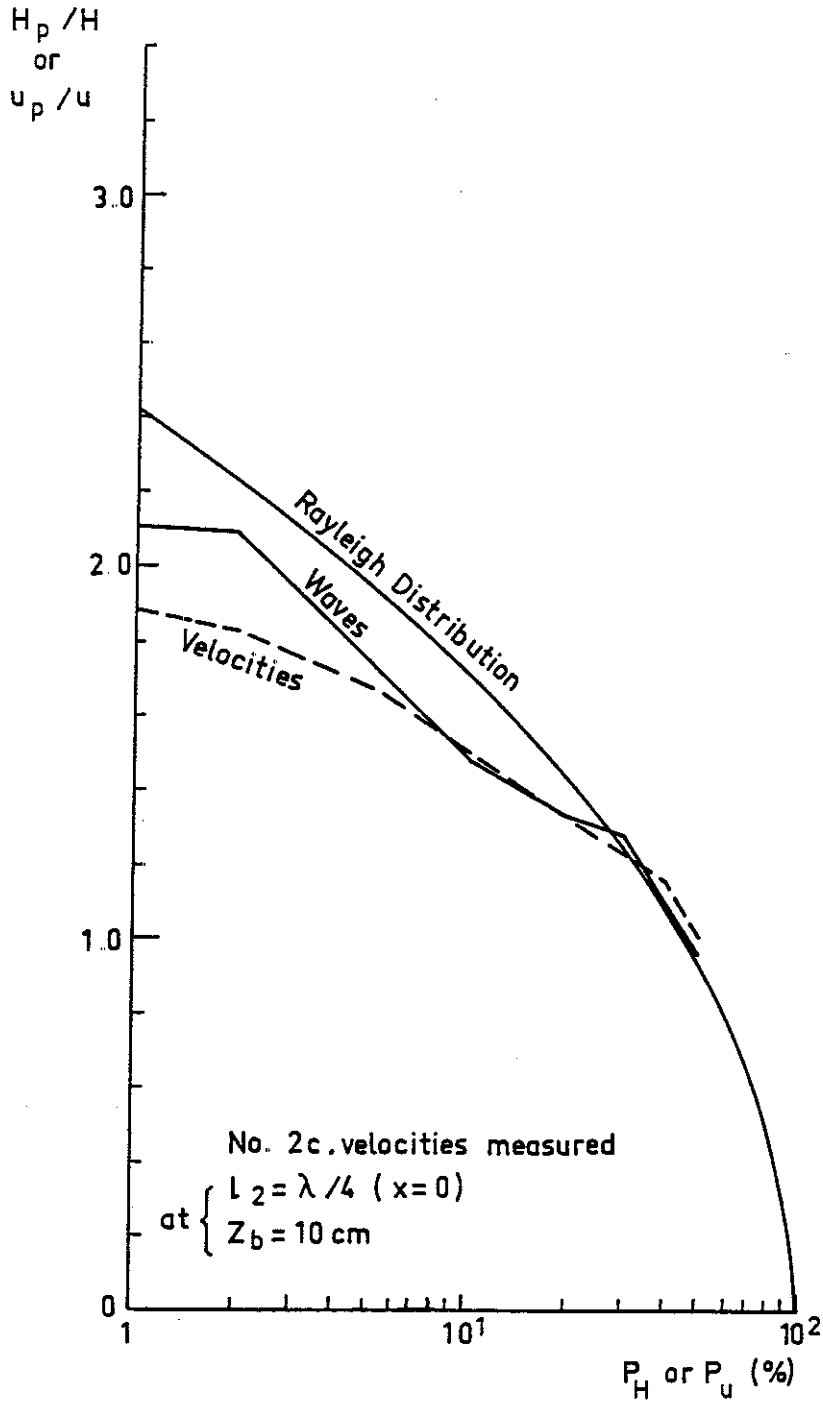

Fig. 55 Statistical property of the orbital velocities of the standing waves

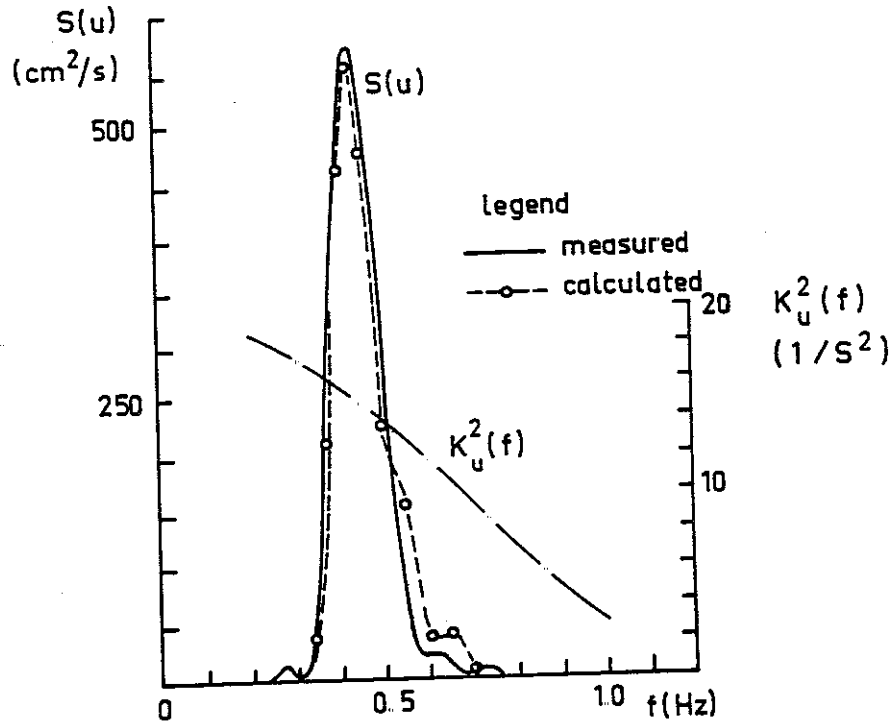

Fig. 56 Velocity spectra of test No.2c

($l = \lambda/4$, $Z_b = 10$ cm)

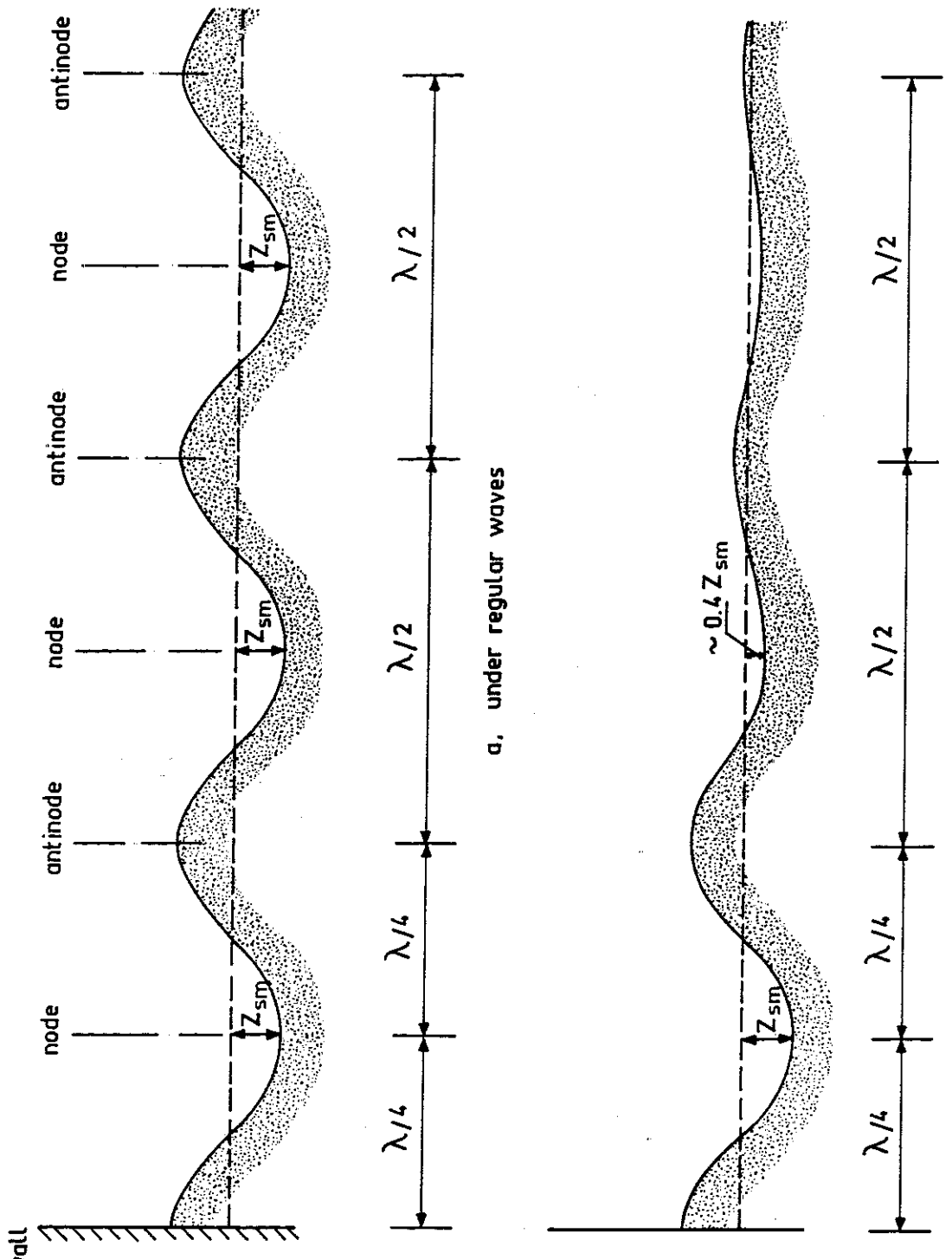

Fig. 57 Scouring profiles for relatively fine material under regular and irregular waves

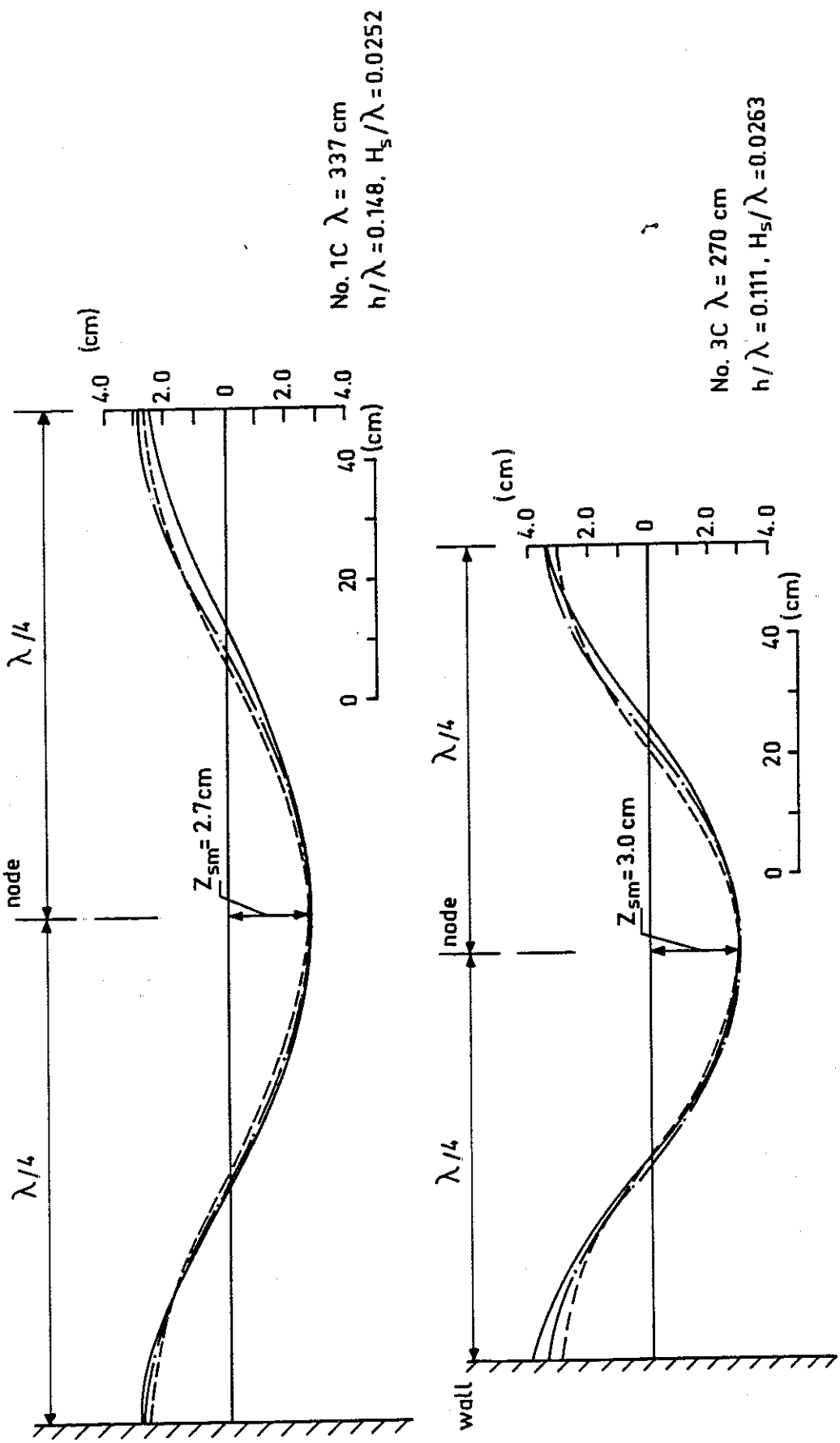

Fig. 58 Comparisons of bottom profiles
(tests No.1c and 3c)

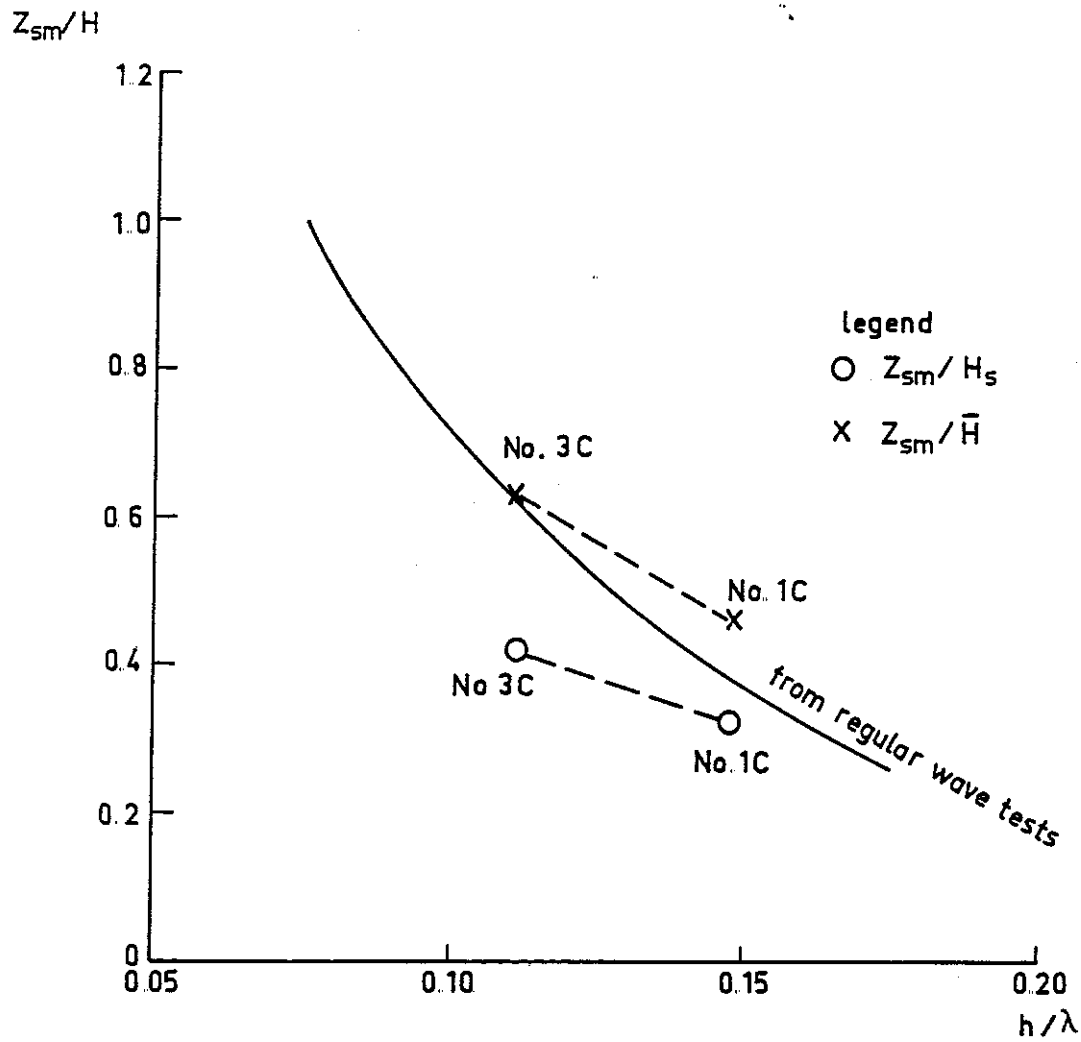

Fig. 59 Z_{sm}/H versus h/λ
for relatively fine material
under irregular waves

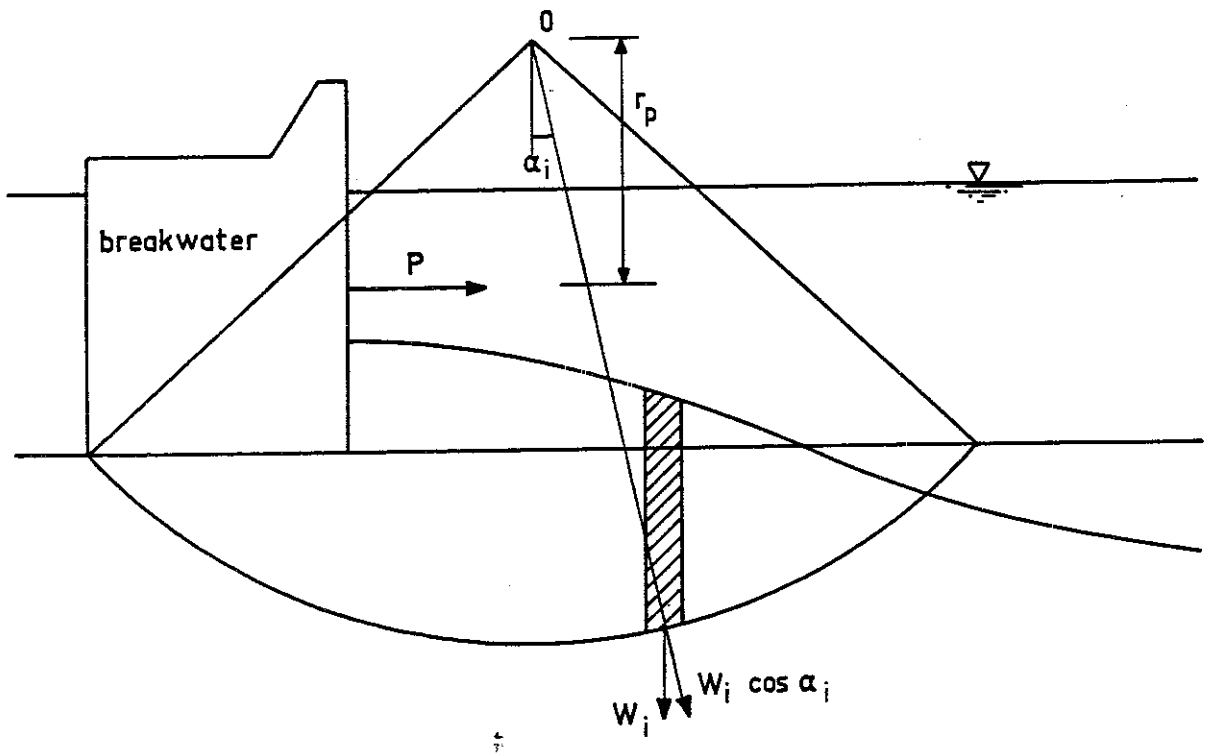

a. for scouring Type "fine"

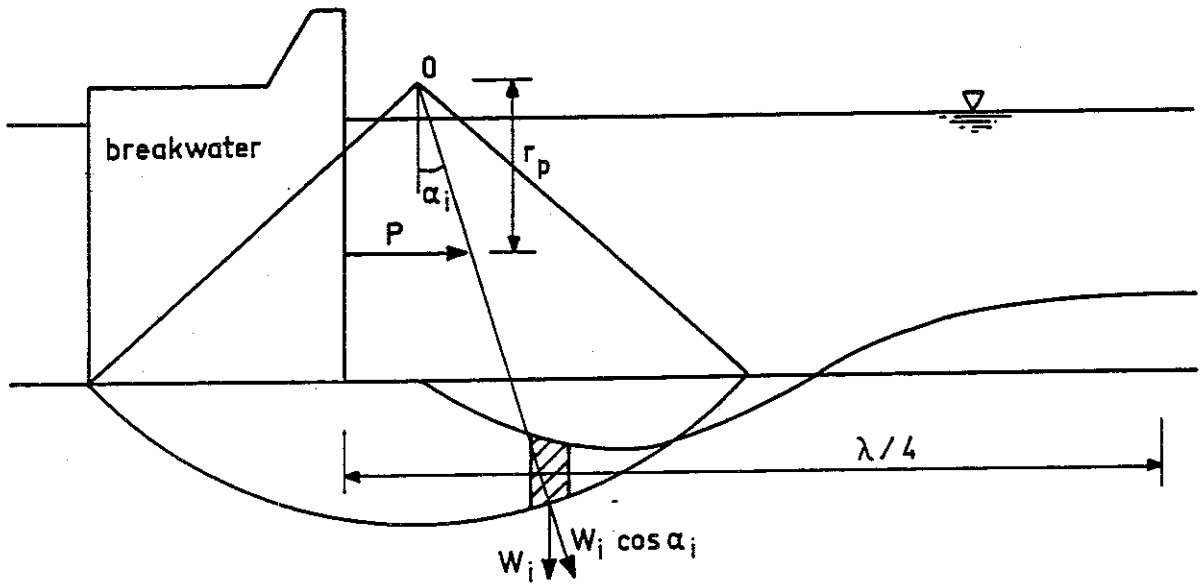

b. for scouring Type "coarse"

Fig. 60 Stability analysis of the foundation of the breakwater influenced by scouring

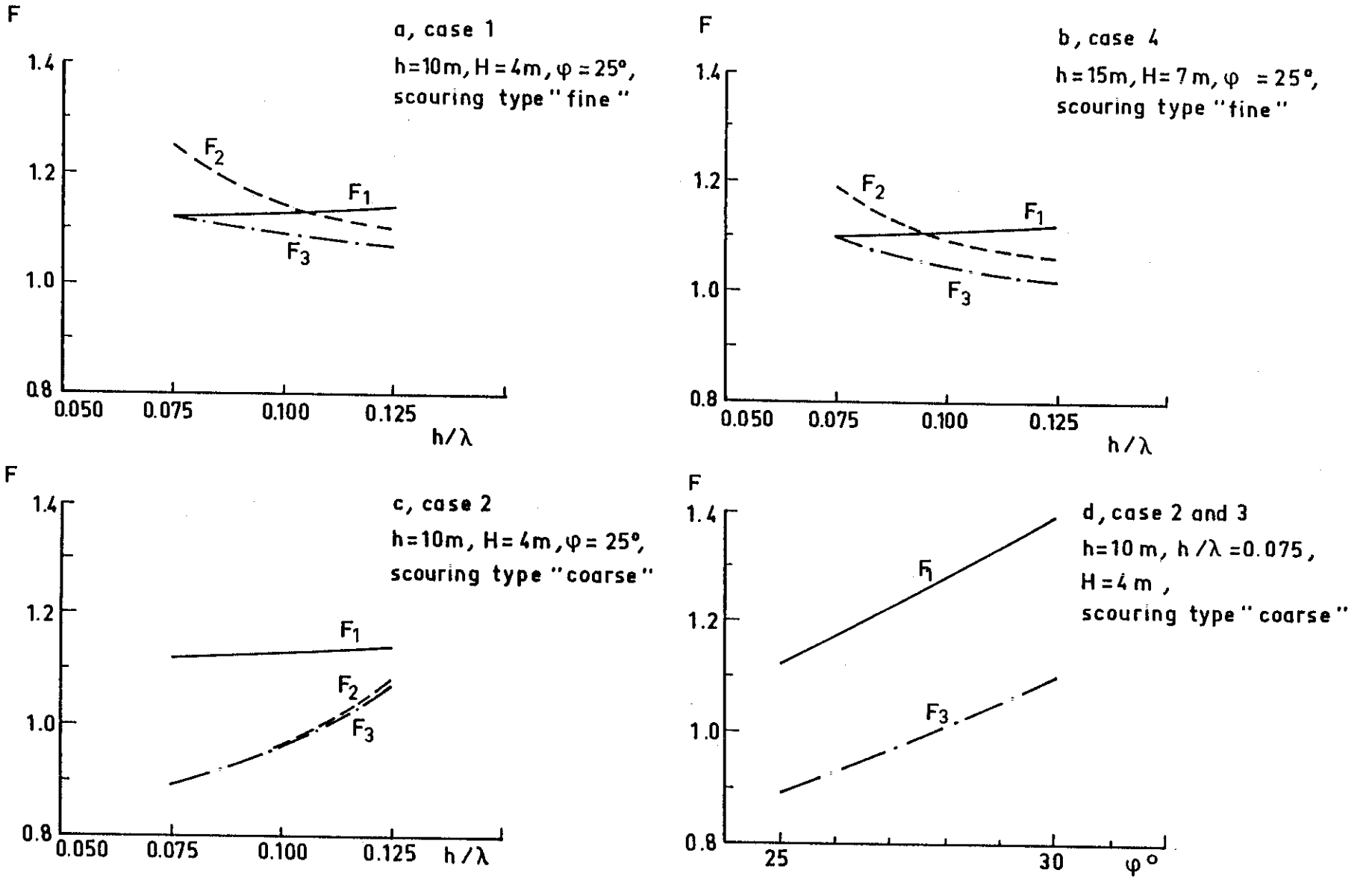

Fig. 61 Influences of scouring on the stability of the breakwater

F_i —— Safety factor when there is no scouring; F_2 —— Safety factor when the influence of scouring pattern is considered;

F_3 —— S.F. when only the influence of scouring trough is considered.

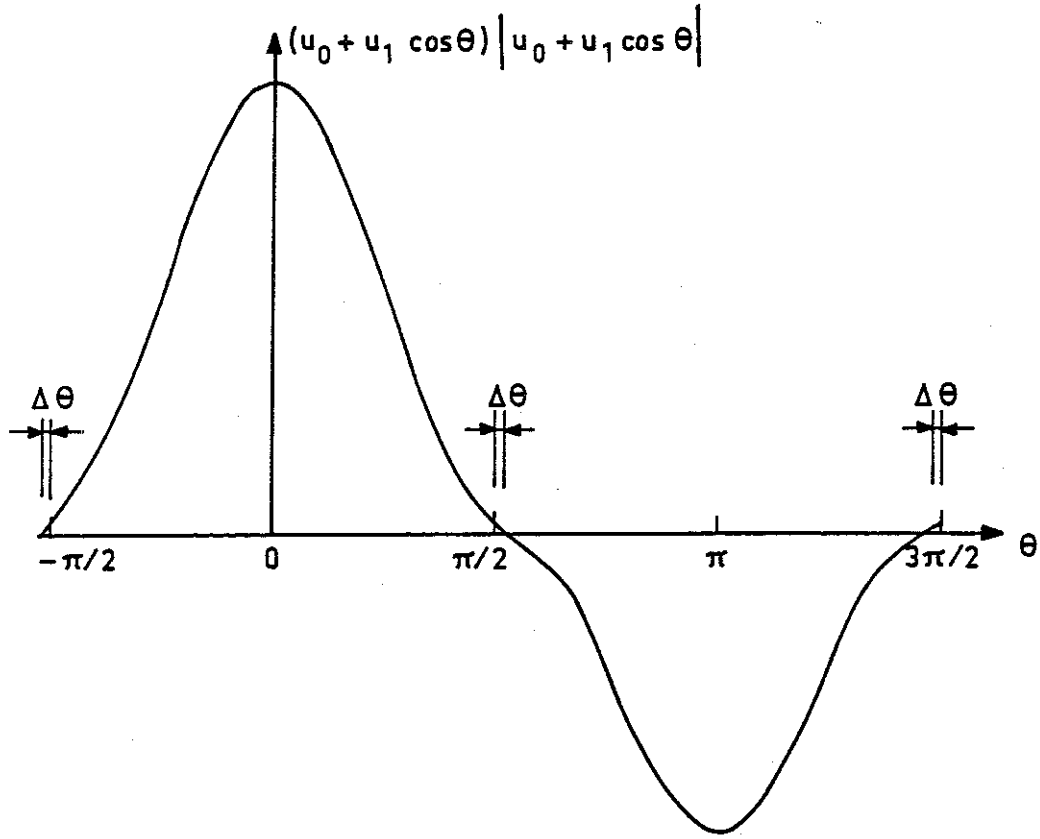

Fig. A1 $(u_o + u_1 \cos\theta) \left/ u_o + u_1 \cos\theta \right/$ versus θ

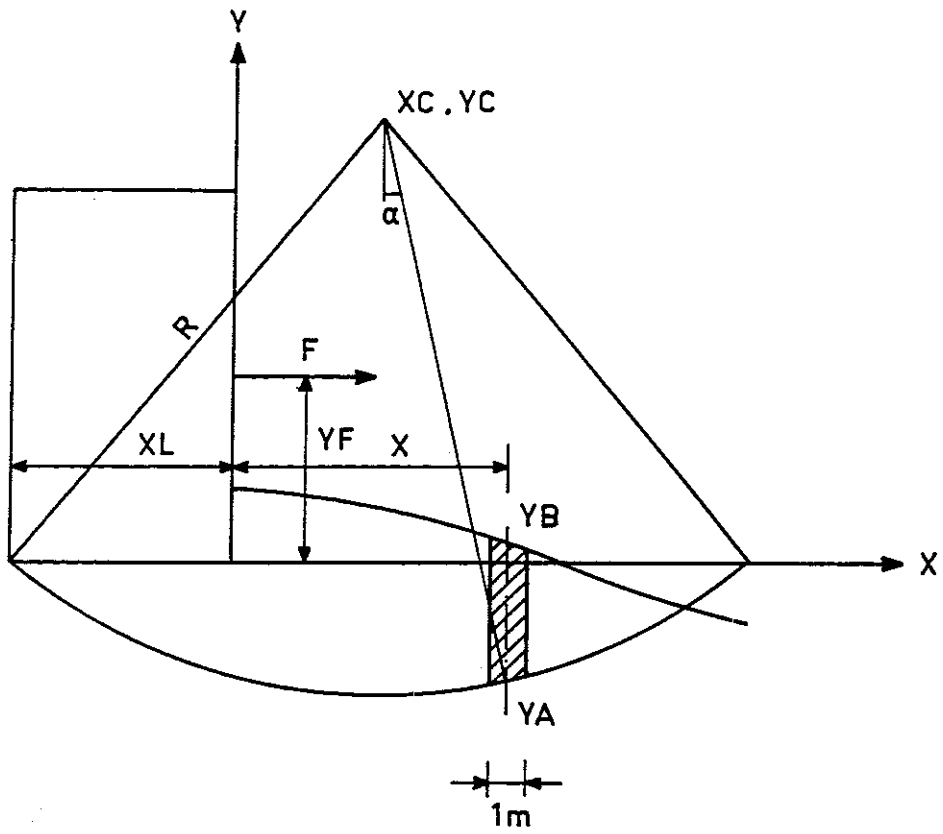

Safety factor $S = \dfrac{\Sigma W \cos\alpha \tan\phi}{\frac{F}{R}(YC-YF)-\Sigma W \sin\alpha}$, ϕ ——— internal friction angle of the soil

Weight of the slice $W = G\ (YB-YA)$, G ——— unit weight of the soil

$YA = YC - \sqrt{R^2-A^2}$, $A = X-XC$

equivalent slice height of the breakwater = $\dfrac{\text{weight of the breakwater}}{G}$

Fig. A2 Main symbols and main equations in the computer program